

INFORMATION TO USERS

The most advanced technology has been used to photograph and reproduce this manuscript from the microfilm master. UMI films the original text directly from the copy submitted. Thus, some dissertation copies are in typewriter face, while others may be from a computer printer.

In the unlikely event that the author did not send UMI a complete manuscript and there are missing pages, these will be noted. Also, if unauthorized copyrighted material had to be removed, a note will indicate the deletion.

Oversize materials (e.g., maps, drawings, charts) are reproduced by sectioning the original, beginning at the upper left-hand corner and continuing from left to right in equal sections with small overlaps. Each oversize page is available as one exposure on a standard 35 mm slide or as a 17" x 23" black and white photographic print for an additional charge.

Photographs included in the original manuscript have been reproduced xerographically in this copy. 35 mm slides or 6" x 9" black and white photographic prints are available for any photographs or illustrations appearing in this copy for an additional charge. Contact UMI directly to order.



300 North Zeeb Road, Ann Arbor, MI 48106-1346 USA

Order Number 8803989

**Low-energy bedload transport by combined wave and current
flow on a southern mid-Atlantic bight shoreface**

Green, Malcolm Omand, Ph.D.

The College of William and Mary, 1987

U·M·I
300 N. Zeeb Rd.
Ann Arbor, MI 48106



PLEASE NOTE:

In all cases this material has been filmed in the best possible way from the available copy. Problems encountered with this document have been identified here with a check mark ✓.

1. Glossy photographs or pages ✓
2. Colored illustrations, paper or print _____
3. Photographs with dark background ✓
4. Illustrations are poor copy _____
5. Pages with black marks, not original copy _____
6. Print shows through as there is text on both sides of page _____
7. Indistinct, broken or small print on several pages _____
8. Print exceeds margin requirements _____
9. Tightly bound copy with print lost in spine _____
10. Computer printout pages with indistinct print _____
11. Page(s) _____ lacking when material received, and not available from school or author.
12. Page(s) _____ seem to be missing in numbering only as text follows.
13. Two pages numbered _____. Text follows.
14. Curling and wrinkled pages _____
15. Dissertation contains pages with print at a slant, filmed as received _____
16. Other _____

U·M·I

LOW-ENERGY BEDLOAD TRANSPORT BY COMBINED WAVE AND CURRENT FLOW
ON A SOUTHERN MID-ATLANTIC BIGHT SHOREFACE

A Dissertation

Presented to

The Faculty of the School of Marine Science
The College of William and Mary in Virginia

In Partial Fulfillment

Of the Requirements for the Degree of
Doctor of Philosophy

by

Malcolm O. Green

1987

APPROVAL SHEET

This dissertation is submitted in partial fulfillment of
the requirements for the degree of

Doctor of Philosophy

Malcolm O. Green
Malcolm O. Green

Approved December, 1987

L. Don Wright

L. Don Wright
Committee Chairman/Advisor

John D. Boon, III

John D. Boon, III

Robert J. Byrne

Robert J. Byrne

Robert J. Diaz

Robert J. Diaz

Egon P. Ruzicki

Egon P. Ruzicki

Richard W. Sternberg

Richard W. Sternberg

School of Oceanography, University of Washington

Dedicated to the memory of John M. Zeigler

TABLE OF CONTENTS

ACKNOWLEDGEMENTS	vi
LIST OF TABLES	vii
LIST OF FIGURES	viii
LIST OF SYMBOLS	x
ABSTRACT	xi
1. INTRODUCTION	2
2. THEORY OF BEDLOAD SEDIMENT TRANSPORT BY COMBINED WAVE AND CURRENT FLOW	9
2.1 Introduction	9
2.2 Bedload Transport by a Pure Wave	11
2.3 Extension of the Pure-Wave Transport Model to Transport by Combined Wave and Current Flow	19
2.3.1 Introduction	19
2.3.2 Theory of combined-flow boundary-layer dynamics	19
2.3.3 Bedload transport by combined wave and current flow	28
2.4 Effect of Wave Asymmetry	33
2.5 Estimation of z_0	34
3. METHODOLOGY AND DATA ANALYSIS	39
3.1 Introduction	39
3.2 Physical Setting of the Duck Shoreface	40
3.2.1 Surficial geology	40
3.2.2 Physical oceanography	51
3.3 Experiment Description and Data Analysis	53
3.3.1 Mid-shoreface experiment	55
3.3.2 Lower-shoreface experiment	64
3.4 Evaluation of Dynamic and Flux Estimates	70
3.4.1 Dynamic calculations	70

3.4.2 Flux calculations	75
3.4.3 Sensitivity analysis	76
4. A MODEL FOR LOW-ENERGY BEDLOAD TRANSPORT ON THE SHOREFACE	86
4.1 Introduction	86
4.2 Onshore Transport	87
4.2.1 Local transport	87
4.2.2 Cross-shore gradient in transport	91
4.2.3 Effect of wave asymmetry	97
4.3 Offshore Transport	99
4.3.1 Local transport	99
4.3.2 Cross-shore gradient in transport	100
4.3.3 Effect of wave asymmetry	104
4.4 Variable Wave Direction	108
4.5 Discussion	110
5. OBSERVED SHOREFACE RESPONSE TO LOW-ENERGY COMPETENT FLOW	115
5.1 Methodology and Data Analysis	115
5.2 Discussion	125
6. CONCLUSIONS	128
APPENDIX	134
LITERATURE CITED	151
VITA	162

ACKNOWLEDGEMENTS

This work was supported from its inception by the Virginia Institute of Marine Science (VIMS). Support at various times was provided by the Southeastern Undersea Research Facility (SURF) at the University of North Carolina at Wilmington; the Geological Society of America, Grant No. 3436-85; the Minor Research Grants Committee, College of William and Mary; the U.S. Army Corps of Engineers Waterways Experiment Station, Grant No. DACW3986 M3677; and the National Science Foundation, Grant No. OCE-8610635.

I am grateful to each of my committee members for wise counsel and encouragement. In particular, I am indebted to Don Wright for providing inspiration since those first classes in the Institute Building, and for giving me my first and many subsequent opportunities. I sincerely thank you for your guidance and unfaltering support.

Working offshore with equipment that is both heavy and delicate at the same time is difficult to say the least. I am indebted to many persons for expertise and assistance. Thanks are due to the Captain and crew of the R/V Seahawk (SURF); the personnel of Vessel Operations at VIMS, including Charles Machen (R/V Langley), Durand Ward and Steve George (R/V Bay Eagle), George Pongonis and Ken Worrell; and Buddy Matthews, Suzanne Alexander and John Posenau of Physical Oceanography. Special thanks are due to the geology field crew for creative solutions and sometimes dangerous work: Don Wright, Bob Gammisch, John Boon, Linda Schaffner, Danny Gouge, Bob Diaz, Bob Byrne and Jeff List. The personnel at the U.S. Army Corps of Engineers Field Research Facility provided valuable shore-based support - I thank Curt Mason especially. Thanks to Jeff Williams, U.S.G.S., for the loan of data in the early phases of the work. Mr. Lewis Glucksman, New York, generously donated the side-scan sonar to VIMS. A special note of thanks is due to John Boon for taking the lead in the instrument development and calibration program, which of course made the whole field exercise possible.

These acknowledgements would not be complete without recognizing the staff of the VIMS Computer Center and Library, and also Cynthia Gaskins for cheerfully handling much paperwork. And for making the long hours bearable, I thank the inhabitants, past and present, of Reed Hall and the Embassy.

Finally, I thank my parents (all four of you), who have borne the strain of our wide separation, and Janice, for support given with grace and good humour.

LIST OF TABLES

3.1	Shoreface sediment parameters	48
3.2	Sensitivity of stress and transport to k_G	84

LIST OF FIGURES

1.1	A. Location map. B. Shoreface definition sketch	4
2.1	Vertical profile of mean component of combined flow	23
2.2	Wave friction factor versus relative roughness	26
2.3	Variation of $f_{w,wc}$ with U_c and θ	27
2.4	$\bar{\phi}_{wc}$ calculated from equations 2.37 and 2.39	30
2.5	Effect of threshold condition on net transport direction ...	32
3.1	Survey lines	43
3.2	A. Shore-normal bathymetry. B. Inner-shelf ridge field	44
3.3	Acoustic imagery of shoreface	46
3.4	Mean grain-size as a function of depth	49
3.5	Locations of current-meter deployments	54
3.6	Mean flow, high and low tides; 17.5-m depth deployment	59
3.7	$U_{1/10}$, U_{100} , T_p , wave and current direction; 17.5-m depth ..	60
3.8	Velocity power spectrum; 17.5-m depth	62
3.9	Burst-averaged dynamic and transport parameters; 17.5-m	63
3.10	Primary physical roughness; 22-m depth	65
3.11	Mean flow, high and low tides; 22-m depth deployment	67
3.12	$U_{1/10}$, U_{100} , T_p , wave and current direction; 22-m depth ...	68
3.13	Burst-averaged dynamic and transport parameters; 22-m	69
3.14	Verification of $U_{*c,wc}$ with CODE data	73
3.15	Verification of z_1 with CODE data	74
3.16	Steady-flow calibration of electromagnetic current meter ..	78

3.17	Sensitivity of stress and transport to U_c	79
3.18	Sensitivity of stress and transport to $U_{w,m}$	81
3.19	Classification of observed flow regimes; 17.5-m depth	83
4.1	Onshore transport: rotation of net transport vector	90
4.2	Onshore transport, symmetrical wave: gradients	96
4.3	Onshore transport: cross-shore variation in total load	98
4.4	Offshore transport: rotation of net transport vector	101
4.5	Offshore transport, symmetrical wave: gradients	103
4.6	Offshore transport: cross-shore variation in total load	105
4.7	Offshore transport, asymmetrical wave: gradients	106
4.8	Effect of variable wave direction	109
5.1	Mean flow, high and low tides; 8-m depth deployment	117
5.2	Wave and current components of total skin friction	119
5.3	S_k , \bar{u}^3 and \bar{u} ; 8-m depth	121
5.4	Samples of record of relative bed elevation; 8-m depth	123
5.5	Burst-averaged relative bed elevation; 8-m depth	124
5.6	Relative bed elevation and \bar{u}^3 ; 8-m depth	126
A.1	Predicted cross-shore variation of $f_{e,wc}$	144
A.2	Predicted cross-shore variation of \bar{E}_{wc}/\bar{E}_w	147
A.3	Predicted cross-shore variation of roughness	148
A.4	Predicted versus observed inshore wave heights	150

LIST OF SYMBOLS

A	near-bed wave-orbital semi-excursion
b	width
C_1	constant in expression for time-averaged dimensionless transport
C_2	empirical constant in grain roughness expression (2.43)
C_3	empirical constant in ripple roughness expression (2.44)
C_g	wave group velocity
C_p	wave phase speed
D	sediment grain-size
E	wave energy dissipation rate
f_w	wave friction factor
f_e	wave dissipation factor
g	acceleration due to gravity
h	water depth
H	wave height
k	boundary roughness
k_G	grain roughness
k_M	movable-bed roughness
k_R	ripple roughness
K	eddy viscosity
K_f	frictional-dissipation coefficient
K_r	refraction coefficient
K_s	shoaling coefficient
L	wavelength
m	empirical coefficient in Dean's profile model
n	number of observations
p	empirical coefficient in Dean's profile model

P	wave energy flux
q	weight rate of bedload transport per width
Q	volume rate of bedload transport per width
RE	wave Reynolds number
S_k	non-dimensional skewness
t	time
T	wave period
T_p	peak spectral period
u	shore-normal velocity component
\bar{u}^3	mean cube shore-normal velocity
U	velocity
U_{100}	mean-flow speed at $z = 100$ cm
$U_{1/10}$	average of highest 10% of wave-orbital velocities
U_*	friction velocity
w	sediment settling velocity
W	weight of sediment
x	horizontal co-ordinate
y	horizontal co-ordinate
z	elevation above the bed
z_0	elevation above bed where mean flow vanishes
z_1	elevation above bed where mean flow appears to vanish from $z > \delta_w$
α	wave angle of incidence
δ	boundary-layer thickness
δz	net change in bed elevation
ζ	rotation angle
n	wave-ripple height
θ	acute angle between wave and current

κ	von Karman's constant
λ	wave-ripple length
μ_N	Nth moment of combined-flow velocity distribution
ν	kinematic fluid viscosity
ρ	density
σ	phase lag
τ	shear stress
T	half-series length
ϕ	dimensionless bedload-transport rate
ψ	Shields parameter
ω	wave radian frequency

SUBSCRIPTS

c	current
cr	critical
f	fluid
m	maximum value in wave period
s	sediment
t	total
w	wave
wc	wave-current

SUPERSCRIPTS

'	skin friction
-	time-averaged
^	vector quantity

MISCELLANEOUS

,	commas separate multiple subscripts
---	-------------------------------------

ABSTRACT

The control of the first three moments of the combined-flow velocity distribution (mean flow, wind-wave energy and wind-wave asymmetry) on low-energy bedload transport magnitude, direction and divergence on a wave-dominated shoreface was investigated using deterministic dynamics and transport models. The objective was to develop a mechanistic basis for postulated fairweather replenishment of the beach sediment prism by sediments derived from offshore.

Fairweather currents were measured at 17.5-m and 22-m depth on two separate occasions. Using a combined-flow boundary-layer model, periods of competent flow were identified. Madsen and Grant's (1976) combined-flow bedload-transport model was used to calculate sediment fluxes after modification of the expression for instantaneous transport rate to include a threshold criterion; this was necessary since sediment may not be in motion over the whole wave period in low-energy conditions. The asymmetry thus introduced into the instantaneous transport rate resulted in partial control over transport direction by the oscillatory motion.

Three events, each >9 hours duration and characterized by steady and unidirectional mean flow that suppressed the semi-diurnal tidal-current rotation, were among those identified. This seems indicative of a coherent mean-current field of broad spatial extent, of the type that is usually high-energy and wind-driven. However, the observed flow was neither high-energy nor correlated with strong local winds.

The oscillatory motion contributed >80% of the total skin friction. Direction of net transport was controlled by: relative orientation of the oscillatory and mean components of the combined flow, wave-orbital velocity asymmetry, and the threshold criterion. The threshold-induced rotation of the net transport vector was significant on the lower shoreface where the flow was not intense and the wave-orbital velocity was not greatly skewed. Enhancement of both offshore and onshore transport in this way was inferred from analysis of the velocity data.

Bedload-flux divergence associated with each of the observed events was simulated using a one-dimensional numerical model. Predicted divergence was explained in terms of: cross-shore variation in transport magnitude, which was driven primarily by a shoreward increase in the wave component of the total skin friction; cross-shore variation in transport direction, which was controlled by the mean current, degree of wave asymmetry, and the flow intensity; and proportion of the total load moving in suspension.

Two scenarios were identified. The first was characterized by offshore transport seaward of ~10-m depth under the dominant influence of the mean flow, and onshore transport at the top of the shoreface under the dominant influence of shoreward-skewed wave-orbital velocities. The second was characterized by onshore transport at every point on the profile. The key prediction, common to both scenarios, was upper-shoreface accretion under the dominant control of shoreward-skewed wave-orbital velocities. Direct observations of upper-shoreface accretion in 8-m depth (a total of ~6 cm in 4.5 days) were consistent with the model simulations, however, the mean flow at 8-m depth controlled the transport direction. Observations and model calculations supported the concept of fairweather nourishment of the beach sediment prism by sediment transported from offshore, however the mean flow may play a more important role than previously recognized.

LOW-ENERGY BEDLOAD TRANSPORT BY COMBINED WAVE AND CURRENT FLOW
ON A SOUTHERN MID-ATLANTIC BIGHT SHOREFACE

1. INTRODUCTION

Surfzone dynamics and morphology have been explained in terms of parameters such as breaker wave height and angle of incidence, gradients in wave height and radiation stress, standing-wave motions, wave asymmetry and bed sediment. Whereas the effect of the inner shelf and shoreface seaward of the breakpoint on some of these terms has long been appreciated (e.g. breaker height, long waves), only recently has the importance of bi-directional sediment exchange between the surfzone and deeper waters offshore been recognized. Niedoroda and Swift (1981) and Swift et al. (1985) postulated that sediment eroded from the beach and upper shoreface and deposited on the inner shelf during storms is returned to the beach via the shoreface during fairweather. Swift et al. (1985) reasoned that since fairweather shoreface currents may be competent (i.e. capable of entraining sediment) only in shallow depths, sediment transported far offshore by storms may be permanently removed from the return limb of the cycle; the result, given no external sediment supply, is a landward migration of the shoreface profile. Wright et al. (1984) postulated that major shifts in beach state and attendant morphology, dynamics and erosion potential are linked to changes in the total inshore sand storage, where those changes are caused by sediment cycling between the inner shelf and surfzone.

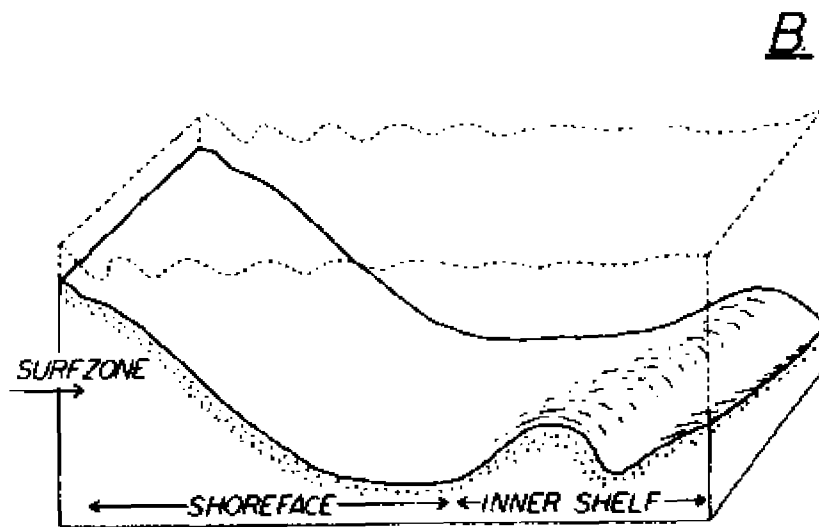
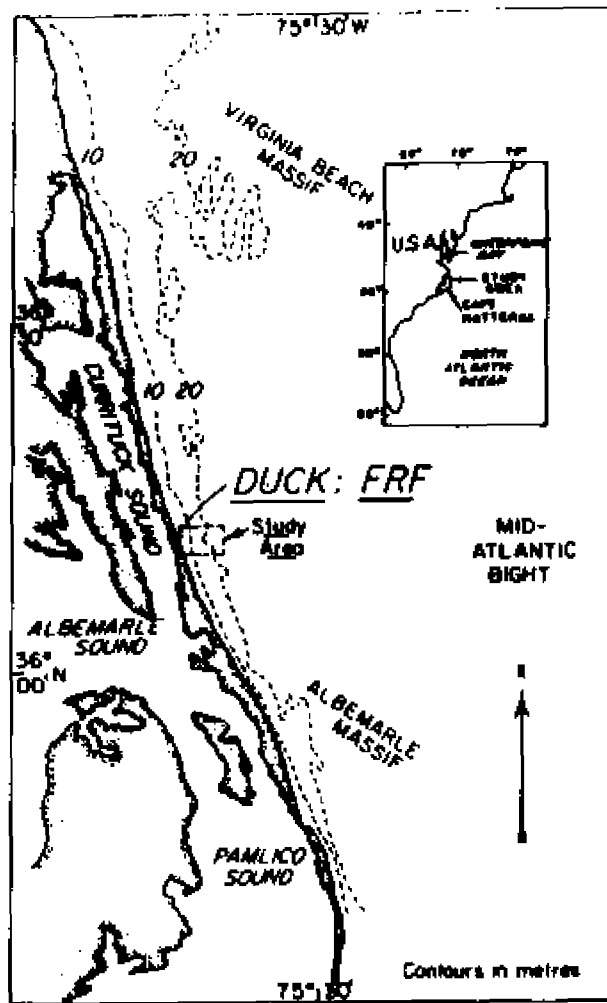
High-energy shoreface sediment transport has been attributed to: wind-driven downwelling (Wright et al., 1986) and coastal jets (Ludwick,

1978); rip currents (Reimnitz, et al, 1976; Cowell, 1986); turbidity currents (Seymour, 1986); and amplitude-modulated surface gravity-waves (Shi and Larsen, 1984). Fairweather sediment transport has been the focus of far less attention. With the notable exception of Niedoroda (1980) and Niedoroda and Swift (1981), who showed that an abrupt increase in onshore-directed bedload flux under fairweather asymmetric waves occurred between depths of 5 and 15 m on a wave-dominated shoreface, detailed treatment of fairweather shoreface sediment transport has previously been lacking.

The objective of this work is to add to the understanding of the processes that drive the fairweather transit of sediments across an unconsolidated wave-dominated shoreface, the rationale being to fill the gap in knowledge created by past bias towards storm processes. The subject of the study is the shoreface (Figure 1.1) fronting a sand barrier island in the southern Mid-Atlantic Bight of North America, where the shoreface is that zone of steeply sloping seafloor between the surfzone (perched near the shoreline) and the inner margin of the continental shelf (relatively deep and flat). Until recently, much of what was known about shoreface sediment transport had only been inferred from the surficial and sub-bottom shoreface geology, with scant attention being paid to actual processes. Early geological investigations demonstrated that most modern barrier-island coasts on this seaboard were initiated by the late-Holocene reduction in the rate of sea-level rise which began about 4,000 to 7,000 years before present (Curry, 1969). Coherent descriptions of the inner-shelf and shoreface sub-bottom structure provided the observational evidence from which shoreward migration of the barrier-island complex in the face of rising

Figure 1.1 A. Location map. The study area is the shoreface fronting the Field Research Facility (FRF) at Duck on the Outer Banks of North Carolina in the southern Mid-Atlantic Bight.

B. Definition sketch: idealized unconsolidated sand shoreface of the southern Mid-Atlantic Bight.



sea-level was deduced (Fischer, 1961). Typically, the uniform fine to medium sands of the barrier islands form a wedge-shaped cross-section, thinning from 15 m at the shoreline to ~1 m at depths of 10 to 15 m (Field et al., 1979). Underlying the barrier sands, and cropping out at the base of the sand-wedge, are deposits of backbarrier origin: mixtures of peats and muds derived from lagoons and tidal marshes, and sands and muds derived from flood-tide deltas (Field et al., 1979). The inner shelf is mantled by a blanket of clean, well-sorted sand, 0 to 10-m thick, which in places bears large-scale (up to 10-m relief) ridge-and-swale topography (Green, 1986). The basement material is of Pleistocene age (or older) and is of varied composition. The basement structure reflects deposition in various environments and various degrees of post-depositional alteration (Pierce and Colquhoun, 1970).

Bruun (1962) proposed a model of the erosional shoreface retreat that occurs in the face of rising sea-level. The model described the kinematics of the barrier-island migration and adequately accounted for the classical transgressive stratigraphy. Bruun postulated that a rise in sea-level resulted in a landward and upward translation of the shoreface/inner-shelf profile with an equal volume of sediment transferred from the eroding shoreface to the adjacent shelf floor. According to the model, the inner shelf acts as a sink to the sediments removed from the eroding shoreface; the migrating barrier also lays a pavement of flood-tide delta deposits and washover fans before it (Leatherman, 1979).

The Bruun model is consistent with observed stratigraphy and in one case the model predictions were confirmed by direct measurements of shoreface deflation and adjacent equal-volume inner-shelf aggradation

(Moody, 1964). Still, Bruun's model is only a description of geometry; the model has nothing to say about the actual mechanisms of sediment dispersal on the shoreface. The challenge of the mechanistic or process approach, undertaken herein, is to reconcile the detailed theories of sediment transport with observations of morphology.

Surfzone currents are driven primarily by high-frequency wind waves and the nonlinear interactions that occur between them; the resulting water motions are strongly controlled and focussed by the surfzone morphology, including the subaerial beachface. Inner-shelf currents, in contrast, are energetic at lower frequencies (semi-diurnal and lower) and are driven by one or more of a variety of forces, including wind stresses, astronomical forces, Coriolis force and baroclinic pressure gradients. It may be assumed a priori (and left to subsequent demonstration) that shoreface fluid motions comprise both high-frequency oscillatory and steady (relative to the oscillatory flow) components. The important properties of the combined flow relevant to sediment transport are the first three moments of the velocity distribution (Bowen and Doering, 1984), which are the the mean, the variance and the skewness respectively. The Nth moment, μ_N , is defined as:

$$\mu_N = \lim_{T \rightarrow \infty} 1/(2T) \int_{-T}^T (U - \bar{U})^N dt \quad (1.1)$$

where U is velocity, 2T is the length of the time series of U, \bar{U} is the arithmetic mean of U, t is time, and N is an integer.

The variance of the velocity represents the wave energy, which controls the rate of sediment resuspension (Lesht et al., 1980; Vincent

et al., 1982). To the first order, suspended sediment is advected by the mean flow (Huntley and Bowen, 1975), where the mean flow may be, for instance, a drift velocity (Kim and Wright, 1987), a tidal current (Wright, 1981) or a wind-driven current (Karl et al., 1981). The direction of bedload flux may depend more on the velocity skewness than on the mean flow. For example, Wells (1967) showed that the direction of bedload transport is given by the sign of the skewness, where the skewness represents the asymmetry of the wave-induced velocities. Huntley and Bowen (1975) noted that if the mean current is strong enough, the sign of the bedload flux can be opposite that of the wave skewness. Bowen's (1980) and Bailard's (1981) models of the equilibrium beach-profile highlighted the critical dependence of beach slope and cross-shore transport on both odd and even moments of the velocity distribution. Their work has subsequently stimulated interest in how these statistical quantities vary with depth across the surfzone and with deepwater and local wave parameters (e.g. Bowen and Doering, 1984; Guza and Thornton, 1985).

Low-energy transport of sediment as bedload on the shoreface will be addressed herein in terms of the competing controls exerted by the first three moments of the combined flow (i.e. the mean current, the wind-wave energy, and the wind-wave asymmetry). The approach taken though is not a statistical one; rather, a deterministic model of boundary shear stress and bedload sediment transport is used to investigate the role of each relevant moment in controlling the rate of sediment entrainment from the bed and the direction of net sediment transport. Sediment sinks and sources, and sediment pathways connecting

the inner shelf, shoreface and surfzone, are governed by the sediment-flux divergence, rather than simply local sediment flux. The same deterministic models of sediment transport are used to elucidate these pathways and provide a mechanistic basis to the concept of shoreface-surfzone sediment cycling.

2. THEORY OF BEDLOAD SEDIMENT TRANSPORT BY COMBINED WAVE AND CURRENT FLOW

2.1 Introduction

Chapter 2 is devoted to developing the deterministic models of boundary-layer dynamics and bedload transport that will be used to address the shoreface sediment dynamics. It is assumed a priori that fairweather currents on the shoreface comprise an oscillatory and a mean component, thus the focus in this chapter is on models of combined-flow dynamics and transport.

The theory of bedload sediment transport by combined wave and current flow has borrowed heavily from the theory of steady, unidirectional, open-channel transport. Two approaches prevail in the open-channel-flow literature: the energetics approach, which seeks to relate the transport rate to the power expended by the stream on the bed (e.g. Bagnold, 1963); and the traction approach, which seeks to relate the transport rate directly to the bed shear stress (e.g. Einstein, 1950). The philosophy underlying the extension of steady-flow transport models to combined wave and current flow has been straightforward: steady-flow equations are assumed to apply to combined flow, provided that expressions for power or stress are replaced with expressions that are appropriate to combined flow. Thus, the fundamental difference between the two types of transport (steady-flow and combined-flow) lies in the generation of bed shear stress.

Typical of the energetics approach to combined-flow bedload transport is the work of Bailard and Inman (1981) in which Bagnold's (1963) steady-flow bedload theory was modified to apply to a steady longshore current superimposed on reversing wave-orbital velocities in the surfzone. Similar applications include those of Inman and Bagnold (1963), Komar (1971; 1977), Thornton (1973) and Bowen (1980). Pattiaratchi and Collins (1984) adapted the steady-flow energetics models of Sternberg (1972) and Gadd et al. (1978) to apply to combined wave and current flows on the continental shelf. Steady-flow total-load models have similarly been extended, e.g. Bailard's (1981) adaptation of Bagnold's (1963) total-load energetics model to the surfzone.

The traction approach to combined-flow bedload transport is well represented by Bijker's (1967; 1971) modification of Frijlink's (1952) steady-flow theory. Stress terms in Frijlink's equations were replaced with two components: a wave-induced component of the total stress, which represented increased stirring of the bed sediment by the waves, and a current component, which represented the current advection of sediment. Swart (1976) embraced the same approach, but used a more sophisticated theory of combined-flow shear stress to partition the total stress. Madsen and Grant (1976) proposed that the steady-flow transport equation of Einstein (1950) be extended using the theory of Jonsson (1966) for the combined-flow bed stress. Van der Graaf and van Overeem (1979) presented an analysis of several steady-flow total-load formulae (including those of Engelund and Hansen, 1967, and Ackers and White, 1973) that were modified to apply to combined flow.

Existing bedload transport models represent many variations on only a few themes; the selection of a transport model should be motivated not

only by validity of the model itself, but also by objectives of the analysis. Generally, the theory should accurately predict the local instantaneous transport rate, and this rate should be integrable over a wave period. Two other requirements are specifically applicable to this study: firstly, for the purposes of computing sediment-flux gradients, the transport rate should be readily expressed and treated as a vector quantity; and, secondly, since sediment may not be in motion over the whole wave period during low-energy conditions, the expression for the instantaneous transport rate should include a threshold criterion.

The combined-flow bedload transport model of Madsen and Grant (1976) is chosen for the basis of the present analysis because it either fulfills all of the above requirements, or can be modified to do so. A comprehensive theory of bed shear stress due to combined wave and current flow that was unavailable to Madsen and Grant will be used in the present formulation. Also, a threshold criterion will be explicitly included in a way that differs from the original formulation.

2.2 Bedload Transport by a Pure Wave

Madsen and Grant's (1976) combined-flow transport model was derived from a model of bedload transport by pure waves which was based on Einstein's (1950) and Brown's (1950) theories of steady, unidirectional bedload transport. Madsen and Grant (1976) re-interpreted the data of Abou-Seida (1965) and Kalkanis (1964), both of whom performed laboratory tests aimed at measuring the average rate at which sediment moves back and forth under pure waves. To this end, they had oscillated in sinusoidal fashion a tray of sediment that was suspended horizontally in

a tank of still water. Kalkanis' experiments were performed with a plane sediment bed; almost all of Abou-Seida's experiments were done with a rippled bed (Abou-Seida, 1965; Sleath, 1978; Hallermeier, 1982). During the motion of the plate, sediment was entrained as bedload and deposited in a trap situated in the center of the oscillating tray. Madsen and Grant interpreted the dry weight of sediment, W (units: $\text{g}\cdot\text{cm}/\text{s}^2$), caught in the trap during one half-wave cycle as the integral, over that half-wave cycle, of the instantaneous transport rate. Therefore, the average, over the half-wave cycle, rate of sediment transport by weight per unit width, \bar{q}_w (units: g/s^3), is:

$$\bar{q}_w = W / tb \quad (2.1)$$

where b is the width of the tray and the subscript "w" indicates that transport is due to a pure wave. The overbar indicates a time-averaged quantity. The average weight-rate of transport per unit width is converted to a volume-rate per unit width, \bar{Q}_w (units: cm^2/s), by dividing by $\rho_s g$ where ρ_s is the sediment density and g is the acceleration due to gravity. Madsen and Grant, following Einstein (1950), chose to non-dimensionalize \bar{Q}_w by dividing by wD , where w is the sediment settling velocity and D is the sediment grain size:

$$\bar{\phi}_w = \bar{Q}_w / wD \quad (2.2)$$

where $\bar{\phi}_w$ is the average, over a half-wave cycle, dimensionless rate of bedload sediment transport due to the pure wave.

Madsen and Grant found an empirical relationship between $\bar{\phi}_w$ and the maximum wave-induced skin-friction Shields parameter, $\psi'_{w,m}$:

$$\bar{\phi}_w = 12.5 \psi'_{w,m}{}^3 \quad (2.3)$$

where $\psi'_{w,m}$ is defined by:

$$\psi'_{w,m} = \tau'_{w,m} / (\rho_s - \rho_f)gD \quad (2.4)$$

and ρ_f is the fluid density, $\tau'_{w,m}$ is the maximum wave-induced skin friction (i.e. bed shear stress), the subscript "w" signifies the source as the wave, and the subscript "m" signifies the maximum value in the wave cycle. Skin friction is regarded as singly expressing the entraining force that acts on the bed sediment (see section 2.5); a bed shear stress that is a skin friction or another quantity that is derived from a skin friction is indicated by an apostrophe. Madsen and Grant deemed equation 2.3 valid for values of $\psi'_{w,m}$ "somewhat greater than" (Madsen and Grant, 1976, p. 38) the critical Shields parameter, ψ_{cr} , which is defined as:

$$\psi_{cr} = \tau'_{cr} / (\rho_s - \rho_f)gD \quad (2.5)$$

where τ'_{cr} is the threshold or critical skin friction, below which sediment remains attached to the bed. Horikawa et al. (1982) found a similar empirical expression relating $\bar{\phi}_w$ to $\psi'_{w,m}$, however Shibayama and Horikawa (1980) reported a value of 19 for the constant of proportionality in equation 2.3.

Madsen and Grant formally defined $\bar{\phi}_w$ by:

$$\bar{\phi}_w = 2/T \int_{-t_1}^{t_1} \phi_w(t) dt \quad (2.6)$$

where T is the wave period, $-t_1 < t < t_1$ is the interval during which transport in the positive (or negative) direction occurs, and $\phi_w(t)$ is the instantaneous dimensionless rate of bedload sediment transport.

Madsen and Grant proposed:

$$\begin{aligned} \phi_w(t) &= 40 [\psi_w'(t)]^3, \quad \psi_w'(t) \geq \psi_{cr} \\ &= 0, \quad \psi_w'(t) < \psi_{cr} \end{aligned} \quad (2.7)$$

where $\psi_w'(t)$ is the instantaneous wave-induced skin-friction Shields parameter:

$$\psi_w'(t) = \tau_w'(t) / (\rho_s - \rho_f)gD \quad (2.8)$$

and $\tau_w'(t)$ is the instantaneous wave-induced skin friction. Equation 2.7 was based on a "quasi-steady" application of the Einstein-Brown (Einstein, 1950; Brown, 1950) model of unidirectional steady-flow bedload transport. The term "quasi-steady" denotes a balance between stabilizing and entraining forces at every instant; the quasi-steady assumption derives from the assumption that sediment particles respond instantaneously to the time-varying bed shear stress.

Jonsson's (1966) model of pure-wave dynamics gives the maximum wave-induced skin friction, $\tau'_{w,m}$ as a function of flow parameters:

$$\tau'_{w,m} = 1/2 \rho_f f'_w |U_{w,m}| U_{w,m} \quad (2.9)$$

where f'_w is the skin-friction wave friction factor and $U_{w,m}$ is the maximum near-bed wave-orbital velocity, which, using linear wave theory, is given by:

$$U_{w,m} = \pi H / 2 \sinh(2\pi h/L) \quad (2.10)$$

where H is the wave height, L is the wavelength and h is the water depth. Jonsson's model is expanded to express the variation of wave-induced skin friction over a wave cycle as follows:

$$\tau'_w(t) = 1/2 \rho_f f'_w |U_w(t)| U_w(t) \quad (2.11)$$

(Wright et al., 1982), where $U_w(t)$ is the instantaneous near-bed wave-orbital velocity, which, using linear theory, is given by:

$$U_w(t) = U_{w,m} \cos(\omega t) \quad (2.12)$$

where $\omega = 2\pi/T$ is the wave radian frequency.

By substituting 2.11 and 2.12 into 2.8, an expanded expression for the instantaneous wave-induced skin-friction Shields parameter is obtained:

$$\psi'_w(t) = (\tau'_{w,m} / ([\rho_s - \rho_f]gD)) |\cos(\omega t)| \cos(\omega t) \quad (2.13)$$

$$= \psi'_{w,m} |\cos(\omega t)| \cos(\omega t) \quad (2.14)$$

Finally, substitution of 2.14 into 2.7 gives a general expression for the instantaneous dimensionless rate of bedload sediment transport by pure waves:

$$\phi_w(t) = 40 [\psi'_{w,m} \cos(\omega t) \cos(\omega t)]^3, \quad \psi'_w(t) \geq \psi_{cr} \quad (2.15)$$

$$= 0, \quad \psi'_w(t) < \psi_{cr}$$

The time-averaged dimensionless transport rate is obtained by integrating 2.15 in accordance with 2.6, which gives:

$$\bar{\phi}_w = C_1 \psi_{w,m}^3 \quad (2.16)$$

where $C_1 = f(\psi'_{w,m}/\psi_{cr})$. For $\psi'_{w,m} > -2\psi_{cr}$, $C_1 = 12.5$, which is in agreement with the empirical relationship already found (equation 2.3). This correspondence constitutes validation of the development leading to equations 2.7 and 2.15.

Equation 2.7 and its expanded form, 2.15, constitute the general bedload transport model that is applicable to pure waves. Adaptation of equation 2.7 to apply to other situations (e.g. superimposed current, asymmetric waves) hinges on modification of the expression for the instantaneous skin-friction Shields parameter.

The central assumption employed in the previous development is that the instantaneous transport responds without lag to changes in instantaneous bed shear stress. To ensure this, transport must be confined to a very thin layer near the bed; clearly such an assumption is invalid for suspended-load transport. Kobayashi (1982) used an identical assumption in a traction model of bedload transport on a sloping bed, as did Ballard (1981) in an energetics bedload-transport model applicable to the surfzone. Sleath's (1978) laboratory observations of $\phi_w(t)$ support the contention: Sleath found that the increase in erosion rate during the phase of waxing wave-orbital velocities mirrored the increase in sedimentation rate during the waning phase. Sleath also found that instantaneous transport leads the wave-orbital velocity by between 0 and $\pi/4$ (typically $\pi/10$), which value appears to be a complex and unclear function of several variables (Sleath, 1978).

Sleath (1978) used the data of Abou-Seida (1965) and Kalkanis (1964) together with new laboratory data to develop a new empirical expression relating $\bar{\phi}_w$ to $\psi_{w,m}^*$. Sleath chose to nondimensionalize \bar{Q}_w by dividing by ωD_s^2 , and found the following empirical relationship:

$$\bar{\phi}_w = 47 (\psi_{w,m}^* - \psi_{cr})^{1.5} \quad (2.17)$$

Note that Sleath explicitly included a threshold condition in the expression, having demonstrated experimentally the efficacy of the concept as applied to oscillatory flow (Sleath, 1978; 1984).

The fundamental difference between equations 2.17 and 2.3 is obvious: the instantaneous rate of bedload transport is proportional to

the sixth power of the orbital velocity in the Madsen and Grant model, and in Sleath's model the transport is proportional to roughly the cube of the orbital velocity. Vincent et al. (1981) pointed out that Sleath's model is closer in form to original steady-flow energetics models (e.g. Kachel and Sternberg, 1971; Heathershaw, 1981) and performed a novel re-interpretation of the laboratory data in an attempt to resolve the discrepancy. Vincent et al. defined an instantaneous bedload volume concentration, which has units of cm^3/cm^2 and which can be thought of as the thickness of the mobilized sediment layer. Vincent et al. developed an expression in which this parameter varied as the cube of the flow velocity, and tested this equation and Madsen and Grant's model (equation 2.7) against Manohar's (1955) data which were obtained by oscillating, in an asymmetrical fashion, a rippled quartz-sand bed suspended in a still-water tank. For large skin-friction Shields parameters, Madsen and Grant's model overpredicted the observed average transport; much better agreement with the data was obtained using Vincent et al.'s model. However, for low Shields parameters, Madsen and Grant's model gave better predictions. Einstein (1950) had earlier postulated that the power dependence varies with transport rate and found that at high rates, transport is proportional to the third or fourth power of the velocity; Hallermeier (1982) also concluded that the power dependence varies with the transport rate.

2.3 Extension of the Pure-Wave Transport Model to Transport by Combined Wave and Current Flow

2.3.1 Introduction

Equation 2.7, which is the general transport equation for pure oscillatory flow, can be extended to apply to combined wave and current flow by modifying the expression for the instantaneous skin-friction Shields parameter. To achieve this, a theory of combined-flow dynamics is required. Prior to this point, vector representation was unnecessary since all directions were implicit. Vector notation (symbolized by superscript " $\vec{}$ ") is used in the following development and thereafter wherever necessary. Symbols without this superscript represent quantities that are either intrinsically scalar or magnitudes of vector quantities.

2.3.2 Theory of combined-flow boundary-layer dynamics

When a steady current is superimposed on an oscillatory current, the bed shear stress exerted by each component of the combined flow is greater than that exerted by each component when acting alone (Smith, 1977; Grant and Madsen, 1979). The turbulent dissipation of energy by both components is said to be enhanced by a nonlinear interaction between the wave and the current. Early attempts at modelling combined-flow boundary-layer dynamics include those of Lundgren and Jonsson (1961) and Bijker (1966). Later, more detailed approaches include those of Smith (1977), Bakker and van Doorn (1978), Grant and Madsen (1979), Tanaka and Shuto (1981) and Christofferson and Jonsson (1985). The

various models differ primarily in the way the near-bed turbulent mixing intensities are reproduced. A common approach is the use of a two- or multiple-layer eddy viscosity distribution; of these models, that of Grant and Madsen (1979) is probably the most widely used. Grant and Madsen's model, though, has been criticised for being needlessly complex (Christofferson and Jonsson, 1985).

The combined-flow boundary-layer dynamics model to be used in this analysis is a two-layer, time-invariant eddy viscosity model that was developed by Larsen et al. (1981) and that is fundamentally similar to Grant and Madsen's better-known model. Larsen et al.'s model is chosen primarily for reasons of clarity and facility.

Larsen et al. define the driving flow as a linear superposition of a mean flow in the x direction and an oscillating flow, frequency ω , in the θ direction. That is, the oscillating flow and the mean flow subtend an acute angle θ . Larsen et al. treat the wave boundary layer as if it is embedded in the constant-stress (i.e. logarithmic) current boundary layer. Within the wave boundary layer, the turbulence is due to both the wave and the current, and the eddy viscosity in this layer, K_{wc} , is scaled by the total maximum friction velocity, $U_{*t,wc,m}$, and assumed to vary linearly with elevation above the bed:

$$K_{wc} = \kappa U_{*t,wc,m} z \quad (2.18)$$

where:

$$U_{*t,wc,m} = (\tau_{t,wc,m} / \rho_s)^{0.5} \quad (2.19)$$

and:

$$\hat{\tau}_{t,wc,m} = \hat{\tau}_{w,wc,m} + \hat{\tau}_{c,wc} \quad (2.20)$$

κ is von Karman's constant (= 0.41; Nowell, 1983) and z is the elevation above the bed. The subscript "w,wc" designates the source as the wave component of the combined flow and likewise "c,wc" designates the source as the current component of the combined flow. As previously, the subscript "m" signifies the maximum value in the wave cycle. Thus, $\tau_{w,wc,m}$ and $\tau_{c,wc}$ are the maximum wave-induced and current components respectively of the total maximum bed shear stress exerted by the combined flow, i.e. $\tau_{t,wc,m}$.

Above the wave boundary layer, which by definition is the potential-flow region for the wave, the turbulence is due to the current only. The eddy viscosity in this region, K_c , is scaled by the current friction velocity, $U_{*c,wc}$, which is also assumed to vary linearly with elevation above the bed:

$$K_c = \kappa U_{*c,wc} z \quad (2.21)$$

where:

$$U_{*c,wc} = (\tau_{c,wc} / \rho_f)^{0.5} \quad (2.22)$$

The mean-current profile within and above the wave boundary layer is given by:

$$U_c(z) = (U_{*c,wc}^2 / \kappa U_{*t,wc,m}) \ln(z/z_0), \quad z < \delta_w \quad (2.23)$$

$$U_c(z) = (U_{*c,wc} / \kappa) \ln(z/z_1), \quad z > \delta_w \quad (2.24)$$

where, by definition, z_0 is the elevation above the bed where the mean flow, U_c , vanishes. δ_w is the wave boundary-layer thickness defined by Larsen et al. as:

$$\delta_w = U_{*t,wc,m} / \omega \quad (2.25)$$

The term z_1 in equation 2.24 is evaluated by matching equations 2.23 and 2.24 across the top of the wave boundary layer, which gives:

$$z_1 = z_0^B \delta_w^{1-B} \quad (2.26)$$

where:

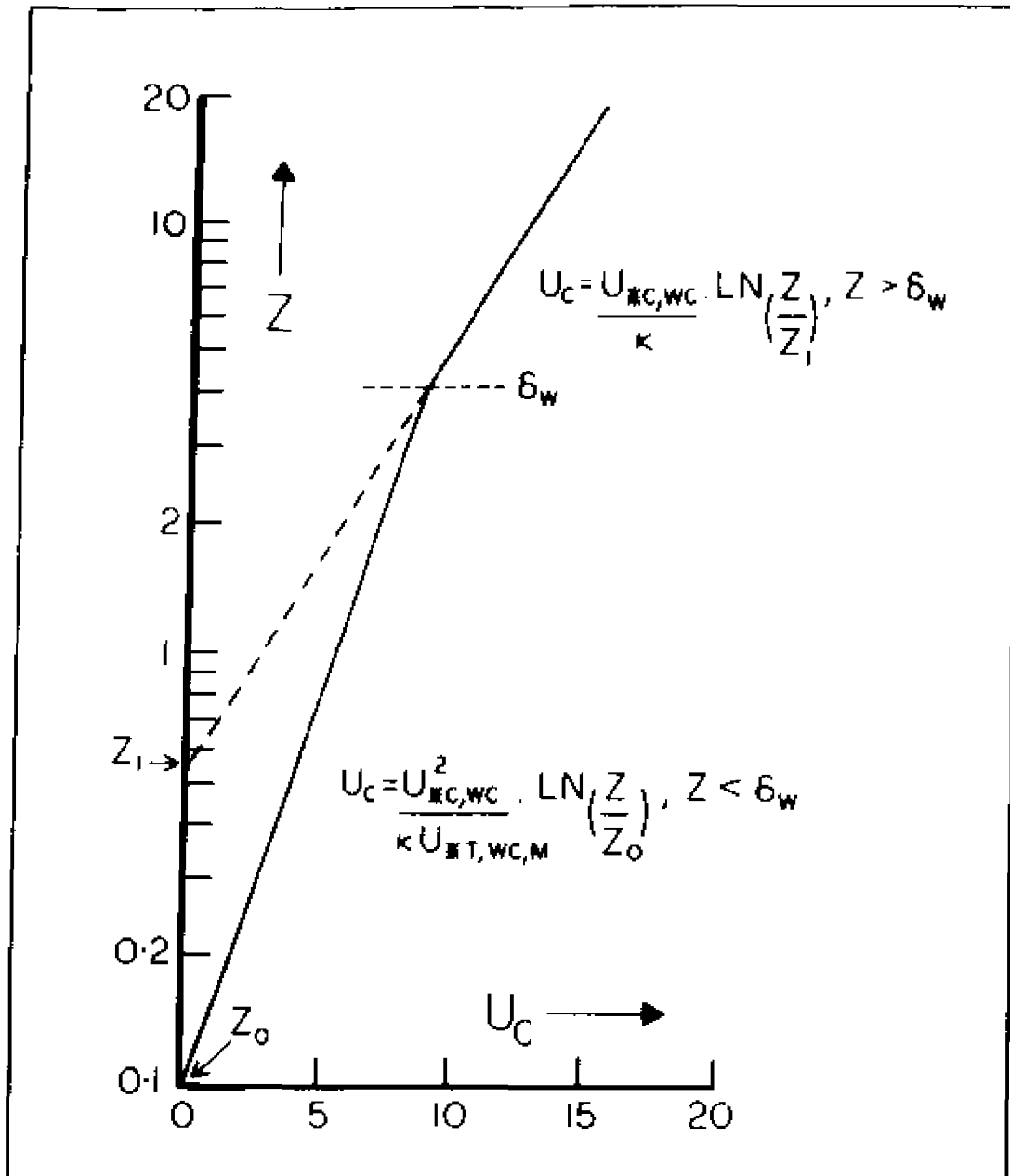
$$B = U_{*c,wc} / U_{*t,wc,m} \quad (2.27)$$

z_1 is the elevation at which U_c appears to vanish from above $z = \delta_w$ (Figure 2.1).

The total maximum friction velocity, $U_{*t,wc,m}$, is given by:

$$U_{*t,wc,m} = \left(U_{*c,wc}^4 + 2 \kappa U_{*c,wc}^2 U_{*t,wc,m} U_{w,m} G^2 \cos(\omega) + \kappa^2 U_{*t,wc,m}^2 U_{w,m}^2 G^4 \right)^{0.25} \quad (2.28)$$

Figure 2.1 Vertical profile of the mean component of the combined wave and current flow (equations 2.23 and 2.24). The parameters are: $z_0 = 0.1$ cm; $\omega = 0.63$ rads/s. z_1 is the elevation at which U_0 appears to vanish from above $z = \delta_w$.



where:

$$G^2 = (\xi_0/2) \{ [\text{Ker}_1^2(\xi_0) + \text{Kei}_1^2(\xi_0)] / [\text{Ker}^2(\xi_0) + \text{Kei}^2(\xi_0)] \}^{0.5} \quad (2.29)$$

and:

$$\xi = 2 [\omega z / (\kappa U_{*t,wc,m})]^{0.5} \quad (2.30)$$

$$\xi_0 = 2 [\omega z_0 / (\kappa U_{*t,wc,m})]^{0.5} \quad (2.31)$$

Ker and Kei are the Kelvin functions of the second kind and zero order, and Ker₁ and Kei₁ are the Kelvin functions of the second kind and first order (Abramowitz and Stegun, 1964).

$U_{*t,wc,m}$ and $U_{*c,wc}$ are solved for as follows. Given $U_c(z)$, z , $U_{w,m}$, ω , θ and z_0 (see section 2.5), a starting value of $r_{c,wc}$ is estimated using, for example, the quadratic drag law (Komar, 1976) with an approximate drag coefficient (e.g. 3×10^{-3} , Sternberg, 1972).

$U_{*t,wc,m}$ is solved for iteratively from equations 2.28 and 2.29; equations 2.23 and 2.24 are then used to predict $U_c(z)$. If the predicted $U_c(z)$ differs significantly from the observed $U_c(z)$, a new value of $U_{*c,wc}$ is estimated using the method suggested by Shi et al. (1985):

$$U_{*c,wc} [\text{new}] = \{ U_{*c,wc} [\text{old}] U_c(z)_{[\text{observed}]} \} / U_c(z)_{[\text{predicted}]} \quad (2.32)$$

and the procedure is repeated until acceptable agreement between $U_c(z)$ [predicted] and $U_c(z)$ [observed] is achieved. Finally, the wave component of the total combined-flow bed shear stress is solved for using equation 2.20.

The total combined-flow bed shear stress, and the two components thereof, may be interpreted as skin frictions if z_0 is appropriately defined (see section 2.5); for the purposes of the remainder of this development, it is assumed that z_0 is thus defined.

The wave and current components of the total bed shear stress exerted by the combined flow are enhanced over their respective pure-flow values, which can be demonstrated by defining a "combined-flow skin-friction wave friction factor", $f'_{w,wc}$:

$$f'_{w,wc} = \tau'_{w,wc,m} / 0.5 \rho_f U_{w,m}^2 \quad (2.33)$$

and examining its behaviour. In the limiting case of the wave-current model (i.e. $U_c = 0$), $f'_{w,wc}$ is equivalent to f'_w (Figure 2.2). With a current superimposed, the ratio $f'_{w,wc}/f'_w$ exceeds unity, where that ratio is equivalent to $\tau'_{w,wc,m}/\tau'_{w,m}$ and therefore indicative of the enhancement of the wave-induced stress by the current (Figure 2.3). The ratio $f'_{w,wc}/f'_w$ increases with an increase in the superimposed mean-current speed and also with a decrease in angle between the wave and the current. The effect of the wave on the current component of the total stress can likewise be demonstrated: the ratio $\tau'_{c,wc}/\tau'_c$ increases with increasing $U_{w,m}$ and is greatest for collinear flow.

Figure 2.2 Wave friction factor plotted as a function of the relative roughness, k/A , where k is the boundary roughness and A is the near-bed orbital semi-excursion (see section 2.5). The three cases plotted are: the limiting case ($U_c = 0$) of the Larsen et al. (1981) combined-flow model; the limiting case of the Grant and Madsen (1979) combined-flow model; and Swart's (1974) explicit approximation to Jonsson's (1966) implicit pure-wave theory.

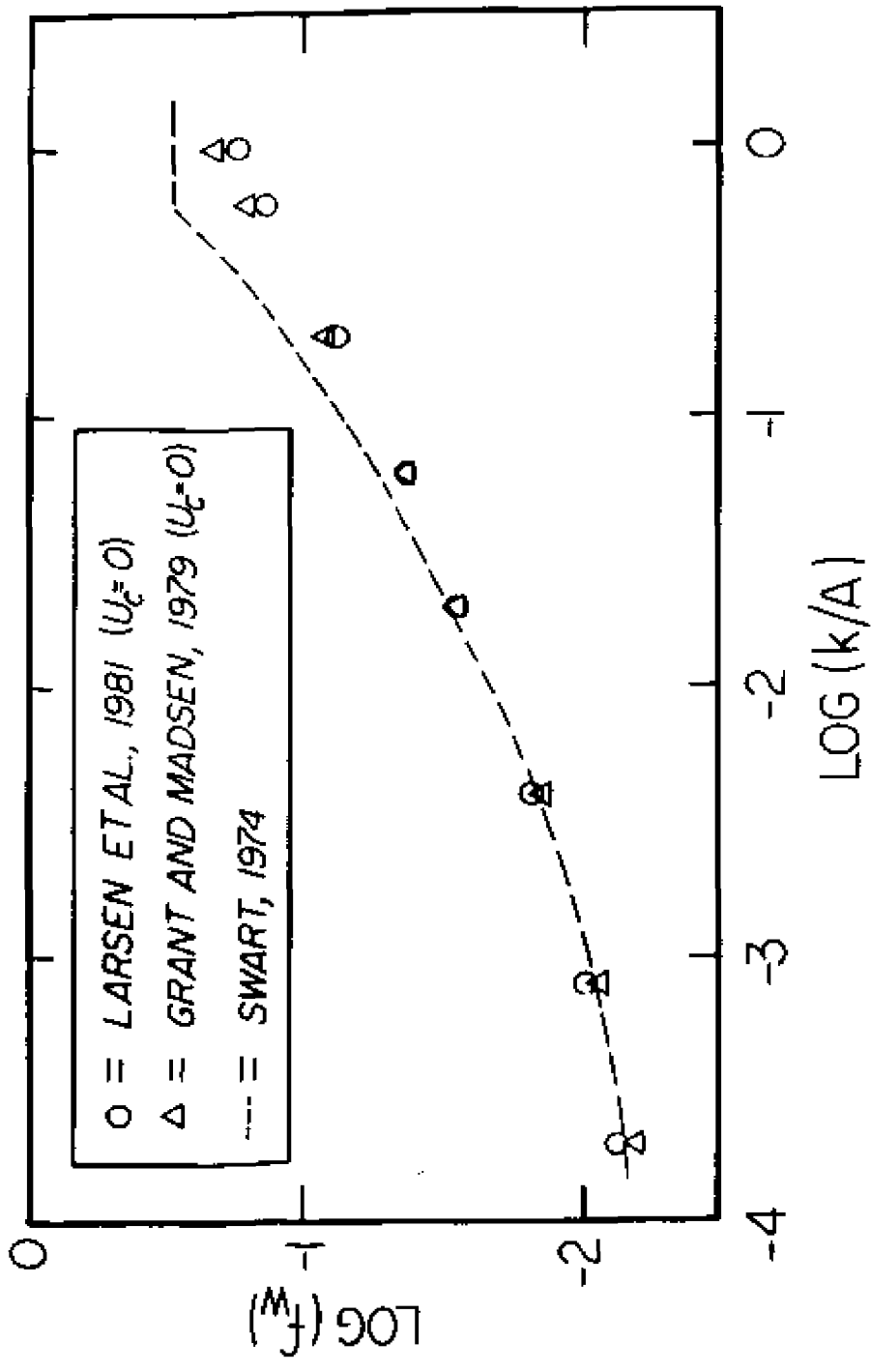
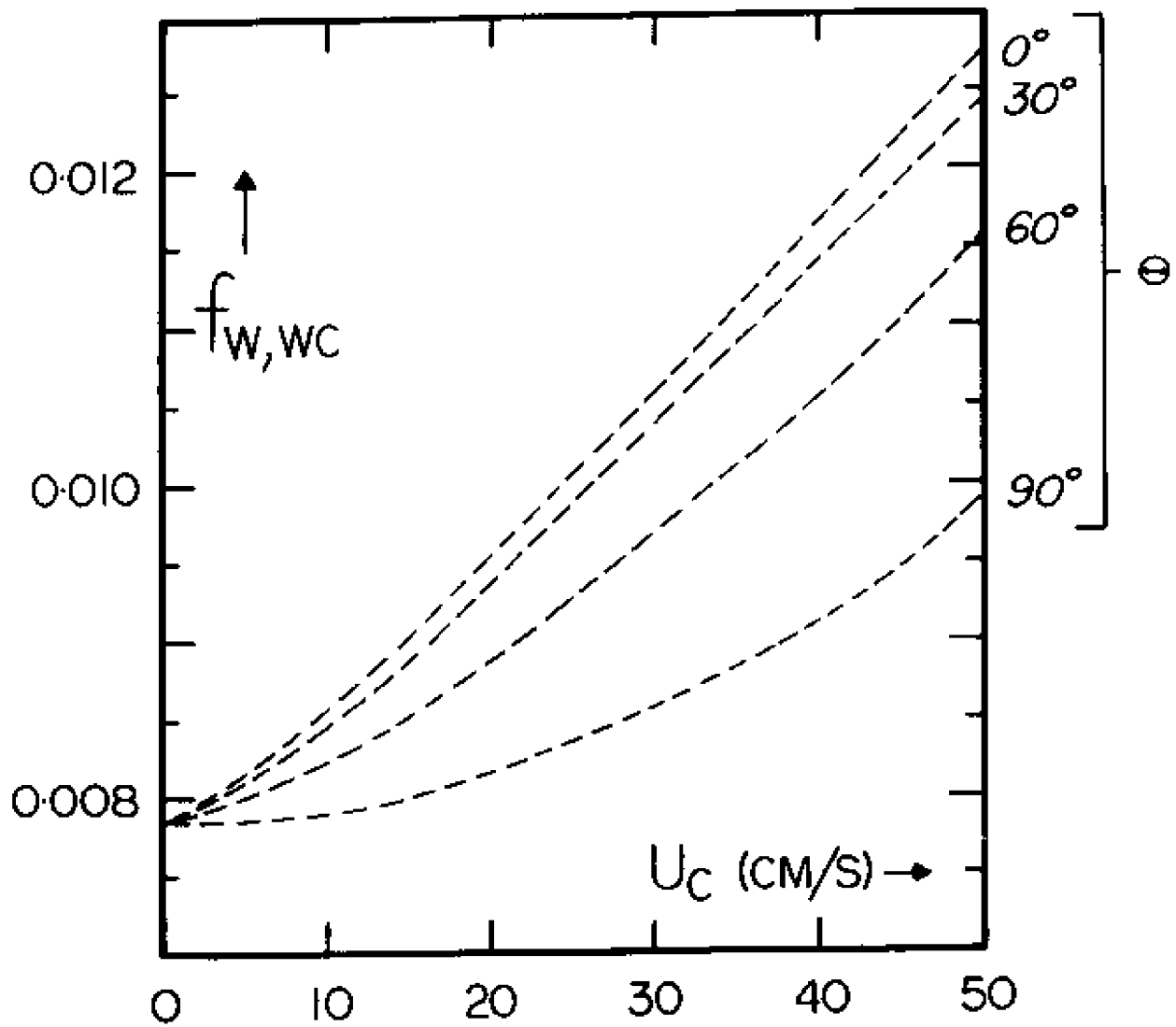


Figure 2.3 Variation of $f_{w,wc}$ with U_c and θ for a 10-s period wave and a relative roughness (k/λ) of 0.0004. $f_{w,wc}$ is equal to f_w when $U_c = 0$. The ratio $f_{w,wc}/f_w$ increases with increasing U_c and is greatest for collinear flow ($\theta = 0$) for any given U_c .



2.3.3 Bedload transport by combined wave and current flow

The time-variation of the wave component of the total skin friction is given by:

$$\hat{\tau}'_{w,wc}(t) = \hat{\tau}'_{w,wc,\pi} |\cos(\omega t)| \cos(\omega t) \quad (2.34)$$

and the combined-flow skin-friction Shields parameter by:

$$\hat{\psi}'_{wc}(t) = \hat{\tau}'_{t,wc}(t) / (\rho_s - \rho_f) g D \quad (2.35)$$

where:

$$\hat{\tau}'_{t,wc}(t) = \hat{\tau}'_{w,wc}(t) + \hat{\tau}'_{c,wc} \quad (2.36)$$

(Shi et al., 1985). The instantaneous bedload transport under combined flow is found by replacing the pure-wave skin-friction Shields parameter in equation 2.7 with the Shields parameter appropriate to the combined flow to obtain:

$$\hat{\phi}'_{wc}(t) = 40 [\hat{\psi}'_{wc}(t)]^3, \quad \psi'_{wc} \geq \psi_{cr} \quad (2.37)$$

$$= 0, \quad \psi'_{wc} < \psi_{cr}$$

Finally, net dimensionless transport, $\hat{\phi}'_{wc}$, is found by integrating equation 2.37 over the whole wave period:

$$\hat{\phi}_{wc} = 1/T \int_0^T \hat{\phi}_{wc}(t) dt \quad (2.38)$$

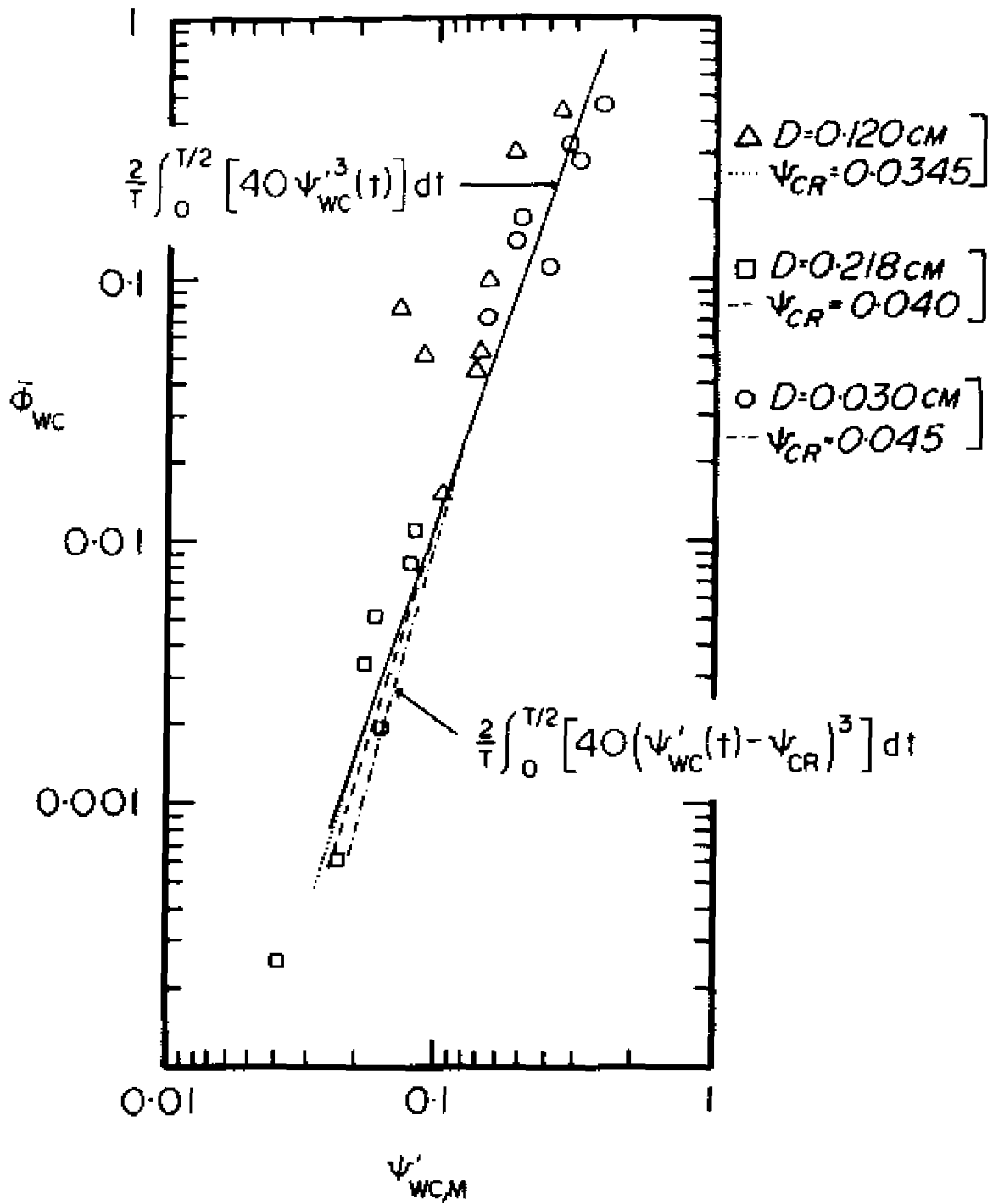
For low-energy conditions, in which sediment may not be in motion over the whole wave cycle, a threshold criterion should be included in the expression for the instantaneous transport in order to ensure acceptable asymptotic behaviour. Seymour (1985) proposed a simple and universally applicable method for including a threshold criterion in any transport model. Seymour's objective was to defeat the analytical complexities that are introduced by forcing the transport to lose its velocity dependence when the skin friction falls below threshold. This was achieved by deliberately introducing a small error into the final estimate of the average transport rate. The driving term in equation 2.37 can be simply converted to the "excess skin friction" (i.e. skin friction in excess of critical stress) as follows:

$$\hat{\phi}_{wc}(t) = 40 [\hat{\psi}'_{wc}(t) - \psi_{cr}]^3, \quad \psi'_{wc} \geq \psi_{cr} \quad (2.39)$$

$$= 0, \quad \psi'_{wc} < \psi_{cr}$$

at the expense of introducing a small error that is reflected in the average transport rate under the combined flow, $\bar{\phi}_{wc}$, which is defined as the integral over a half-wave cycle of the instantaneous transport rate with the current component of the total skin friction set to zero. The difference between $\bar{\phi}_{wc}$ calculated from 2.37 and from 2.39 is demonstrated in Figure 2.4 for various values of ψ_{cr} . For large $\psi'_{wc,m}/\psi_{cr}$, where $\psi'_{wc,m}$ is the maximum combined-flow skin-friction

Figure 2.4 $\bar{\phi}_{wc}$ calculated from 2.37 (general equation for combined-flow transport) and from 2.39 (general equation with driving term converted to excess skin friction) for various values of ψ_{cr} . For large $\psi'_{wc,m}/\psi_{cr}$, the two equations provide almost identical values of $\bar{\phi}_{wc}$; for small $\psi'_{wc,m}/\psi_{cr}$, the disparity is greater, but less than the spread of the original data points used to develop the transport expressions.



Shields parameter, the two equations provide almost identical values of $\bar{\phi}_{wc}$; for small $\psi'_{wc,m}/\psi_{cr}$, the disparity is greater, but less than the spread of the original data points used to develop the transport expressions.

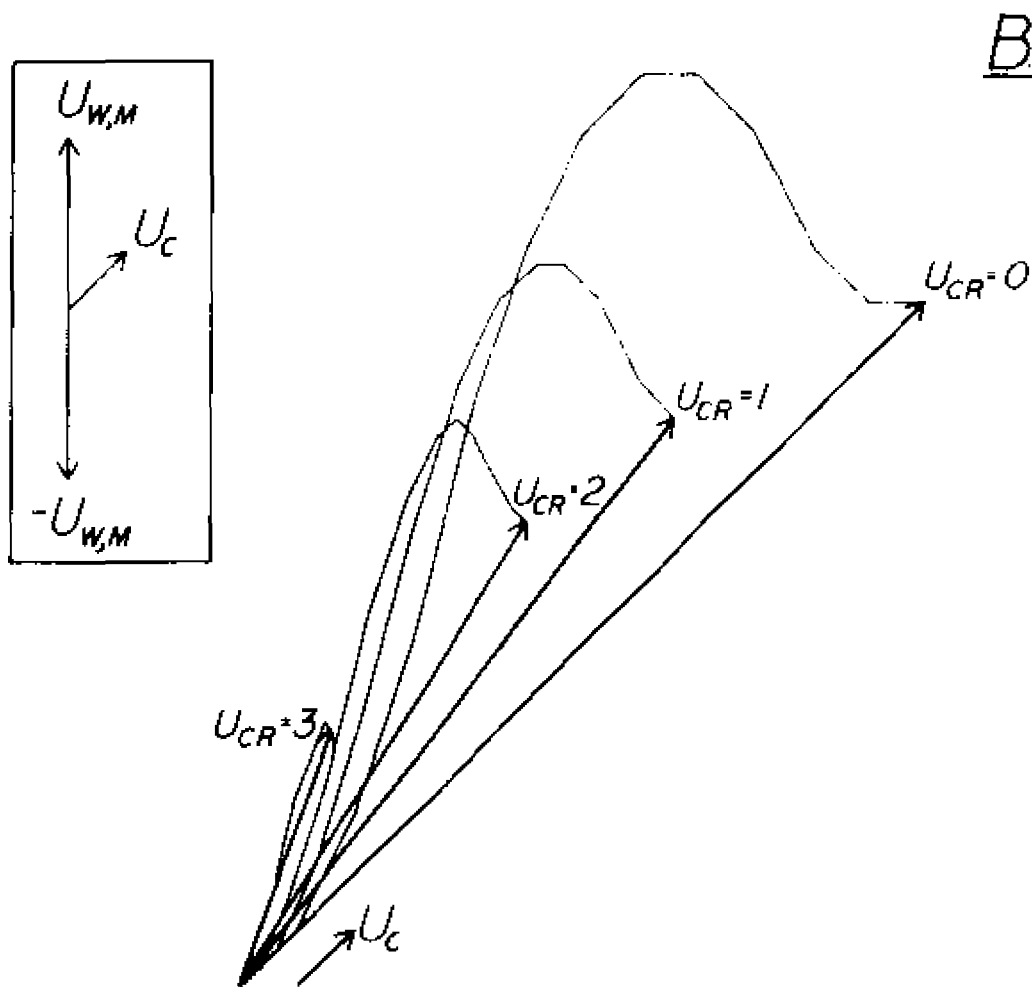
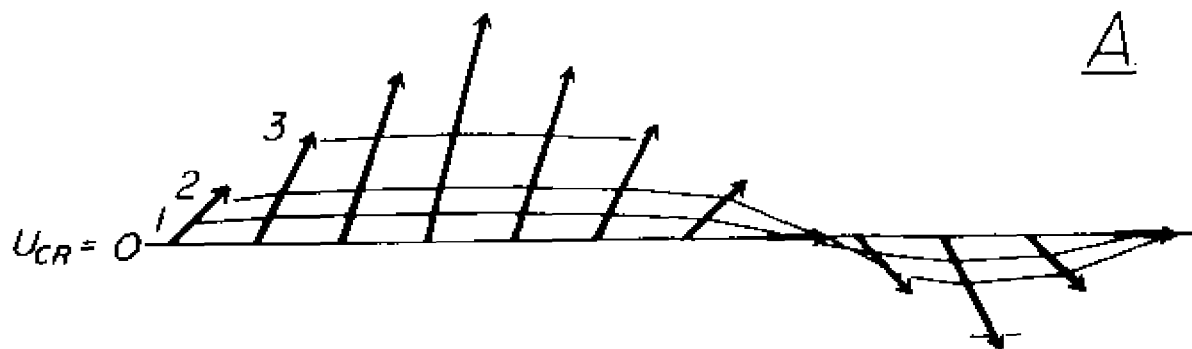
There is an important consequence of converting the driving term to the excess skin friction: the threshold criterion in combination with the combined flow causes an asymmetry in $\hat{\phi}_{wc}(t)$, and consequently net sediment transport may not be aligned with the mean current. This is demonstrated graphically in Figure 2.5. In Figure 2.5.A, combined-flow velocity vectors (sum of a sinusoidally-varying wave component and a steady current component) at twelve instants over a wave period are depicted. Four different threshold levels (including zero) are superimposed on the velocity plot. In Figure 2.5.B, progressive additions of the velocity in excess of each threshold level are plotted; resultant displacements, over the wave period, corresponding to each of the four threshold levels are also shown. For zero threshold, net displacement parallels the original current. As threshold increases, the resultant displacement turns in the direction of the wave stroke that makes an acute angle with the current. For the special case of orthogonal wave and current, it can be shown that net displacement is always parallel to the current.

The translation of this concept to fluxes of sediment is complicated by the power dependences involved, but the results are exactly analogous: net bedload transport is turned away from the mean current towards, but not beyond, that stroke of the wave that makes an acute angle with the current. As the ratio $\psi'_{wc,m}/\psi_{cr}$ decreases, the net transport vector turns more in the direction of the wave, and vice

Figure 2.5 Effect of including a threshold condition in the general transport equation on net transport direction.

A. Addition of a sinus wave velocity and a steady velocity at twelve instants over a wave period. Also depicted are four different threshold velocity levels.

B. Progressive additions of the combined velocity that is in excess of each threshold. The resultant displacements (heavy lines) are not necessarily aligned with either the wave or the current component of flow.



versa. For large $\psi'_{wc,m}/\psi_{cr}$ and for the special case of orthogonal wave and current, net transport is in the direction of the current.

Calculating sediment flux from mean-flow quantities instead of time-integrating the instantaneous sediment flux obscures possible wave control over the direction of net sediment flux. For example, integrating the product of the vertical time-mean sediment-concentration and velocity profiles (e.g. Lees, 1981; Wright, 1981) results in a net flux of suspended sediment that can only parallel the mean current. The concept of bedload flux as the mean-current advection of sediment that is entrained from the bed by waves as bedload is analogous. The present analysis demonstrates that, in a combined wave and current flow, partial control by the wave over the direction of net transport is admitted by including a threshold criterion in the formulation of the instantaneous transport rate and by integrating the instantaneous rate to obtain the net flux.

2.4 Effect of Wave Asymmetry

Finite-amplitude waves are rarely symmetrical. Rather, natural waves are asymmetrical about the still-water level such that troughs are flattened and crests are peaked. Linear wave theory under such circumstances is not a useful model of the water-surface displacement or of the wave-orbital velocities (equation 2.12). According to Stokes' second-order finite-amplitude wave theory (LeMehaute, 1976), the maximum forward (i.e. in the direction of wave propagation) wave-orbital velocity exceeds the maximum reverse velocity, and the reverse stroke persists for longer than $T/2$:

$$U_w(t) = \frac{H\omega}{2\sinh(2\pi h/L)} \cos(\omega t) + \frac{3\pi H/L}{4\sinh^3(2\pi h/L)} \cos(2\omega t) \quad (2.40)$$

The asymmetry of the wave-orbital velocities causes an asymmetry in the instantaneous bedload transport rate that is magnified because of the transport rate's nonlinear dependence on the wave-orbital velocity; more sediment is moved forward under the brief but intense forward stroke of the wave, resulting in net transport that is in the direction of wave propagation. Madsen and Grant (1976) extended the general equation for bedload transport (equation 2.7) to apply to asymmetric waves by replacing the linear expression for the wave-orbital velocity (equation 2.12) with the second-order expression (equation 2.40). Manohar's (1955) laboratory observations of transport under asymmetric oscillatory velocities were used to verify the transport model.

2.5 Estimation of z_0

The elevation above the bed at which both components of the combined flow vanish, z_0 , must be known in order to use the dynamics equations. When the flow is rough turbulent, z_0 is given by:

$$z_0 = k / 30 \quad (2.41)$$

(Smith, 1977), where k is the equivalent sand roughness of the boundary or simply the boundary roughness. When the flow is fully rough turbulent, the boundary roughness non-dimensionalized by the appropriate length scale of the flow (which ratio is the relative roughness)

uniquely defines the friction or drag coefficient. For the case of wind waves, the appropriate length scale is the near-bed orbital semi-excursion:

$$A = U_{w,m} / \omega \quad (2.42)$$

(Jonsson, 1966). The roughness of a flat sand bed under oscillatory flow is composed entirely and only of the grain roughness, k_G , which is given by:

$$k_G = C_2 D_n \quad (2.43)$$

where D_n is the grain size that is greater than $n\%$ of the grains that compose the bed. For a smooth, flat sand bed, $C_2 = 1$ and $n = 50$ (Madsen and Grant, 1976; Hsiao and Shemdin, 1979); for a slightly irregular flat bed, $C_2 = 2.5$ and $n = 50$ may be used (Engelund and Hansen, 1972).

Kamphuis (1975) recommended $C_2 = 2$ and $n = 90$, which Davies (1985) used with good results.

Bed stress that is scaled by grain roughness is skin friction, which is defined as the tangential stress exerted by the flow on the bed averaged over a few tens of grain diameters (Chriss and Caldwell, 1982). Skin friction is regarded as singly expressing the sediment-entraining force (Dyer, 1980; Lofquist, 1980; Chriss and Caldwell, 1982); inertia forces were shown to be unimportant by Madsen and Grant (1976) and Nielsen (1979), however, Sleath (1978) noted that "forces other than skin friction [i.e. lift] are probably important [in entraining sediment] under certain conditions" (p. 301).

A natural, loose-sand bed acted upon by waves is rarely flat; typically, the bed is covered by wave-generated ripples. The streamlines close to the bed are bent by the deformed surface causing a variation in dynamic pressure over the ripple profile. The integral over the length of the ripple of the horizontal component of the dynamic pressure results in a force that is directed adversely to the flow (Lofquist, 1980), which force is known as form drag. In this way, ripples act as roughness elements which generate a drag that contributes only to dissipation of flow energy; form drag contributes nothing to the force that entrains sediment from the bed (Dyer, 1980; Chriss and Caldwell, 1982).

The boundary layer above a rippled bed is segmented: very close to the bed, flow is retarded by skin friction alone, and above this, the flow is retarded by both skin friction and form drag. Davies (1985) showed that, in oscillatory flow, form drag may be orders of magnitude greater than skin friction. Chriss and Caldwell (1982) demonstrated that unwittingly including form drag in sediment-transport calculations will lead to large errors. This is a real possibility, since current measurements are typically made above the very thin internal boundary layer in the region where the velocity shear reflects both components of the stress.

Lofquist (1980) showed that there is no way of analytically separating skin friction and form drag. To scale the form drag, an empirical ripple roughness, k_R , which is analogous to the grain roughness, is usually employed. Grant and Madsen (1982) proposed the following model that related k_R to the dimensions of the wave-generated ripples:

$$k_R = C_3 (n^2 / \lambda) \quad (2.44)$$

where n is the wave-ripple height, λ is the wave-ripple length, and the value of C_3 was determined experimentally to be 27.7. Nielsen (1983) adopted the same model but found that $C_3 = 8$ gave a better fit to available laboratory data.

The skin-friction component of the total drag over a rippled bed may be estimated by treating the problem as though the bed were flat: the observed velocity (above the internal boundary layer) is used in the stress calculation, and the grain roughness is used to scale the friction coefficient. The velocity thus used is assumed to be unaffected by form drag: clearly, this assumption can lead to errors in estimation of skin friction if the form drag is in fact significant. Nevertheless, both Madsen and Grant (1976) and Davies (1980) have demonstrated the validity of this approach. If the flow over the ripple crests is not separating, potential-flow theory can be used to relate the observed velocity far from the bed to the velocity in the internal boundary layer (e.g. Davies, 1984), thus eliminating the problem. Other stress-partitioning schemes, e.g. Smith (1977), are not applicable to single-point velocity observations.

The term z_1 , which is the elevation at which the mean current appears to vanish when viewed from above $z = \delta_w$, is analogous to z_0 and is termed the apparent roughness. Whereas z_0 reflects the influence of the bed on turbulent energy-dissipation in the flow, the apparent roughness reflects both the influence of the bed and of the wave-current interaction within the wave boundary layer on the drag felt by the mean flow above $z = \delta_w$. Recent detailed boundary-layer measurements support

the concept of an apparent roughness (e.g. Cacchione and Drake, 1982; Grant et al., 1983; Wiberg and Smith, 1983; Grant et al., 1984), as do recent laboratory measurements (e.g. Kemp and Simons, 1983).

In conclusion, the general transport equation (2.7) is valid for both plane and rippled beds provided the total drag is properly partitioned into skin-friction and form-drag components, and only the skin friction is used in the transport calculations.

3. METHODOLOGY AND DATA ANALYSIS

3.1 Introduction

Three experiments were conducted on the shoreface that fronts the community of Duck on the Outer Banks of North Carolina in the southern Mid-Atlantic Bight (Figure 1.1). During each experiment, near-bed currents at a single location on the shoreface were measured, and during one experiment, changes in relative bed elevation were also recorded. All measurements were made during low-energy (fairweather) conditions. In Chapter 3, the physical setting of the shoreface is presented as background to the experimental observations, the experimental methodology is described, and measured kinematic quantities (current velocities) are converted into dynamic quantities (stresses) and ultimately into bedload fluxes using the theory detailed in Chapter 2. The model calculations are subsequently used in Chapter 5 to investigate the role of velocity moments in controlling low-energy bedload flux on the shoreface.

3.2 Physical Setting of the Duck Shoreface

3.2.1 Surficial geology

The Outer Banks is a chain of narrow, unconsolidated sand barrier islands situated in the southern Mid-Atlantic Bight of North America. The experiments were conducted on the shoreface seaward of the U.S. Army Corps of Engineers Field Research Facility (FRF) at Duck (Figure 1.1). The FRF (latitude $36^{\circ} 11.0' N$, $75^{\circ} 44.8' W$) is located approximately halfway between Cape Hatteras in the south and the entrance to Chesapeake Bay in the north.

Geophysical surveys were conducted with the objective of defining the spatial and temporal variability in relief, bedforms and surface sediments (together, the "surficial geology") of the shoreface. The description that follows is intended to guide the reduction and interpretation of the velocity data.

High-resolution side-scan sonar and bathymetric surveys of the shoreface and adjacent inner shelf were conducted on three separate occasions: July, 1984; October, 1984; and July, 1985. All surveys were run during fairweather. An EG&G Model SMS 960 side-scan sonar was used to acquire acoustic imagery of the seabed. The imagery is composed of sixteen discrete gray scales which represent different intensities of acoustic backscattering from the seafloor; the intensity of backscattering depends on the seafloor "roughness" (both sediment texture and bedforms). At the selected range, 100 m either side of the vessel was being surveyed, which provided a maximum resolution of about

0.25 m. A distinctive acoustic signature, interpreted by direct observation ("groundtruth"), may be generated by assemblages of smaller-scale features and sediment textures. The imagery, automatically corrected during acquisition for slant range of the side-looking sonar, was recorded on magnetic tape for post-survey processing. Post-survey processing included correction of imagery scale for actual ship speed and amplification and enhancement of selected bed features. Groundtruth was obtained by divers during the survey and on several other occasions between July, 1984, and July, 1985.

A Raytheon Model DE719 high-resolution depth sounder was deployed simultaneously with the side-scan sonar. Bathymetric profiles, which correspond to the center line of the swaths of acoustic imagery, were digitized at 10-m intervals, corrected for tide and draft, and redrawn at appropriate scales. The vertical accuracy of the resulting point-depths varies with the sea-state at the time of survey; after filtering of high-frequency (surface-wave) noise, the error was reduced to an estimated ± 20 cm.

LORAN-C was used for navigation control. Position fixes were taken every 150 m along pre-determined tracklines. In open, coastal waters the accuracy of LORAN-C is approximately ± 20 m; positional accuracy was later verified during preparation of sonograph mosaics. A unique feature of the surveys, intended to resolve the spatial distribution and continuity of bed morphology, was the use of trackline grids designed to provide overlapping acoustic coverage (50% between adjacent swaths) of a large area (1.5 km by 1.5 km). Grid coverage of the upper shoreface just seaward of the outer bar (~ 8 -m water depth), the shoreface in mid-depths (10 to 15-m), and the inner shelf at the seaward base of the

shoreface (-22-m) was obtained. Long shore-normal and shore-parallel transects extended the coverage and provided tie-ins. Tracklines sailed on the three separate cruises are shown in Figure 3.1.

One shore-normal bathymetric profile, surveyed to 10-km offshore in July, 1984, and two profiles surveyed to 5-km offshore in October, 1984, are shown in Figure 3.2.A. The smooth, concave-upwards profile, which is diagnostic of the shoreface (e.g. Niedoroda et al., 1985), extends approximately 5 km offshore to a depth of -22 m. The superposition of the three profiles, which are separated in the longshore dimension by several kilometers, is evidence of longshore uniformity in bathymetry. Williams (1983) described two profiles, one 18 km to the north of the FRF and one 18 km to the south, that demonstrated uniformity over even larger longshore separations. On a larger scale, Everts (1978) showed that the depth of the base of the shoreface increases towards the south in the southern Mid-Atlantic Bight. Regions where clusters of closely spaced ridges merge with the shoreline at oblique angles in shallow depths (-4 m) are exceptions to the typical profile shape; such "shoreface-connected ridges" occur at four locations in the southern Mid-Atlantic Bight (Swift et al., 1978).

Extending seaward from the base of the shoreface is the inner shelf, which, in the vicinity of Duck, is characterized by a complex pattern of relief associated with a field of large sand ridges (Green, 1986). The distinction between the shoreface and the inner shelf is reinforced by comparing topographies. The uniform, concave bow of the shoreface is a stark contrast to the ordered but highly variable, in both the longshore and cross-shore dimensions, relief of the sand-ridge field of the adjacent inner shelf (Figure 3.2.B).

Figure 3.1 Survey lines; July 1984, October 1984, and July 1985 cruises.

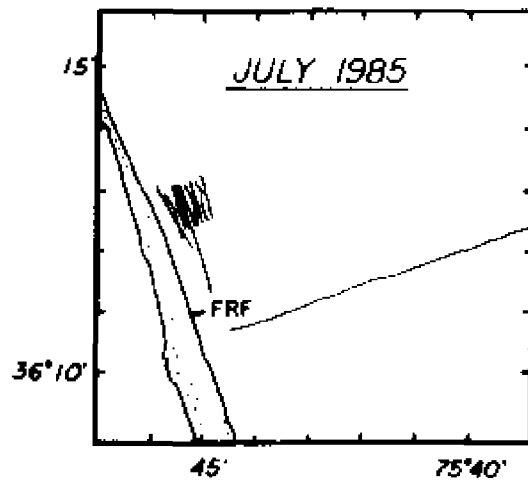
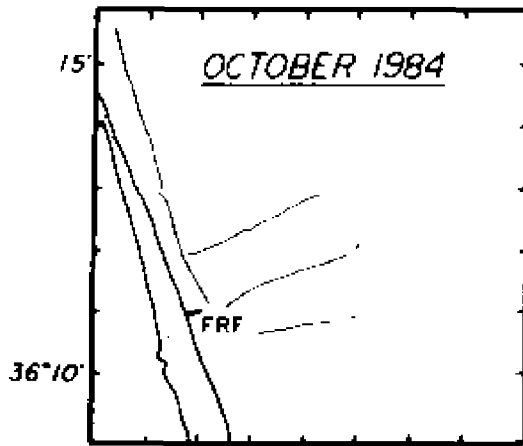
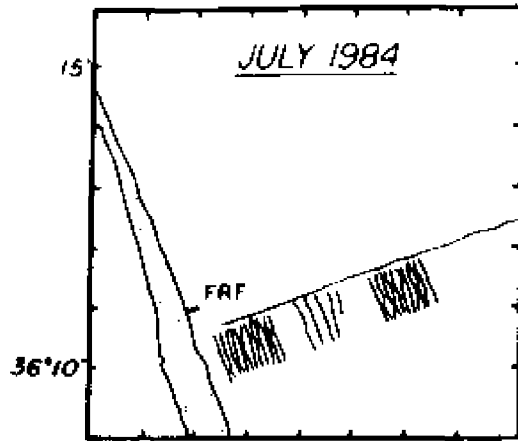
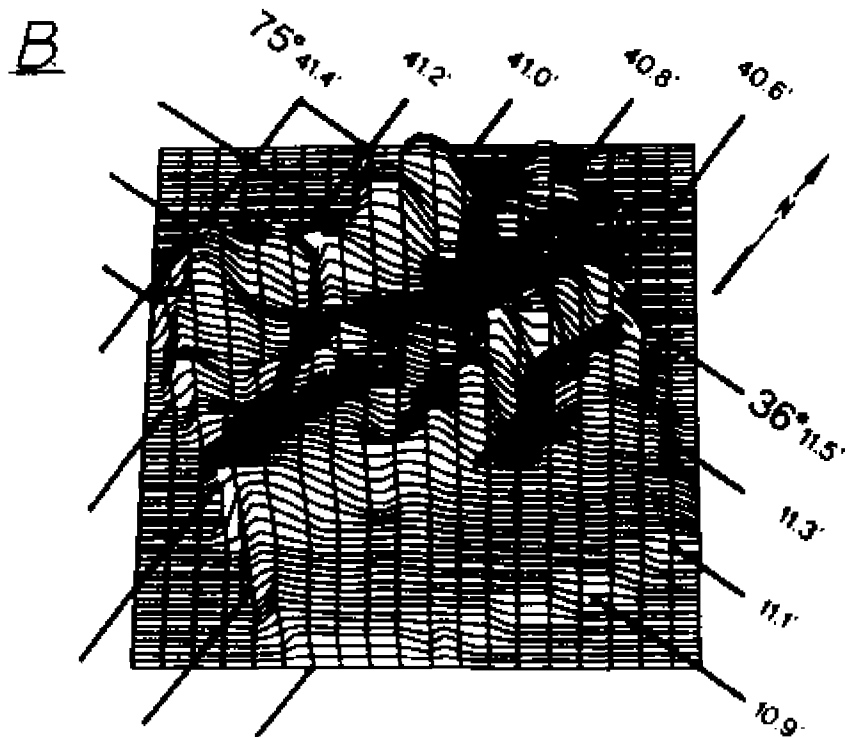
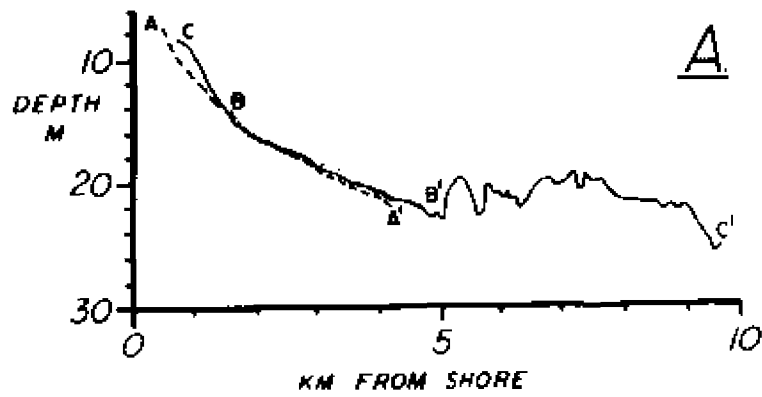
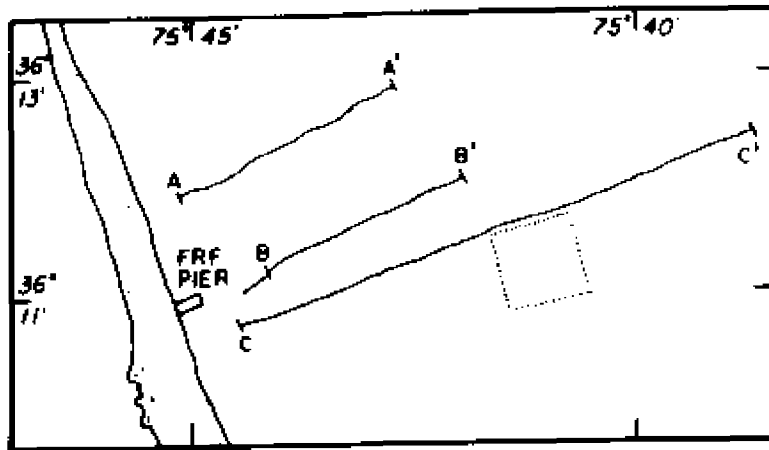


Figure 3.2 A. Shore-normal bathymetric profiles of the shoreface and adjacent inner shelf in the vicinity of the FRF at Duck, North Carolina.

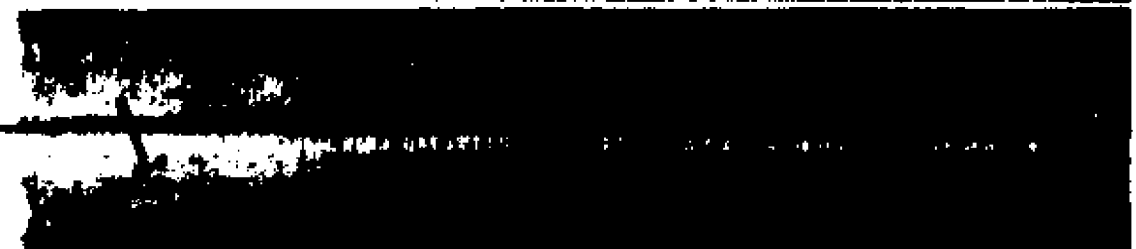
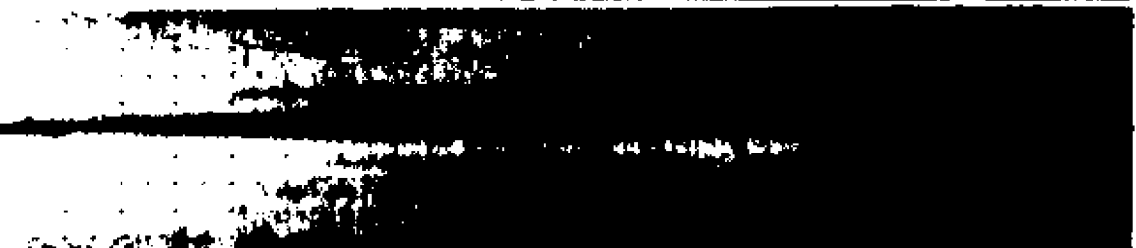
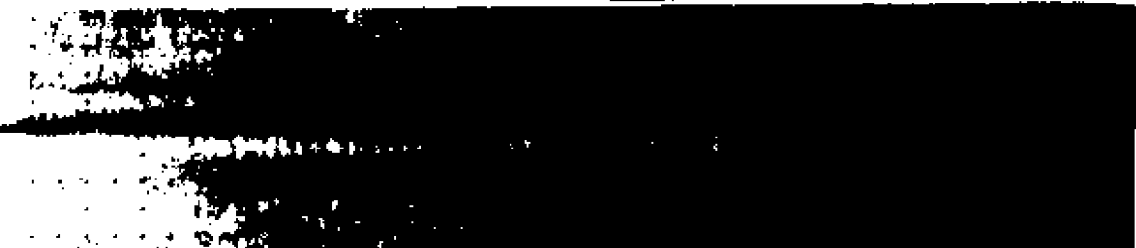
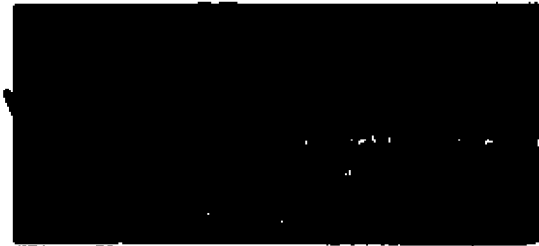
B. Perspective view of the bathymetric relief of the inner-shelf sand-ridge field seaward of the FRF. The shaded areas correspond to trough floors (areas of relatively high intensity acoustic backscattering). The maximum depth is 21.4 m and the minimum depth is 16.7 m. The area depicted corresponds to the dotted outline in the top panel.



The spatial distribution of small-scale bedforms on the inner shelf is correlated with the primary relief of the ridges (Green, 1986; Swift and Field, 1981). Green (1986) described megaripples (wavelength 3 to 9 m; height 0.5 to 1 m) which are restricted to the coarse sands of the ridge crests, and wave ripples (wavelength 10 to 25 cm; height 1 to 4 cm) which are ubiquitous. Unlike the inner shelf, the shoreface is devoid of bedforms of a scale larger than wave ripples. Acoustic imagery acquired during the shore-normal traverse in July, 1984, is shown in Figure 3.3. From the shoreward end of the traverse (upper shoreface; 8-m depth) to the break in slope at the base of the shoreface (22-m depth), the shoreface appears bland and homogenous (cf. Figures 2 and 4 of Green, 1986); diver observations however revealed the ubiquitous occurrence of wave ripples. Grid surveys of the upper and middle shoreface undertaken in July, 1984, (see Figure 3.1) and subsequent surveys in October, 1984, and July, 1985, support the contention that the shoreface is uniformly bland at scales larger than that of wave ripples. Wave ripples, as reported by divers during the July, 1984, survey, were symmetrical with rounded crests and flattened troughs. Ripple length was 10 to 15 cm and height 1 to 3 cm. Crest lengths were continuous over horizontal distances of several meters and typically ended in tuning-fork patterns. The crests were aligned parallel to shore, which was approximately normal to the direction of wave propagation at the time. Both Birkemeier et al. (1985) and Williams (1983) observed similar features; Birkemeier et al. also observed megaripples (wavelength 2 m; height 15 cm) in 2.9-m water depth immediately seaward of the surfzone.

Like that of small-scale bedforms, the spatial distribution of

Figure 3.3 Acoustic imagery of the shoreface. The swath is continuous; read the figure from the lower left (8-m depth) across each line always to the right. The break in imagery on the top line corresponds to the base of the inner shelf (22-m depth, ~5-km offshore).



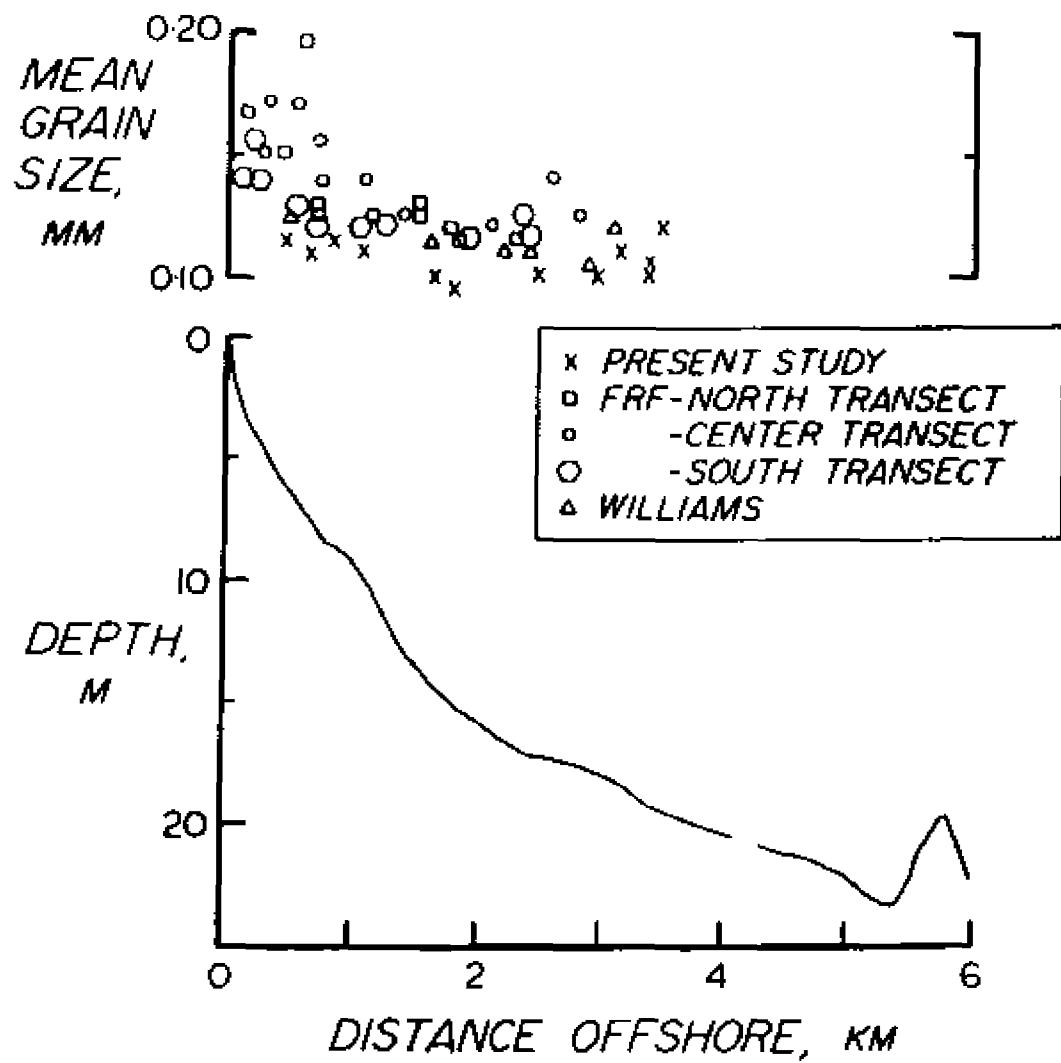
inner-shelf sediments is tied to the primary relief of the sand ridges (e.g. Stubblefield and Swift, 1981). The surficial sediments of the shoreface display no such order. Birkemeier et al. (1985) reported on 35 short-core sediment samples collected along three shore-normal transects, one transect extending seawards from the end of the FRF pier, and the other two lying 75 m north and south of that line. Sediments were generally moderately well-sorted, medium to fine quartz sands, with median grain-size ranging from 0.29 mm to 0.12 mm. Two sandy silt samples were obtained between 13 and 15-m depth; this location coincides with a fine-grained backbarrier outcrop described by Field et al. (1979). Although subaerial beach and surfzone sediments frequently contain a significant coarse fraction (Swift et al., 1971), Birkemeier et al.'s samples contained no gravel except for one secondary mode in one sample directly seaward of the FRF pier-end (7-m depth).

Surficial sediment samples were obtained along a transect extending seawards from the end of the FRF pier by personnel operating a grab-sampler from a vessel, and by divers operating a short coring device. Samples were collected during the July, 1984, and October, 1984, surveys. Samples were split into gravel, sand, silt and clay fractions, and analysed using a rapid sediment analyser. Mean, median and standard deviation were calculated from the particle size distribution using Folk's (1980) graphic technique. These parameters are reported in Table 3.1, and the mean grain-size is plotted in Figure 3.4 as a function of distance offshore together with Williams' (1983) data, collected along the same transect, and Birkemeier et al.'s data. Typically, the silt and clay fraction makes up less than 8% by weight of the total sample and is bound in sand-sized fecal pellets. Seaward of approximately

Table 3.1 Gravel, sand, silt, clay ratios; median grain-size; graphic mean grain-size; and graphic standard deviation of shoreface sediment samples collected along a shore-normal transect seaward of the FRF pier during July, 1984, and October, 1984.

DEPTH	GRAV/SAND/SILT/CLAY	MEDIAN	MEAN	GRAPHIC
(m)		GRAIN	GRAIN	STANDARD
		SIZE	SIZE	DEVIATION
		(mm)	(mm)	(ϕ units)
6	0.0/96.9/ 3.1/ 0.0	0.13	0.13	0.26
7	0.7/92.8/ 6.5/ 0.0	0.13	0.12	0.22
8	0.0/94.9/ 5.1/ 0.0	0.13	0.13	0.29
8	0.9/94.5/ 4.6/ 0.0	0.13	0.13	0.28
9.5	0.9/93.5/ 2.1/ 3.4	0.12	0.12	0.28
12	0.2/86.5/ 8.5/ 4.9	0.09	0.09	0.48
12	0.0/89.7/ 5.3/ 5.0	0.10	0.10	0.33
15	0.0/78.0/19.0/ 3.1	0.10	0.10	0.34
17.5	0.0/91.6/ 8.4/ 0.0	0.12	0.12	0.30
17.5	0.0/88.8/ 6.3/ 4.9	0.11	0.10	0.36
18	4.7/89.0/ 2.2/ 4.2	0.11	0.11	0.34
18	0.0/89.9/ 6.6/ 3.4	0.10	0.10	0.30
18.5	0.0/94.5/ 5.6/ 0.0	0.13	0.14	0.61

Figure 3.4 Mean grain-size as a function of depth and distance offshore as reported in: the present study; Birkemeier et al. (1985) (FRF transects in the figure); and Williams (1983).



7.5-m depth, mean grain-size ranges from 0.09 mm (where backbarrier fines are exhumed) to 0.14 mm. No clear trend of grain-size with depth is evident either from any individual's data or from all the data combined. Shoreward of 7.5-m depth, surficial sediments appear to become coarser as depth decreases. The maximum reported grain-size is 0.29 mm from approximately 4-m depth.

The surficial geology of the shoreface and inner shelf in the vicinity of Duck differ in type (primary relief, characteristic bedforms and sediments) and in scales and types of within-region variability. germane to the numerical simulations that follow in Chapter 4 is the conclusion that the surficial shoreface geology varies primarily with distance offshore. Thus the shoreface can be adequately described using two dimensions only, i.e. by ignoring the alongshore dimension. The comparison between the shoreface and inner shelf serves to illustrate and emphasize this point. Whereas the primary relief of the inner shelf (i.e. that associated with the sand ridges) varies as a complex function of both horizontal dimensions, the concave bow of the shoreface is uniform across large separations in the alongshore dimension. Also, the distribution of sediments and bedforms on the inner shelf is tied to primary relief of the sand ridges; in contrast, characteristic sediments and bedforms (wave ripples) of the shoreface display no significant trends with either depth or distance alongshore.

3.2.2 Physical oceanography

Records of waves, tides, currents and winds have been maintained at the FRF since 1980. Data have been reported in preliminary form in monthly reports (Coastal Engineering Research Center [CERC], 1980 to present), in comprehensive form in annual reports, and as an overview of the area in a user's guide to the FRF (Birkemeier et al., 1985).

The annual average significant wave height at the seaward end of the FRF pier (7-m depth) is 0.9 ± 0.6 m and the annual average peak spectral period is 8.7 ± 2.8 s. Waves are lowest from April to September, and highest from October to December. Higher waves accompany storms; the region is affected by both extratropical ("northeaster") and tropical (hurricane) cyclones. High waves associated with storms are most likely to occur from October to March. Storm breaker-wave heights may exceed 4 m and persist for hours to days. Waves approach mainly from the south in the spring and summer, driven before the predominant southwest to southeast winds. Winter waves originate typically from the northern quadrant. Extreme waves usually approach from the northeast.

The coastal tides are semi-diurnal with a mean range of 1 m and a mean spring range of 1.2 m. Seaward of the surfzone, the tip of the tidal current vector traces out an ellipse that is elongated in the shore-parallel dimension (Battisti and Clarke, 1982). Redfield (1958) showed that the shelf tide co-oscillates with a driving oceanic tide that impinges on the shelf slope. The passage of the tidal wave across the shelf is delayed by bed friction; close to shore (within 20-m depth), enhanced friction causes tidal currents to diminish rapidly (Niedoroda et al., 1985).

Beardsley et al. (1976) showed that most of the subtidal (i.e. of a frequency less than tidal) current variability over the shallow shelf of the Mid-Atlantic Bight is wind-driven. Fifty percent of the subtidal current variance is in a wide band ("synoptic" band) of 0.01 to 1.0 cycles per day. In this band, the local cross-shelf component of wind is unimportant except near the coast where it can generate trapped pressure fields that drive alongshore currents; for example, Wright et al. (1986) observed a strong (33 cm/s at 20 cm above the bed) south-setting (shore-parallel) current in 8-m water depth off the FRF associated with northeast winds and a local setup in the mean water-level of 60 cm. In contrast, local longshore wind stress is coherent with the longshore current and sea-level over the entire shelf (e.g. Huyer et al., 1975; Scott and Csanady, 1976). The water column response is typically barotropic and lags the imposed wind stress by a time on the order of one inertial period (Winant, 1979). The principal synoptic scale forcing is the travelling winter mid-latitude cyclone that originates near Cape Hatteras and intensifies as it propagates towards the northeast (Beardsley and Boicourt, 1981). Beardsley and Butman (1974) described strong longshore currents (20 to 50 cm/s) in the mid-shelf region that were generated by winter storms. Boicourt and Hacker (1976) described southward storm flow (30 to 50 cm/s at mid-depth) off the Virginia coast.

Monthly mean currents are generally directed downshelf (i.e. to the south) at all elevations, with a few exceptions; for example, Beardsley and Boicourt (1981) described strong upshelf flow that occurred for periods of 1 to 6 weeks. Winant (1979) identified three types of

forcing at this scale: direct wind stress, adjoining deep-ocean motions, and river runoff.

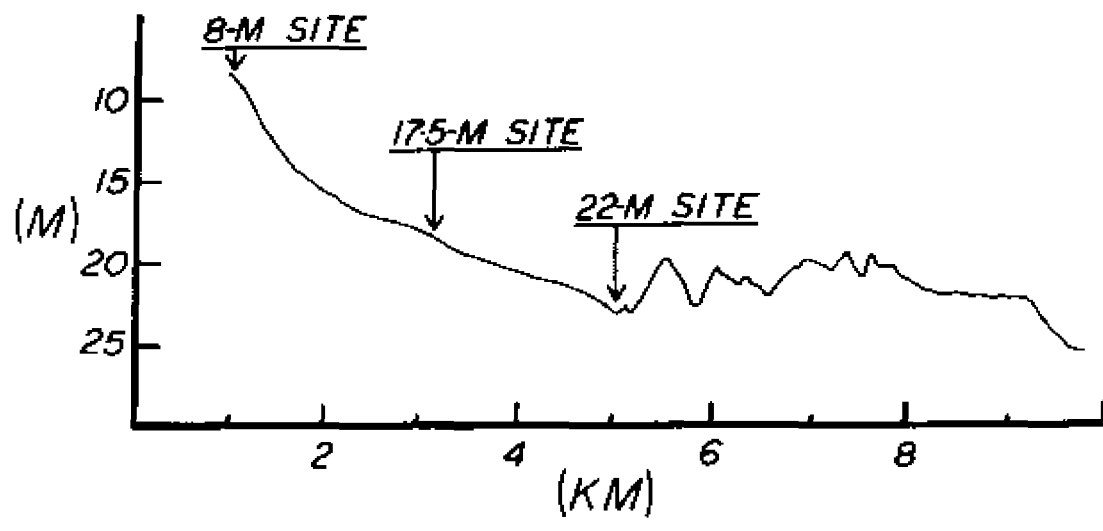
An annual mean southwestward drift throughout the Mid-Atlantic Bight has long been known (e.g. Bumpus, 1965). In the vicinity of Cape Hatteras, shelf water turns seaward and is entrained into the Gulf Stream. Superimposed on the mean drift is a series of distinct eddies. The seabed drifter studies of Bumpus (1965) also demonstrated bottom drift from shoreward of 60 to 80-m depth toward the mouths of major estuaries.

3.3 Experiment Description and Data Analysis

A right-handed co-ordinate system is used throughout the following analysis, with the positive y-axis aligned shore-parallel to the north, and the positive x-axis aligned shore-normal to the east. The shore is rotated 20° to the west of north (i.e. the shore trends 340° - 160°). The shoreline is defined as the origin.

Three experiments were conducted seaward of the FRF: on the upper shoreface in 8-m water depth, on the mid-shoreface in 17.5-m water depth, and on the lower shoreface near the edge of the inner shelf in 22-m water depth (Figure 3.5). Discussion of data from the upper-shoreface deployment will be postponed until Chapter 4, when bed response to fairweather waves and currents is discussed.

Figure 3.5 Locations of current-meter deployments. Current meters were deployed at three locations on the shoreface seaward of the FRF at Duck.



3.3.1 Mid-shoreface experiment

The mid-shoreface experiment (17.5-m water depth; 36° 10.65' N, 75° 42.77' W) was conducted over the period 16-18 August, 1983. The data set comprises high-frequency measurements of near-bed currents and periodic visual observations of the seabed in the immediate vicinity of the current meters. Over the duration of the experiment, waves were low, winds light, and steady currents weak relative to reported storm currents (e.g. Wright et al., 1986; Ludwick, 1978).

Surficial sediment samples were collected by divers in the immediate vicinity of the current-meter installation. Sediment was devoid of gravel and contained less than 8% of silt plus clay by weight. The sand fraction was composed of noncohesive quartz particles; mean grain-size was 0.10 mm and graphic standard deviation was 0.30 phi units, which, according to Folk's (1980) scheme, indicates a very well sorted sediment.

Periodic observations of small-scale seabed morphology in the immediate vicinity (20-m radius) of the current meters were also made by divers. The principal features were low, long-crested, rounded wave ripples. The average ripple height was 2 cm and the average spacing between ripples was 10 cm. Ripple crests were oriented approximately parallel to shore, which was normal to the direction of wave approach at the time. The wave ripples persisted over the duration of the experiment. Biogenic roughness was negligible; scattered worm tubes that protruded less than 3 mm above the bed surface were the primary biogenic structures.

Two Marsh-McBirney Model MM551M current meters (4.0-cm diameter sphere) arranged in a vertical profile were used to measure currents. The instruments were attached to a single mounting pipe and the pipe was suspended from the center of a weighted frame that was placed on the seabed. The current meters were located at 20 and 65 cm above the bed. The legs of the frame were 4.0-cm diameter; no part of the frame was within 1.5 m of the instruments in any horizontal direction.

Data were transmitted over armoured cables to an anchored vessel where a computer controlled a burst-sampling sequence. The analog (voltage) current-meter output was read and digitized by the computer, and the digital representation was written to cassette tape for later analysis.

In general, the choice of sampling interval, Δt , is constrained by the data-logger's capability and by the characteristics of the random process that is being measured. The sampling interval must be short enough such that the Nyquist frequency ($= 1/2\Delta t$) is greater than the highest-frequency signal that is likely to be present at significant energy levels. The Nyquist frequency is the highest frequency about which information can be obtained in a time-series analysis; furthermore, in a spectral analysis, energy at frequencies higher than the Nyquist frequency is folded back into lower frequencies ("aliasing") thus rendering the spectrum useless if the folded energy is high. Surface gravity-waves, considered a priori to be the highest-frequency energy source of significant magnitude on the shoreface, range in period from 4 to 16 s. A sampling interval of 1 s was chosen as the best compromise between the competing needs of the analysis and the data

logger; tests indicated that sampling faster than 1 Hz could lead to an overload of the computer.

The burst duration must be long enough to ensure that: (1) the high-frequency turbulence is sufficiently averaged; (2) enough wave cycles are measured to provide stable estimates of average wave parameters; and (3) the resolution of the spectrum, after smoothing, is acceptable. The burst duration must also be short enough to ensure that: (4) low-frequency signals (tidal currents) appear steady over the burst; and (5) the data-logger capacity is not exceeded. If the burst duration is long enough to satisfy (2) then (1) should be automatically satisfied. Lesht (1980) proposed that the averaging period be at least 20 times the characteristic time-scale of the flow. For surface gravity-waves this time-scale is the wave period and therefore the recommended averaging period is 80 to 320 s. If energy is present at beat frequencies, then a longer averaging period is required. After weighing the competing requirements, a burst duration of 240 s was chosen.

The burst interval is the time between the beginning of successive bursts; the burst interval must exceed the burst duration in order to provide the computer with time to write accumulated data to tape. A burst interval of 360 s was chosen to minimize down-time of the system.

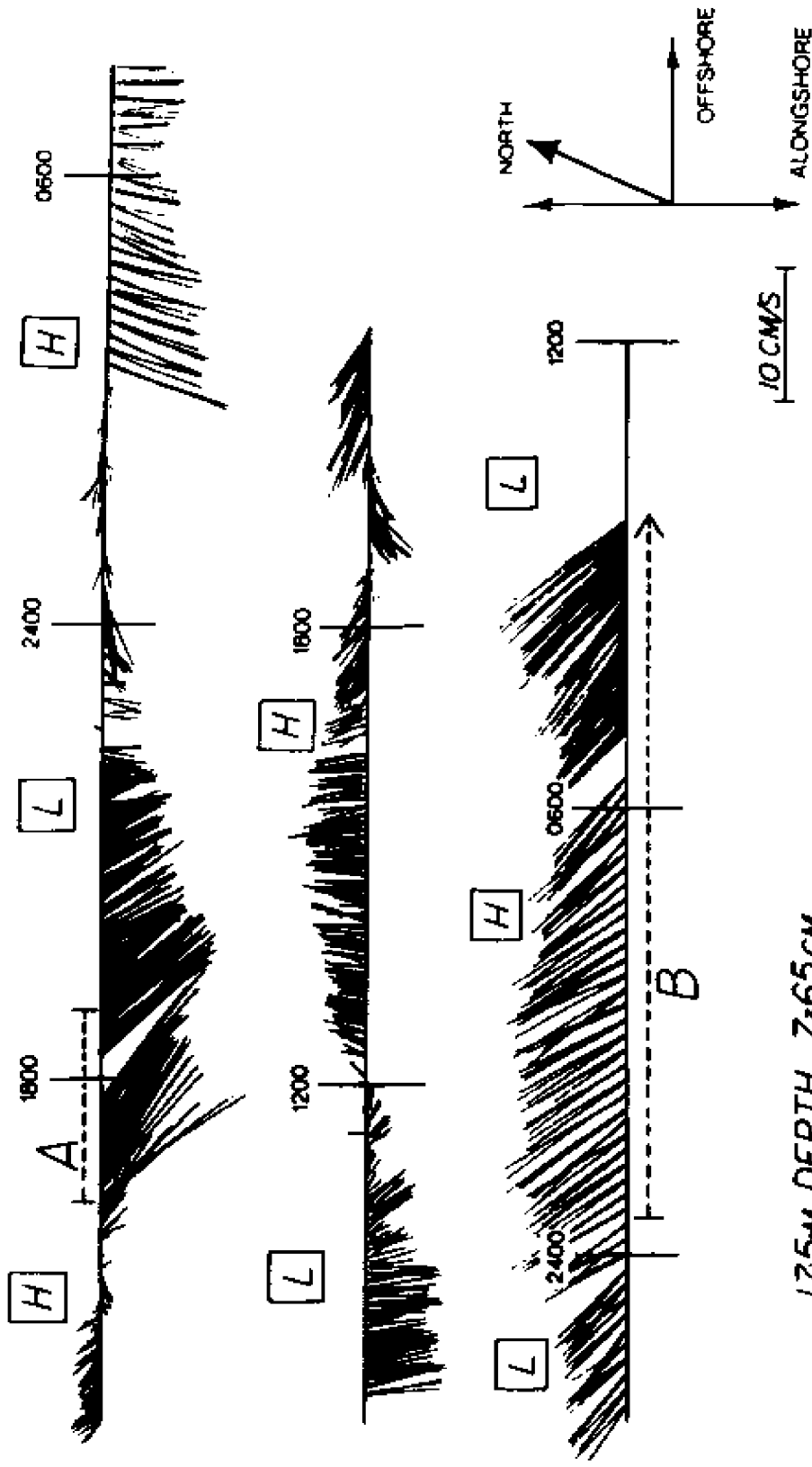
The bursting sequence was interrupted when the cassette tape was changed. Nine gaps, each of 10-minutes duration typically, occurred during the mid-shoreface deployment. Throughout the experiment, divers periodically verified the elevation and orientation of the current meters.

The lower current meter ($z = 20$ cm) failed early in the experiment. The digitized output voltage of the upper current meter ($z = 65$ cm) was converted into estimates of component speeds using a calibration curve that was derived from a steady-flow laboratory calibration (see section 3.4.3). The vector-averaged current velocity over the duration of the experiment is shown in Figure 3.6. On this and other plots, events, or periods when the threshold shear stress was exceeded, are indicated; events are discussed in Chapter 4. Also shown in Figure 3.6 are predicted times of high and low water at Kitty Hawk (20 km to the south of Duck) from the National Ocean Service tide tables.

Shown in Figure 3.7 are time series of the burst-averaged flow parameters ($z = 65$ cm) that are required for the prediction of the bed shear stress using the combined-flow boundary-layer model. The maximum near-bed wave-orbital velocity, $U_{w,m}$, is represented by $U_{1/10}$, which is the average of the highest 10% of the measured current speeds with the mean current removed. One estimate of $U_{1/10}$ was calculated for each burst. The steady-current speed, U_c , is represented by the magnitude of the vector-averaged (over the duration of the burst) current velocity. To facilitate comparisons among experiments, the measured mean speed was adjusted to apply to $z = 100$ cm (U_{100}) using the solution for the mean-current profile above the wave boundary layer (equation 2.24).

Current direction is represented by the direction of the vector-averaged (over the duration of the burst) current velocity. Direction of wave propagation was calculated as follows. The right-handed horizontal co-ordinate system was rotated anti-clockwise 180° in 5° increments from its original orientation and for each increment the variance of the shore-parallel component of the current velocity was

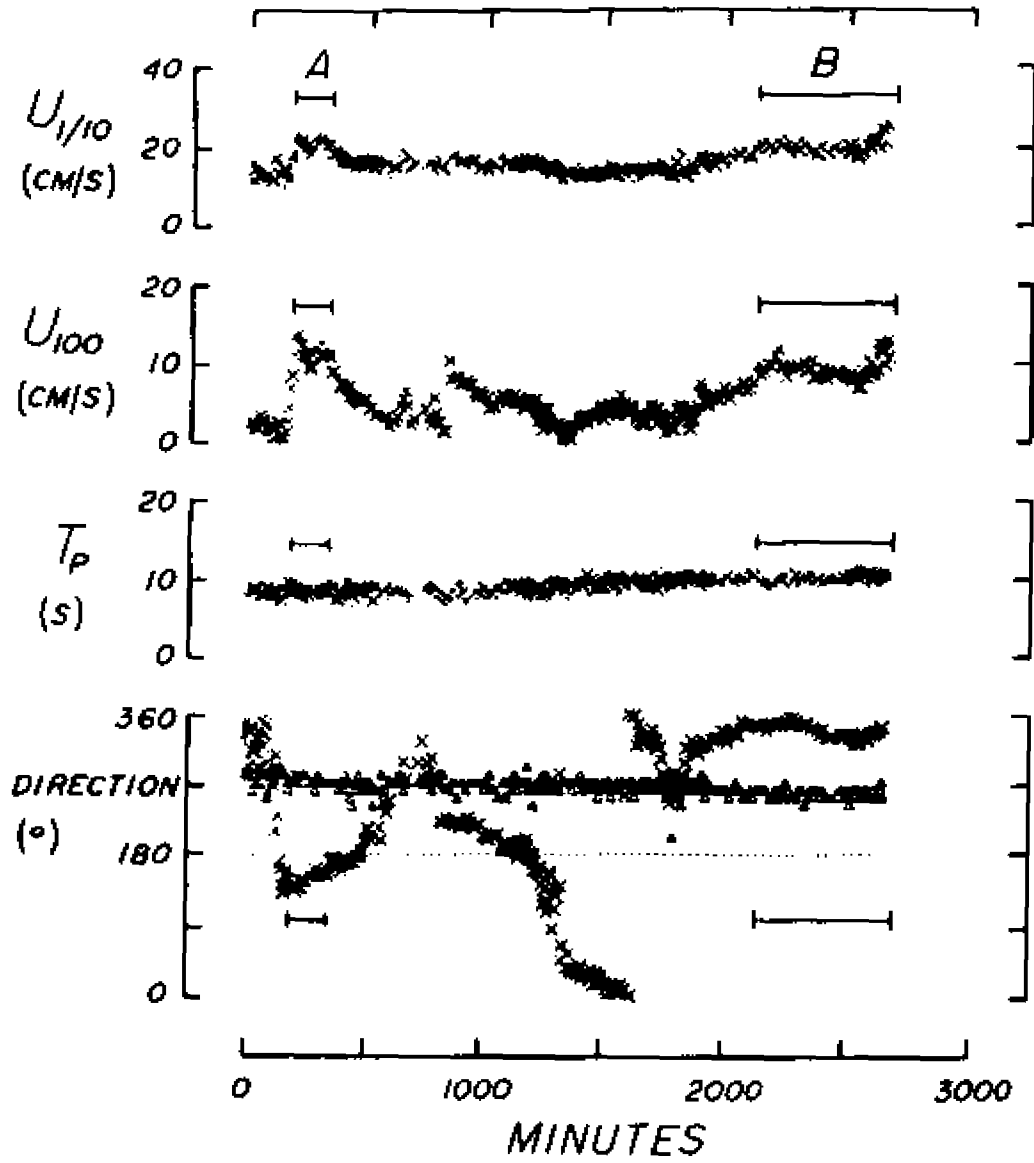
Figure 3.6 Overview of mid-shoreface (17.5-m depth) experiment. Shown are the vector-averaged (over blocks of 80 s) current velocities ($z = 65$ cm) and times of predicted high ("H") and low ("L") water 20 km to the south at Kitty Hawk. Two events, A and B, are indicated.



175-M DEPTH, Z=65 CM

Figure 3.7 Mid-shoreface (17.5-m depth) experiment. Burat-averaged estimates of $U_{1/10}$, U_{100} , T_p , wave direction (Δ) and current direction (x). 180° is parallel to shore to the south, 90° is normal to shore to the east, and so on. Directions are directions setting (propagating) to. Two events, A and B, are indicated.

MID-SHOREFACE



calculated. The direction of wave propagation was defined as the rotation angle that maximized the variance of the shore-parallel velocity component.

Wave period, T , is represented by the peak spectral period, T_p (i.e. period of maximum energy-density), which was identified from the power spectrum of the zero-mean shore-normal component of the velocity series. The co-ordinate system was rotated such that the variance of the shore-normal velocity component was maximized, and the spectrum was then computed using a Fast Fourier Transform. The spectrum was smoothed by averaging across blocks of four adjacent frequencies. Spectral analysis was performed on each burst; one spectrum that is representative of the experiment is shown in Figure 3.8. The peak is relatively narrow and centered on about 8 s, which validates the choice of burst duration (since there are 30 cycles of an 8-s wave in 240 s). Also, there is no unresolved energy at the red (low-frequency) end of the spectrum, indicating that the time series is indeed stationary.

Shown in Figure 3.9 are calculated estimates of "burst-averaged" dynamic, transport and related parameters. It is emphasized that these are not strictly burst-averages since they are not obtained by time-integrating instantaneous values; rather, each "burst-averaged" parameter is calculated by applying the combined-flow boundary-layer and transport theories to the burst-averaged flow parameters. Skin frictions were calculated as though the bed were flat (section 2.5): observed velocities were used directly in the boundary-layer model (i.e. they were not related to velocities within the internal boundary layer), and the grain roughness was used to calculate z_0 (equation 2.41). Equation 2.45 was used to calculate k_G , with $C_2 = 2.5$ and $n = 50$, where

Figure 3.8 Power spectrum of one burst sample of the zero-mean rotated shore-normal component of velocity, 17.5-m water depth. The spectrum was calculated from 240 points ($\Delta t = 1$ s) and was smoothed by averaging across blocks of four adjacent spectral estimates. The 95% confidence interval is indicated.

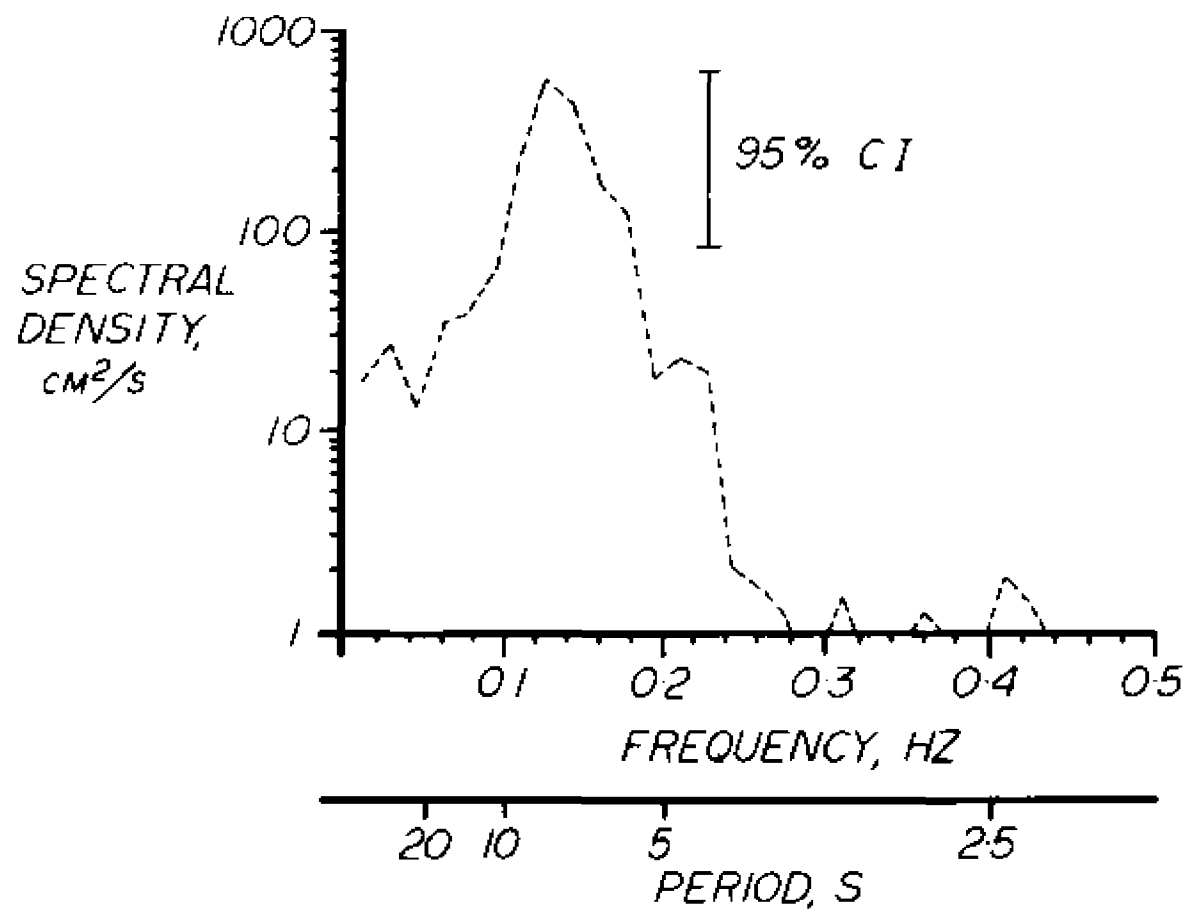
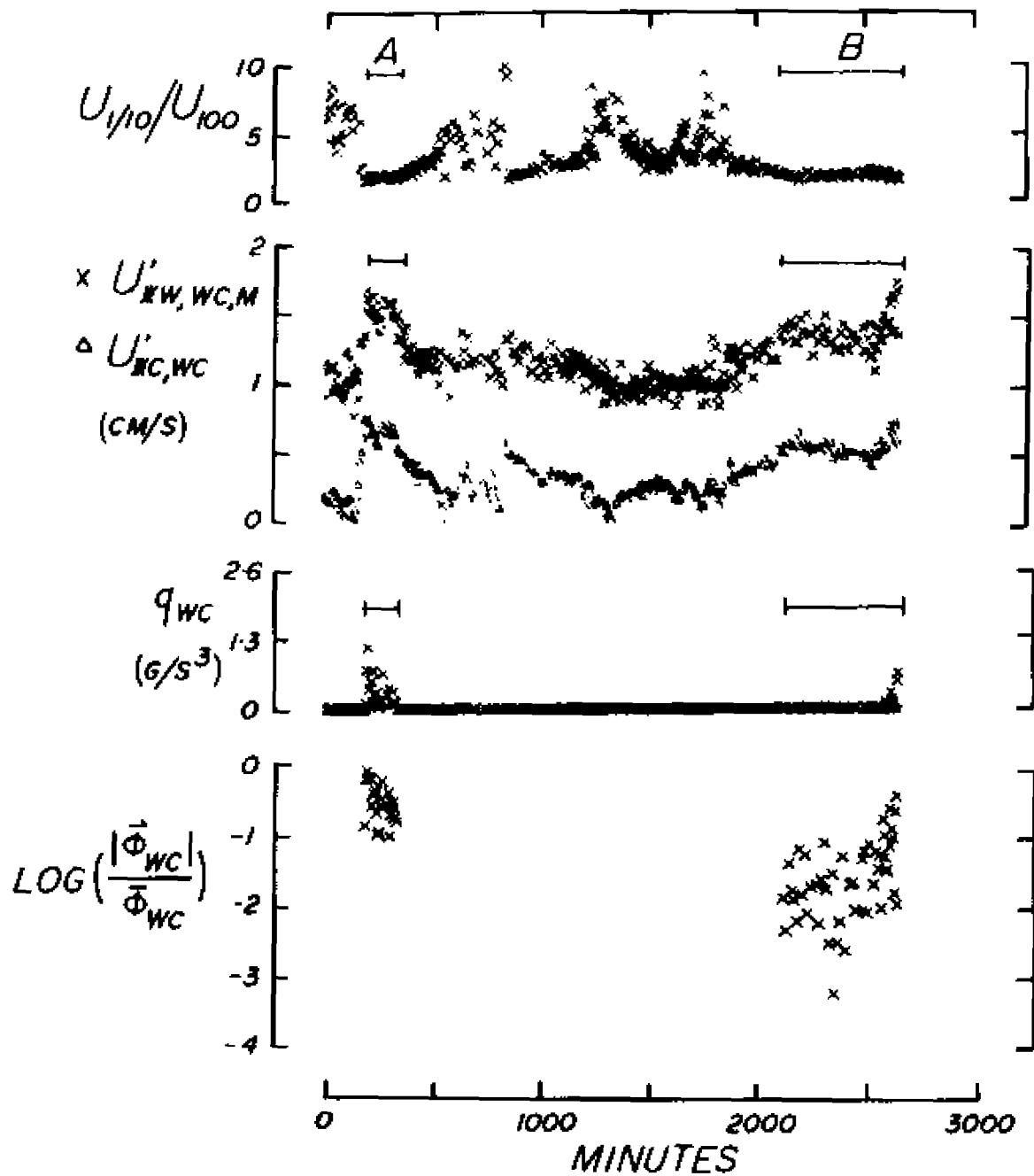


Figure 3.9 "Burst-averaged" (refer to the caveat in the text) dynamic, transport and associated parameters; mid-shoreface (17.5-m depth) experiment. Two events, A and B, are indicated.

MID-SHOREFACE



$D_{50} = 0.10 \text{ mm.}$

Net bedload transport over the wave period, $\hat{\phi}_{WC}$, was calculated according to equations 2.38 and 2.39 with $\psi_{CR} = 0.10$, which is applicable to 0.10-mm noncohesive quartz sand under waves (Madsen and Grant, 1976). $\hat{\phi}_{WC}$ was converted to units of weight per unit width (\hat{q}_{WC}) by multiplying by $\rho_s g w D$, where $\rho_s = 2.65 \text{ g/cm}^3$, $g = 981 \text{ cm/s}^2$ and $w = 1 \text{ cm/s}$. Average bedload transport over the half-wave period, $\bar{\phi}_{WC}$, was calculated to provide a perspective on the magnitude of $\hat{\phi}_{WC}$. If the ratio $|\hat{\phi}_{WC}|/\bar{\phi}_{WC}$ is small, then net transport is due to only a relatively small asymmetry in the back and forth movement of sediment. If such were the case, small errors in predictions would be more likely to lead to major errors in inference.

3.3.2 Lower-shoreface experiment

The site of the second experiment was 22-m water depth ($36^\circ 11.10' \text{ N}$; $75^\circ 40.86' \text{ W}$) on the shoreward flank of the first sand ridge at the base of the shoreface (Figure 3.5). Near-bed currents were measured and the seabed observed by divers over the period 20 to 23 July, 1984. Low-energy (fairweather) conditions persisted over the duration of the experiment.

Surficial sediment at the site was a very well-sorted, fine-grained, noncohesive quartz sand that contained less than 5% gravel and less than 3% silt plus clay by weight. Mean grain-size was 0.20 mm.

Short-crested, symmetrical wave ripples constituted the primary seabed roughness (Figure 3.10). Ripple crests were less than 1.5-m long and joined in tuning-fork patterns. Ripple wavelengths varied from 15

Figure 3.10 Primary physical roughness at the 22-m depth site: short-crested, rounded, symmetrical wave ripples. Each band on the scale is one centimeter.



to 25 cm, and height from 2 to 5 cm. Mobile benthic organisms, including Polinices sp. (moon snail), Pagurus sp. (hermit crab) and Busycon sp. (whelk), constituted the primary biogenic roughness; the seabed itself showed no evidence of reworking by biota.

Currents were measured at elevations of 20 and 70 cm above the bed using the data-logging system previously described. Currents were sampled in a burst mode; the sampling interval was 1 s, burst duration 1800 s, and burst interval 3600 s. Currents were logged over 62.5 hours with only two breaks of 1-hour duration in the bursting sequence. The lower current meter again failed early in the experiment. Divers periodically checked the current-meter orientation and elevation and recorded observations of the bed.

The vector-averaged current velocity ($z = 70$ cm) and predicted times of high and low water for Kitty Hawk are shown in Figure 3.11. The burst-averaged flow parameters are shown in Figure 3.12; the "burst-averaged" dynamic, transport and related parameters in Figure 3.13. The calculations proceeded as previously described, with one exception: flow parameters were averaged over adjacent blocks of 600 s (three blocks per burst), therefore there are three estimates of each parameter per burst. For the purposes of the transport calculations, ψ_{cr} was set at 0.060, which is applicable to 0.20-mm noncohesive quartz sand under waves (Madsen and Grant, 1976).

Figure 3.11 Overview of lower-shoreface (22-m depth) experiment. Shown are the vector-averaged (over blocks of 60 s) current velocities ($z = 70$ cm) and times of predicted high ("H") and low ("L") water. Two events, C and D, are indicated.

22-M DEPTH, Z = 70CM

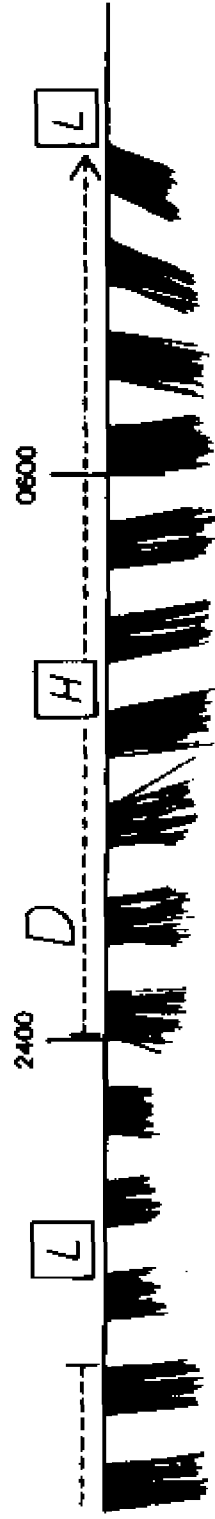
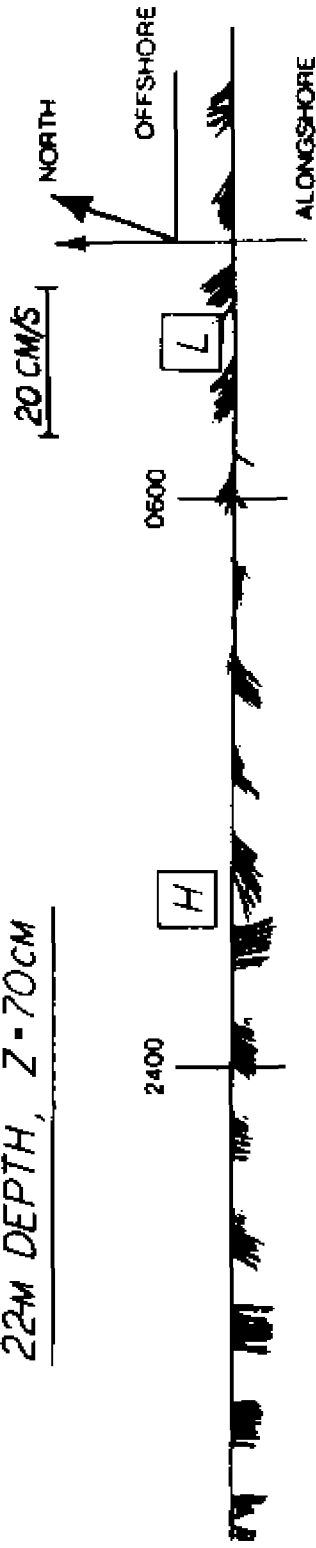


Figure 3.12 Lower-shoreface (22-m depth) experiment. Burst-averaged estimates of $U_{1/10}$, U_{100} , T_p , wave direction (Δ) and current direction (\times). 180° is parallel to shore to the south, 90° is normal to shore to the east, and so on. Directions are directions setting (propagating) to. Two events, C and D, are indicated.

LOWER SHOREFACE

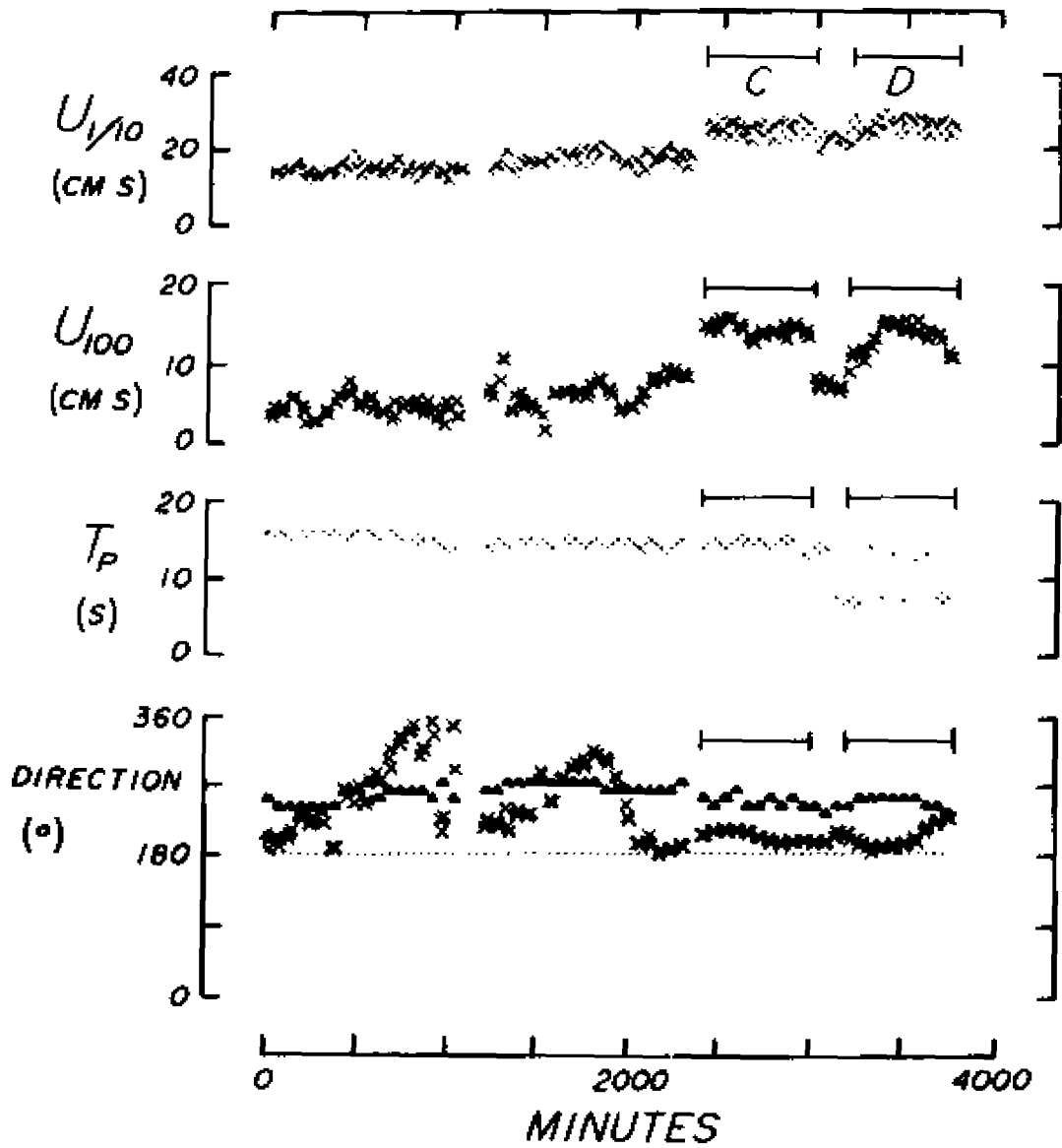
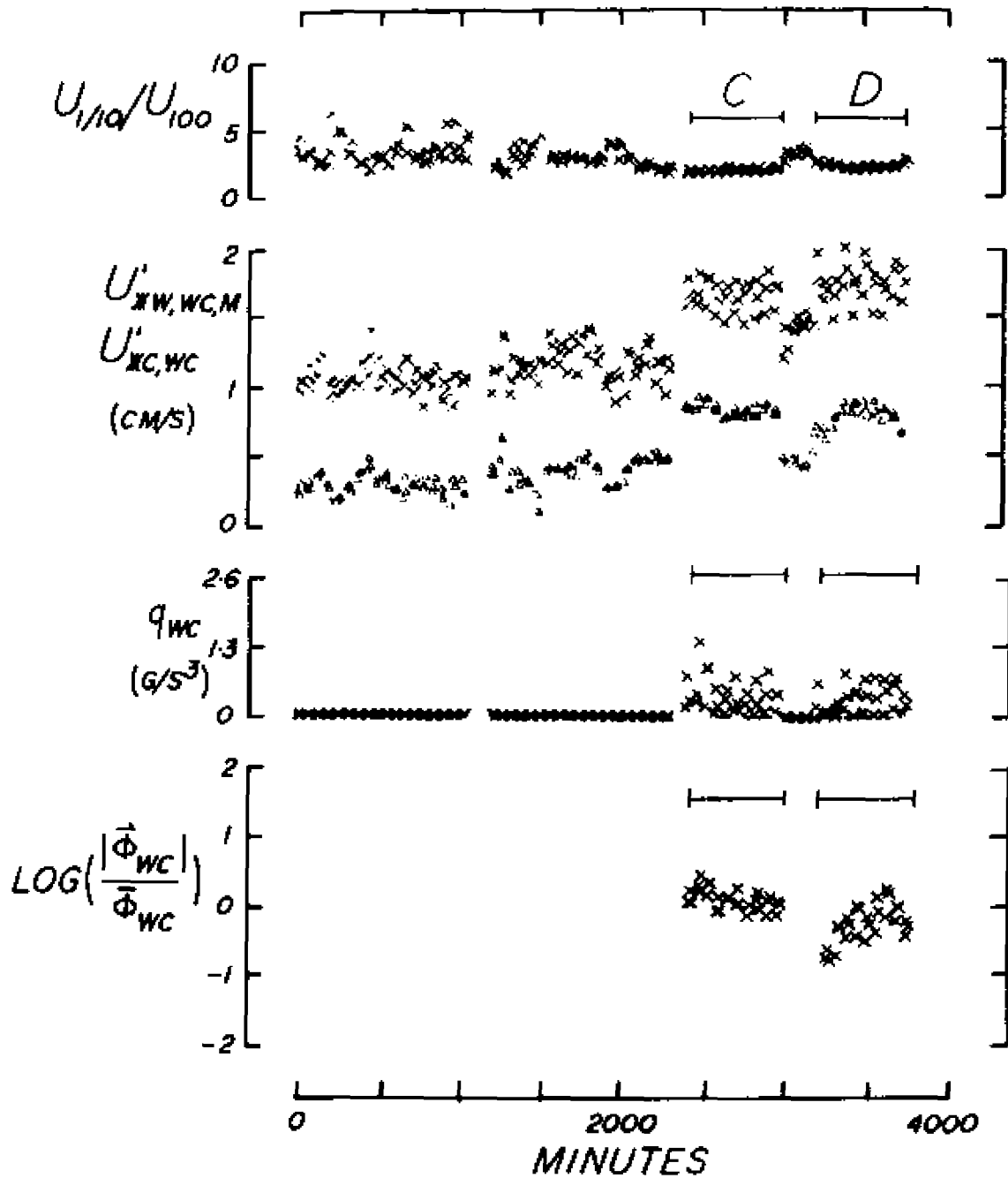


Figure 3.13 "Burst-averaged" (refer to the caveat in the text) dynamic, transport and associated parameters; lower-shoreface (22-m depth) experiment. Two events, C and D, are indicated.

LOWER SHOREFACE



3.4 Evaluation of Dynamic and Flux Estimates

A full evaluation of the model calculations should include both verification with controlled experimental data and an error analysis. For a detailed error analysis, the statistical distribution of each model parameter must be known. As an alternative to the error analysis, the sensitivity of the calculations to variability in each of the model parameters may be demonstrated and used to evaluate the predictions. For complicated calculations, or when the model parameters are not fully understood, the latter approach (i.e. sensitivity analysis) is preferable.

3.4.1 Dynamic calculations

One component of the Coastal Ocean Dynamics Experiment (CODE) was designed to identify key physical processes controlling bed shear stress on an open ocean shelf. Grant et al. (1983) and later Grant et al. (1984) reported on a low-energy subset of the CODE data, the "CODE-1 subset", with the objective of verifying the predictive capability of Grant and Madsen's (1979) combined flow boundary layer model. The analysis provided "a quantitative and unambiguous comparison of the near bed flow and stress models with high quality data sets" (Grant et al., 1983, p. 5). The same data are used in this section to verify the combined-flow stress model of Larsen et al. (1981).

The CODE-1 data set comprised four days of velocity-profile and ancillary measurements obtained during low-energy conditions on the northern California shelf in 100-m water depth. Current velocity was

measured at four elevations above the bed (nominally 30, 55, 105 and 205 cm) by vertically-stacked acoustic current meters. The sampling rate was 5 Hz. Measured velocities were averaged over blocks of 9.33 minutes and the equation for the steady-flow law of the wall (e.g. Dyer, 1986):

$$U_c(z) = (U_{*c}/\kappa) \ln(z/z_0) \quad (3.1)$$

was fitted to each velocity profile, where U_{*c} is the current friction velocity. U_{*c} was obtained from the slope of the fitted equation, and z_0 from the intercept. Only those profiles with a high correlation coefficient and no significant curvature were used in the analysis. As an independent check on the validity of applying the velocity-profile method, bottom stress and stress at the upper three levels in the flow were computed using an inertial-dissipation technique (Grant et al., 1983). The two methods provided estimates of stress which were in good agreement.

Observed values of U_{*c} and z_0 were large relative to those expected for uniform steady flow. Anomalously high values of U_{*c} and z_0 were consistent with the following hypothesis: the observed stress and roughness were enhanced by a nonlinear interaction characteristic of a combined-flow boundary layer. In this case, the observed U_{*c} corresponds to $U_{*c,wc}$ of the combined-flow model, and the observed z_0 corresponds to z_1 (equation 2.24). That the velocity measurements were made in the potential-flow region of the wave (i.e. $z > \delta_w$) is easily demonstrated; δ_w (equation 2.25) for typical surface gravity-waves is on the order of several centimeters while the lowest current meter was 30 cm above the bed.

Grant et al. (1983) tested the ability of Grant and Madsen's (1979) combined-flow model to reproduce the CODE-1 observations. Grant et al. reported estimates of $U_{w,m}$, ω , θ and k . Maximum wave-orbital velocity was based on the maximum amplitude of the wave envelope and ω was represented by the average wave frequency. Direction of wave propagation was inferred from the ratio of the orthogonal components of the wave-orbital velocity. Boundary roughness was estimated from observations of the bed; since no sediment was in motion, the roughness reflected only the physical characteristics (primarily animal mounds) of the seafloor.

Plotted in Figures 3.14 and 3.15 are: $U_{*c,wc}$ and z_1 calculated by Grant et al. (1983) using the method of Grant and Madsen (1979) with the parameters reported by Grant et al. (1983); $U_{*c,wc}$ and z_1 calculated using the method of Larsen et al. (1981) with the same parameters; and the observed values of $U_{*c,wc}$ and z_1 . Grant et al. (1983) concluded that the agreement between observed and calculated values verified Grant and Madsen's (1979) combined-flow model; Larsen et al.'s (1981) combined-flow theory provides predictions that are in similar good agreement with observations.

Either combined-flow dynamics model can thus be used with confidence to predict bed shear stress provided the near-bed logarithmic velocity profile is linear. Clearly, this provision cannot be tested when velocity is measured at only one elevation above the bed, and must be left as an a priori assumption in the model application.

Figure 3.14 Comparison of: $U_{*c,wc}$ calculated by Grant et al. (1983) using the method of Grant and Madsen (1979) with the CODE-1 parameters reported by Grant et al. (1983); $U_{*c,wc}$ calculated using the method of Larsen et al. (1981) with the same parameters; and the CODE-1 observations reported by Grant et al. (1983). The vertical lines represent the computed error range of the observed stress. The best estimate is the midpoint of the range.

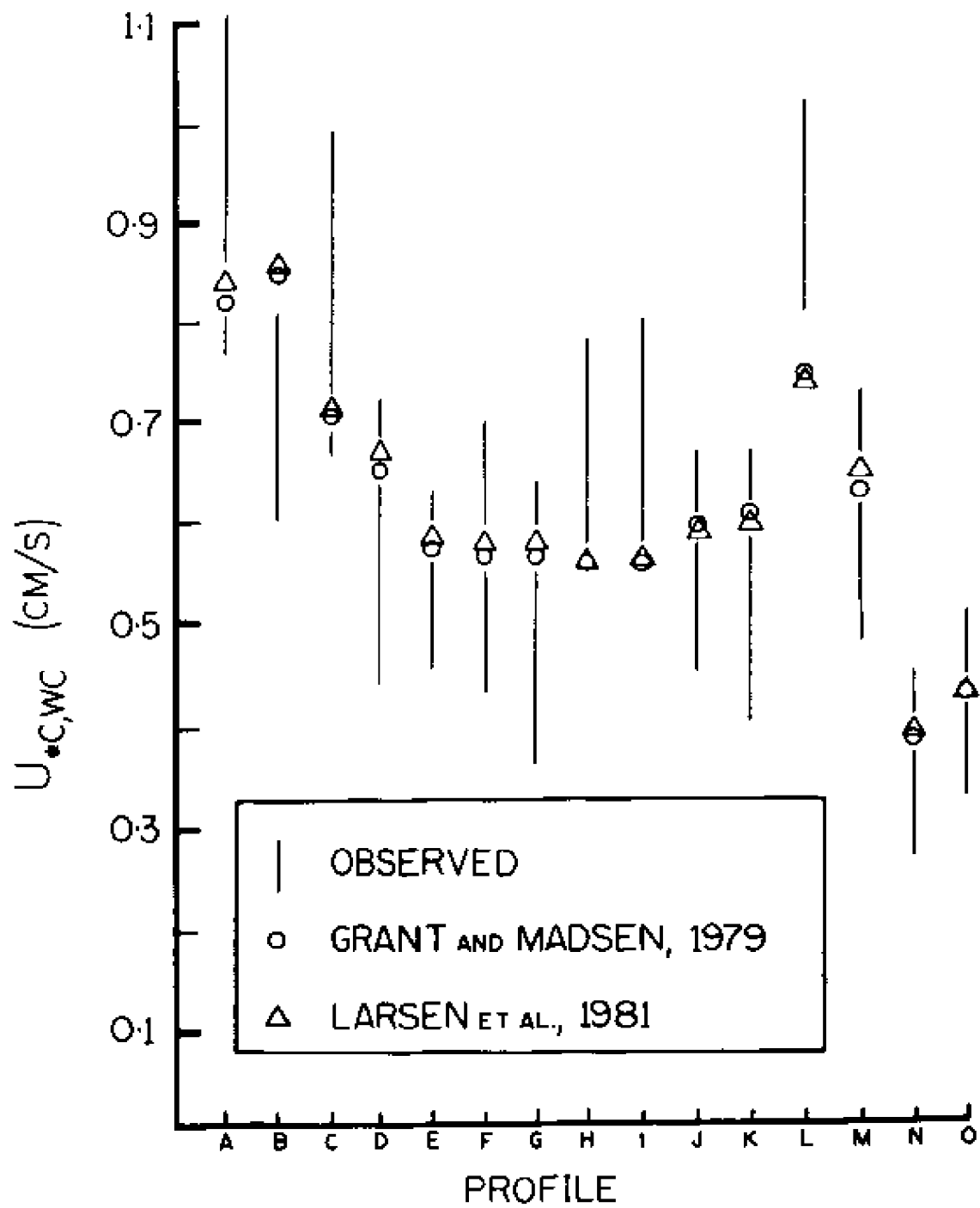
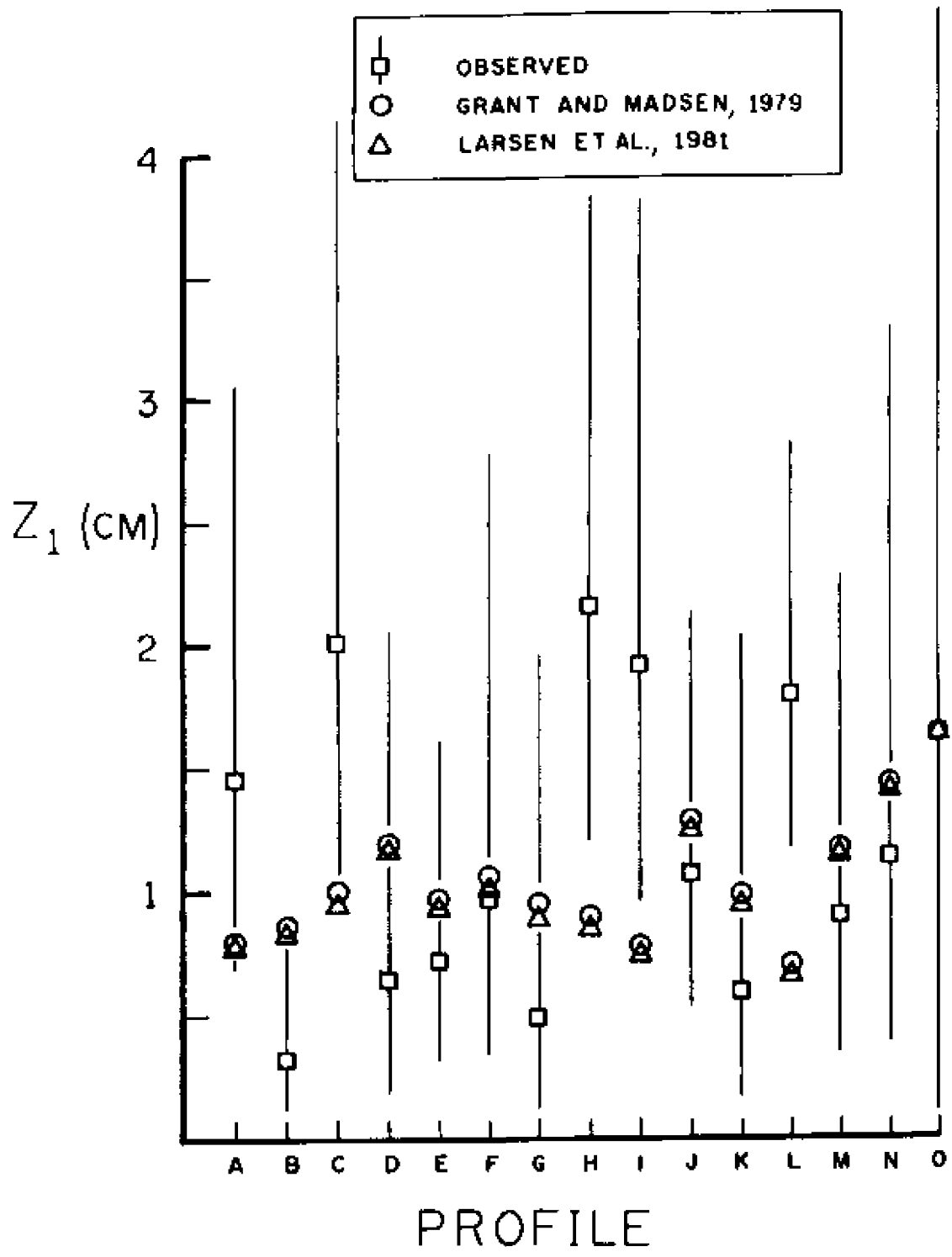


Figure 3.15 Comparison of: z_1 calculated by Grant et al. (1983) using the method of Grant and Madsen (1979) with the CODE-1 parameters reported by Grant et al. (1983); z_1 calculated using the method of Larsen et al. (1981) with the same parameters; and the CODE-1 observations reported by Grant et al. (1983). The vertical lines represent the computed error range of the observed roughness.



3.4.2 Flux calculations

Bedload transport in the sea has been measured using radioactive tracers (Lavelle et al., 1978; Heathershaw and Carr, 1977); fluorescent tracers (Miller and Komar, 1979; Lees, 1979; Murray, 1967); acoustic instruments (Thorne et al., 1983); bedform-migration rates (Kachel and Sternberg, 1971; Langhorne, 1982); and lighted rods (Wilkinson, 1986). Still, field verification of the bedload-transport equations has been sparse. Several field experiments have tested the steady-flow transport equations (e.g. Gadd et al., 1978; Lavelle et al., 1978; Heathershaw, 1981; Heathershaw et al., 1981; Lees, 1983; Hardisty, 1983). Only a few experiments have been designed to verify combined-flow transport equations.

Pattiaratchi and Collins (1985) compared predicted rates of combined-flow bedload transport with data from a fluorescent-tracer study. The tracer was released in 20 to 40-m water depth in an area of high tidal-current and wave energy in the northern Bristol Channel, UK. Transport rates inferred from the tracer experiments were compared to predictions by a number of methods: the traction approaches of Madsen and Grant (1976), Vincent et al. (1981) and Bijker (1971); Bagnold's (1963) energetics model for combined flow; and the steady-flow equations of Einstein (1950), Frijlink (1952), Yalin (1963), Engelund and Hansen (1967), Sternberg (1972), Ackers and White (1973) and Gadd et al. (1978) all modified to apply to combined flow. The performance of the equations was assessed against a number of criteria: observed transport rates had to be accurately predicted; an increase in the observed wave-orbital velocity had to produce a corresponding increase in the

predicted transport rate; and the predicted combined-flow transport rates had to be substantially greater than rates predicted by current-only models. Pattiaratchi and Collins concluded that only the models of Madsen and Grant (1976) and Sternberg (1972) (modified to apply to combined flow) performed credibly. Each of these models were said to "provide realistic estimates of transport under the combined influence of wave- and tidally induced currents, in comparison with field measurements" (Pattiaratchi and Collins, 1985, p. 97).

Niedoroda et al. (1982) used Madsen and Grant's (1976) transport model to reproduce observations of sedimentation rates in a test pit on the central California inner shelf. They also concluded that the model was sound for waves and currents and, by including a slope-correction term, they achieved a good correspondence between predictions and observations.

3.4.3 Sensitivity analysis

Given the high power-dependence of transport on velocity, it is important to evaluate the sensitivity of the model calculations and assess the errors involved in measuring each of the model parameters.

The current meters were calibrated in the Virginia Institute of Marine Science's (VIMS) recirculating flume (dimensions: 90 cm x 100 cm x 12 m) prior to and at the conclusion of each deployment. Each axis was independently calibrated. Aubrey and Trowbridge (1985), reporting on an extensive series of laboratory tests of the Marsh-McBirney electromagnetic current meters, found that a two-segment linear calibration model consistently gave lower residual errors than did a

single-segment model. Aubrey and Trowbridge hypothesized that the meter's sensitivity (inverse of gain) changed with the transition from laminar to turbulent boundary-layer flow, however they could find no consistency in cutoff Reynolds number that would support such a postulate. Applying a two-segment calibration model (cutoff at 60 cm/s) to the VIMS test data resulted in a decrease in the root-mean-square residual to 1-2 cm/s (Figure 3.16). A two-segment calibration model, unique for each axis, was thus used to convert recorded voltages to component current speeds.

Aubrey and Trowbridge found no significant difference between pure oscillatory- and pure steady-flow sensitivity, however, for combined flow, the steady sensitivity increased by 7-10% and the oscillatory sensitivity by 9-21%. Concomitantly, the error variance increased by up to 70%. This behaviour was attributed to the complex wake structure in the combined flow.

Aubrey and Trowbridge also found that the flow structure generated by the quadrantal distribution of the electrodes caused a Reynolds number-dependent horizontal cosine response. The sensitivity varied as the electrode rotated from the forward stagnation point and the largest errors occurred when the flow was 90° from head-on. A further source of error was identified as the structure of the free-stream flow itself: for free-stream turbulence intensities (defined as the ratio of the root-mean-square velocity to the free-stream velocity) greater than 1%, steady sensitivity was affected. Aubrey and Trowbridge noted that turbulence intensities in shelf depths of 20-40 m commonly exceed 1%.

The sensitivity of model calculations to errors in U_c is demonstrated in Figure 3.17 with the aid of a "reference stress value"

Figure 3.16 Steady-flow calibration of one axis of a Marsh-McBirney Model MM551M (4.0-cm diameter sphere) electromagnetic current meter. A two-segment linear model was fitted independently to the Y and X axes.

MM551M
S/N 0520
Y-AXIS

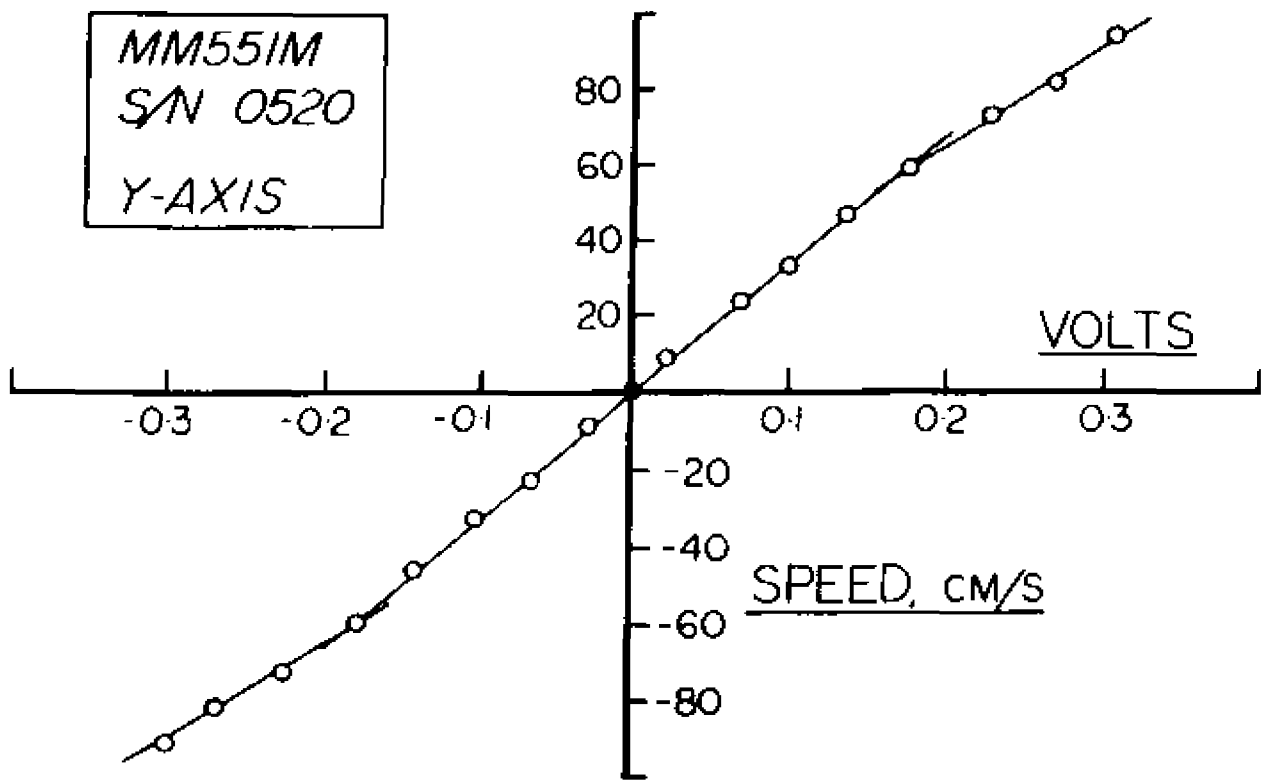
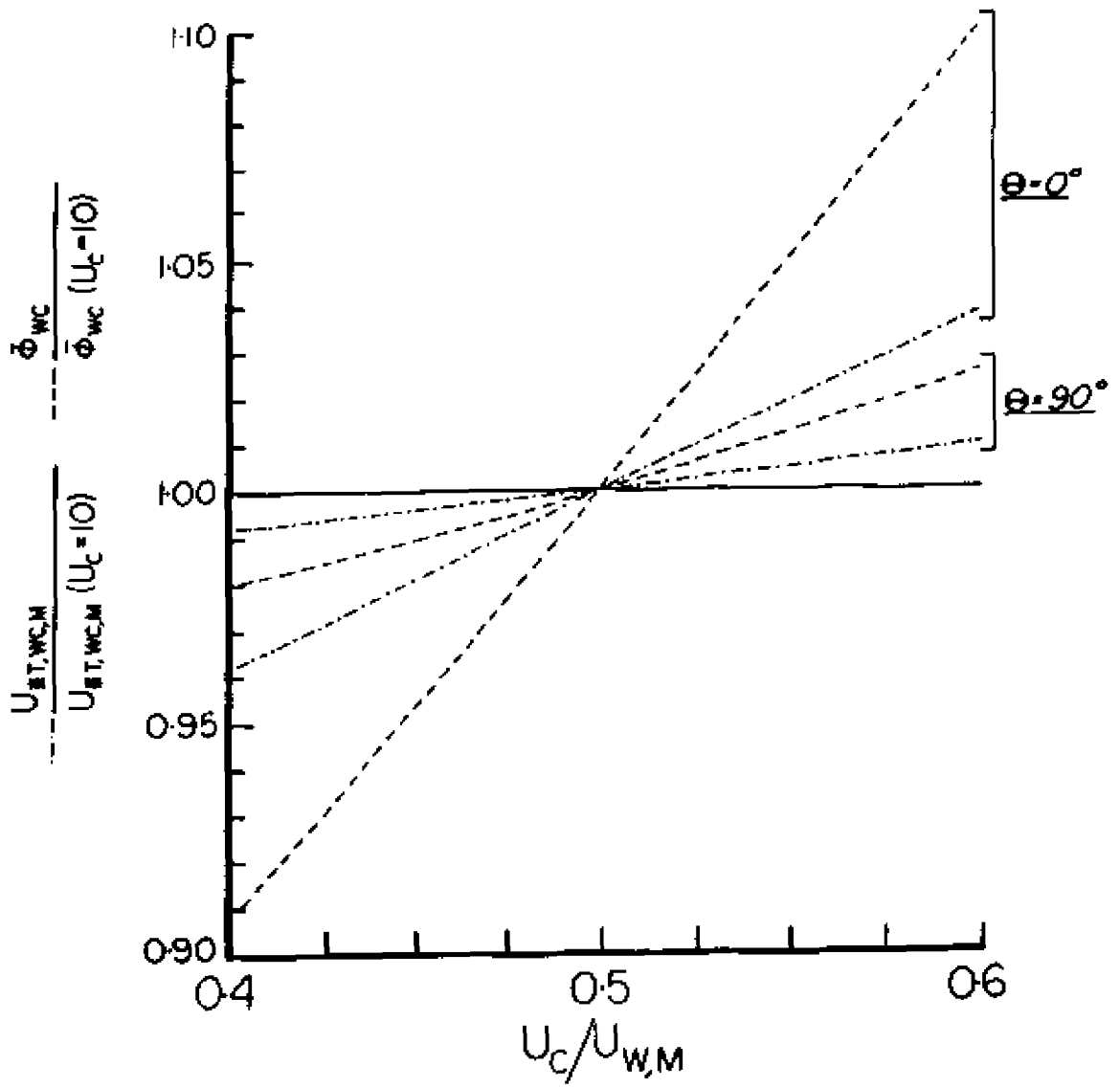


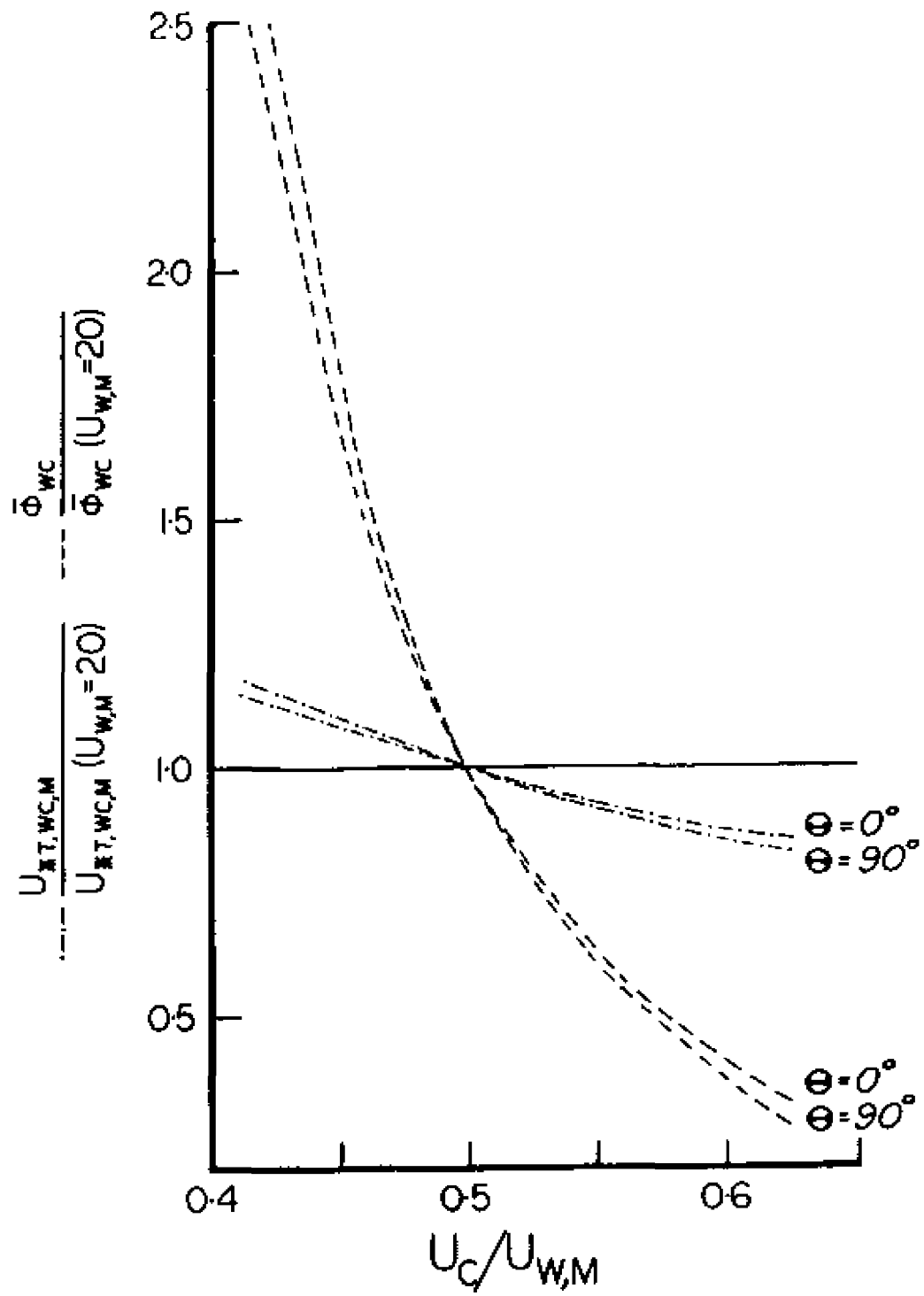
Figure 3.17 Sensitivity of stress and transport predictions to variations in U_c . Plotted is the ratio of $U_{*t,wc,m}$ to the reference stress value ($U_{*t,wc,m}$ with $U_c = 10$ cm/s and $U_{w,m} = 20$ cm/s), where $U_{*t,wc,m}$ is calculated over the range $U_c/U_{w,m} = 0.4$ to 0.6 with $U_{w,m}$ held constant at 20 cm/s. Also plotted is the ratio of $\bar{\phi}_{wc}$ to the reference transport value ($\bar{\phi}_{wc}$ with $U_c = 10$ cm/s and $U_{w,m} = 20$ cm/s) where $\bar{\phi}_{wc}$ is calculated over the same range.



and a "reference transport value" that are both typical of observed fairweather magnitudes. The reference stress value is defined as $U_{*t,wc,m}$ corresponding to $U_c = 10$ cm/s and $U_{w,m} = 20$ cm/s, and the reference transport value as $\bar{\phi}_{wc}$ corresponding to $U_c = 10$ cm/s and $U_{w,m} = 20$ cm/s. Plotted in the figure is the ratio of $U_{*t,wc,m}$ to the reference stress value where $U_{*t,wc,m}$ is calculated over the range $U_c/U_{w,m} = 0.4$ to 0.6 with $U_{w,m}$ held constant at 20 cm/s. Also plotted is the ratio of $\bar{\phi}_{wc}$ to the reference transport value, where $\bar{\phi}_{wc}$ is calculated over the same range. Corresponding to a deviation of $\pm 20\%$ from $U_c = 10$ cm/s, is a deviation of less than 10% in $\bar{\phi}_{wc}$ from the reference value for co-directional flow and less than 4% for orthogonal flow.

The choice of $U_{1/10}$ as the parameter to represent wave intensity is designed to reflect the strongest oscillatory events (Shi et al., 1985). Another possibility is $U_{1/3}$, the "significant" orbital velocity, which is the average of the highest one-third of the wave-orbital velocities. Analysis of selected bursts from each of the deployments revealed that $U_{1/10}$ was typically 20% higher than $U_{1/3}$. The sensitivity of the model calculations to errors in $U_{w,m}$ is demonstrated in Figure 3.18, again with the aid of the reference values defined above. Plotted is the ratio of $U_{*t,wc,m}$ to the reference stress value, where $U_{*t,wc,m}$ is calculated over the range $U_c/U_{w,m} = 0.4$ to 0.6 with U_c held constant at 10 cm/s. Also plotted is the ratio of $\bar{\phi}_{wc}$ to the reference transport value, where $\bar{\phi}_{wc}$ is calculated over the same range. Corresponding to a deviation of $\pm 20\%$ from $U_{w,m} = 20$ cm/s is a deviation in $\bar{\phi}_{wc}$ from the reference value of greater than 250% for both co-directional and orthogonal flow.

Figure 3.18 Sensitivity of stress and transport predictions to variations in $U_{w,m}$. Plotted is the ratio of $U_{*t,wc,m}$ to the reference stress value, where $U_{*t,wc,m}$ is calculated over the range $U_c/U_{w,m} = 0.4$ to 0.6 with U_c held constant at 10 cm/s. Also plotted is the ratio of $\bar{\phi}_{wc}$ to the reference transport value, with $\bar{\phi}_{wc}$ calculated over the same range.



The expression given in equation 2.41 for z_0 is only valid if the flow is fully rough turbulent; if the flow is transitional or smooth turbulent, z_0 also varies with a Reynolds number that is applicable to the wall layer of the flow (Smith, 1977). Jonsson (1966) delineated oscillatory-flow regimes in terms of the relative roughness (A/k) and wave Reynolds number, $RE = U_{w,m} A/\nu$, where ν is the kinematic fluid viscosity. Observed burst-averaged values of RE and A/k (where k is given by the ripple roughness; equation 2.44 with $n = 3$ cm, $\lambda = 15$ cm and $C_3 = 27.7$) for the mid-shoreface experiment are plotted in Figure 3.19 together with Jonsson's transition criteria. The data confirm that the observed flow was rough turbulent at all times during the experiment, thus vindicating the use of equation 2.41 in the stress calculations. A similar analysis confirmed that the flow was rough turbulent at all times during the lower- and upper-shoreface experiments.

The sensitivity of skin-friction and transport predictions to variations in the grain roughness, k_G , is demonstrated as follows. With U_G set at 10 cm/s and $U_{w,m}$ at 20 cm/s, $U_{*t,wc,m}'$ and $\bar{\phi}_{wc}$ were calculated using each of the three formulations for k_G described in section 2.5 (equation 2.43). The sediment parameters used in the calculation were: $D_{50} = 0.010$ cm and $D_{90} = 0.015$ cm, which are applicable to the 17.5-m depth site. Results are shown in Table 3.2. The calculated values of $U_{*t,wc,m}'$ and $\bar{\phi}_{wc}$ vary by factors of -1.1 and -2.3 respectively for co-directional flow, and by factors of -1.1 and -2.5 for orthogonal flow.

It was noted in section 2.5 that, when the bed is rippled, calculating skin friction from the observed mean velocity above the internal boundary layer could lead to significant errors if the form

Figure 3.19 Classification of flow regimes, mid-shoreface experiment. Plot of observed RE versus A/k , calculated from burst-averaged flow quantities. Superimposed on the plot is Jonsson's (1966) transition criterion.

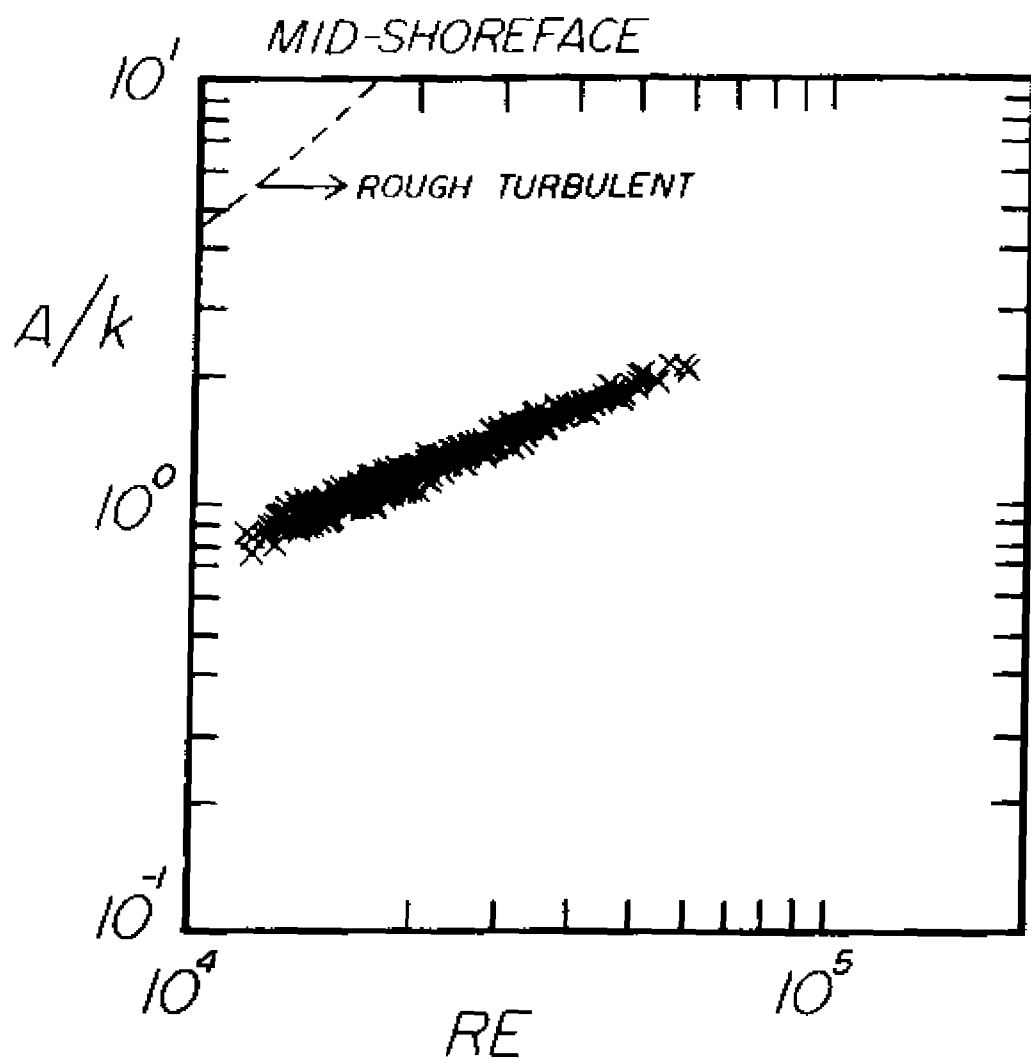


Table 3.2 Sensitivity of stress and transport predictions
to variations in k_G . $U_c/U_{w,m} = 0.5$, $D_{50} = 0.010$
cm and $D_{90} = 0.015$ cm.

	k_G (cm)	$U_{*t,wc,m}$ (cm/s)	$\bar{\phi}_{wc}$
a. $\theta = 0^\circ$			
	D_{50}	1.43	0.016
	2.5 D_{50}	1.59	0.032
	2 D_{90}	1.63	0.037
b. $\theta = 90^\circ$			
	D_{50}	1.23	0.011
	2.5 D_{50}	1.38	0.022
	2 D_{90}	1.42	0.026

drag is large. Bed shear stress inferred from the velocity profile above the internal boundary layer is an overestimate of the actual skin friction on a rippled bed (Chriss and Caldwell, 1982). However, any method that uses a single-point estimate of velocity will underestimate the skin friction because any one measurement of the mean current over a rippled bed will be lower than if the bed were flat. The following analysis demonstrates the effect of form drag on the observed mean-current speeds that were used in the wave-current boundary-layer model to calculate the skin frictions. Equation 2.24 was used to calculate U_{100} given various free-stream velocities and by both including and neglecting the ripple roughness in the calculations. The ripple roughness was calculated using equation 2.44 with $\eta = 3$ cm, $\lambda = 15$ cm and $C_3 = 27.7$; $U_{w,m}$ was 20 cm/s; T was 10 s; and the flow was co-directional. For a free-stream mean-current speed of 15 cm/s, U_{100} was -10 cm/s by including the form drag, and -12 cm/s by neglecting it. For a free-stream speed of 25 cm/s, U_{100} was -17 cm/s by including the form drag and -21 cm/s by neglecting it. Thus, using observed velocities as though they are unaffected by form drag should lead to an error in the calculated value of skin friction that is only about the same as that due to the imperfect response of the current meters themselves.

Compared to the sensitivity to variations in U_c , $U_{w,m}$ and k_G , the model calculations are relatively insensitive to expected variations in angle between the wave and current, wave period and reference elevation of the driving parameters.

4. A MODEL FOR LOW-ENERGY BEDLOAD TRANSPORT ON THE SHOREFACE

4.1 Introduction

The following analysis addresses two scenarios: (1) onshore net bedload transport, and (2) offshore net bedload transport. Observed events, where an event is defined as a period of time during which critical bed shear stress is exceeded and thus bed sediment is in motion, form the basis of the analysis. The objective, introduced in Chapter 1, is to elucidate the controls exerted by the first three moments of the combined-flow velocity distribution on the magnitude and direction of bedload transport, where those moments are the mean flow, the wind-wave energy, and the wind-wave asymmetry respectively. The effect of the threshold criterion is also addressed, since this was identified in Chapter 2 as being potentially important in low-energy flow.

A one-dimensional numerical model that simulates the cross-shore velocity and bedload-flux fields is used to model the bedload-flux divergence across the shoreface. For each scenario, sediment pathways and areas of net deposition (flux convergence) and net erosion (flux divergence) are identified and explained in terms of flow parameters.

The analysis of onshore transport is based on the conditions that existed during event C (lower-shoreface experiment, 22-m water depth). Event D, which also occurred during the lower-shoreface experiment, was

identical to event C in all essential respects. The analysis of offshore transport is based on event A (mid-shoreface experiment, 17.5-m water depth). Event B (mid-shoreface experiment), which contains elements of both scenarios, will be discussed separately.

4.2 Onshore Transport

4.2.1 Local transport

The wind was light (<20 km/hr) and from the southeast and southwest quadrants for the duration of the lower-shoreface (22-m depth) deployment. During the first half of the experiment, waves were low and the mean current rotated at approximately the semi-diurnal tidal frequency, ebbing to the south and offshore, and flooding to the north and onshore (Figure 3.11). Approximately 36 hours into the experiment, the mean flow strengthened and set alongshore to the south. This condition persisted for the next 24 hours until (and presumably beyond) the termination of the experiment. Events C and D occurred during this time.

Event C (marked as such on Figures 3.11, 3.12 and 3.13) was approximately 9.7 hours duration. Simultaneous increases in U_{100} and $U_{1/10}$ initiated the event; U_{100} increased to an average (over the event) of ~13 cm/s and $U_{1/10}$ to ~22 cm/s (Figure 3.12). Peak spectral period as inferred from the velocity measurements at the bed was 14 to 16 s (Figure 3.12). The significant wave height coincident with event C, as recorded by a waverider shoreward of the experiment site in 18.5-m water depth, was 0.70 m (CERC, 1984).

Prior to the event, $U_{1/10}$ exceeded U_{100} by up to a factor of 10; during the event, $U_{1/10}$ was, on average, 1.6 times the magnitude of U_{100} (Figure 3.13). Although the wave component of the total skin friction was on average two times the magnitude of the current component (Figure 3.13), the components add together as vectors through varying angles and hence a straight comparison of magnitudes is not truly indicative of the relative contribution made by each to the total skin friction. The ratio of total skin friction calculated from the wave and current in combination to skin friction calculated on the assumption that the superimposed current speed is zero (i.e. $\tau_{t,wc,m}'/\tau_{w,m}'$) is a more useful indicator. The average (over the event) of this ratio was 1.17, indicating that -85% of the total skin friction was due to the wave-orbital velocity.

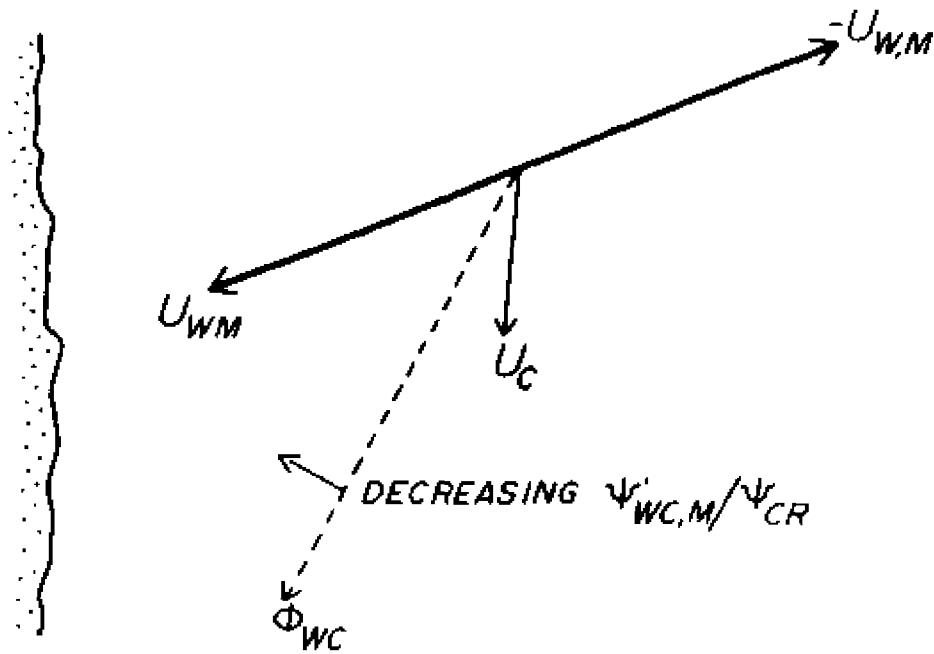
The net combined-flow sediment-transport rate assuming symmetrical wave-orbital velocity ($\hat{\phi}_{wc}$) averaged 0.0078 (dimensionless) over the event, or, in units of weight per unit width (\hat{q}_{wc}), 0.41 g/s³ (Figure 3.13). The net rate was -135% of the average back-and-forth transport rate, i.e. $|\hat{\phi}_{wc}|/\bar{\phi}_{wc} = 1.35$ (Figure 3.13), indicating that net transport did not originate from only a very small disparity in the forward and reverse transport rates under the wave. The waves propagated slightly to the south of shore-normal and the mean current set to the south and onshore over the duration of the event (Figures 3.11 and 3.12). Because $\psi_{wc,m}'/\psi_{cr}$ was consistently small, the "threshold effect" (i.e. rotation of the net transport vector due to the threshold-induced asymmetry in the instantaneous combined-flow transport rate) augmented significantly, in this case, the onshore component of net transport. The measure of this effect can be obtained by defining an angle, ζ , such that ζ is the

angle that $\hat{\phi}_{wc}$ is rotated relative to \hat{U}_c . By definition, ζ is positive if $\hat{\phi}_{wc}$ is rotated onshore of \hat{U}_c , and vice versa. Consider the following clarifying example applied to the Duck shoreline, which trends 20° west of north. If \hat{U}_c is directed to 230° and $\hat{\phi}_{wc}$ to 220° , then $\hat{\phi}_{wc}$ is rotated 10° offshore relative to \hat{U}_c , and hence $\zeta = -10^\circ$. As a further example, suppose \hat{U}_c is directed to 290° and $\hat{\phi}_{wc}$ to 240° , then $\zeta = +10^\circ$. Shown in Figure 4.1 is a schematic of the threshold-induced rotation of net transport in relation to the mean current and symmetrical wave-orbital velocity. Since the net bedload-transport vector is constrained to lie between the mean flow and that stroke of the wave that makes an acute angle with the mean flow, $\hat{\phi}_{wc}$ was, like \hat{U}_c , directed to the south and onshore. Within that acute angle, $\hat{\phi}_{wc}$ was rotated onshore relative to \hat{U}_c (i.e. ζ was positive) due to the threshold-induced asymmetry in the instantaneous transport rate.

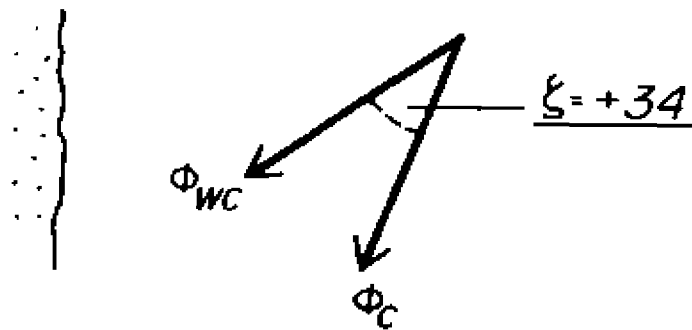
The event-integrated bedload transport was found by summing each burst-averaged estimate of $\hat{\phi}_{wc}$ multiplied by the burst interval. The same integration was performed on another transport quantity ($\hat{\phi}_c$) that had the same magnitude as $\hat{\phi}_{wc}$ but the direction of \hat{U}_c , this for the purpose of assessing the significance of the threshold effect. After 9.7 hours (the duration of the event), the onshore component of $\hat{\phi}_{wc}$ was 216% of the onshore component of $\hat{\phi}_c$, which corresponded to $\zeta = +34^\circ$ (Figure 4.1). Hence, the onshore component of bedload transport was considerably enhanced by the threshold effect over the duration of the event.

Figure 4.1 Onshore transport: event C, lower shoreface. Schematic of threshold-induced rotation of net transport in relation to mean current and symmetrical wave-orbital velocity. After 9.7 hours (event duration), cumulative net transport was turned onshore 34° by the threshold-induced asymmetry in the instantaneous transport rate.

ONSHORE TRANSPORT



EVENT C - AFTER 9.7 HOURS



4.2.2 Cross-shore gradient in transport

The local rate of change in sediment volume (i.e. erosion or deposition) is equal to the sediment-flux divergence; therefore single-point measurements of sediment flux per se are uninformative in this regard. Consider the sediment-flux field $\hat{Q}_{wc}(x,y)$, where \hat{Q}_{wc} is the volume rate of bedload sediment transport per unit width due to combined wave and current flow (units: cm^2/s). The general conservation equation (e.g. Pond and Pickard, 1978) applies:

$$\partial z/\partial t = -[(\partial Q_{wc,x}/\partial x) + (\partial Q_{wc,y}/\partial y)] \quad (4.1)$$

where $Q_{wc,x}$ and $Q_{wc,y}$ are the x and y components respectively of \hat{Q}_{wc} and $\partial z/\partial t$ is the local rate of vertical accretion ($\partial z/\partial t$ positive) or erosion ($\partial z/\partial t$ negative). A sediment pathway (i.e. no net deposition or erosion) exists where the divergence of the sediment flux is zero.

In the following analysis, a numerical model is used to predict bedload-flux divergence on the shoreface. The basis of the model is the prediction of the transformation a wave undergoes by the processes of shoaling, refraction and frictional dissipation as it propagates towards shore over a specified bathymetric profile and through a specified mean-current field.

A wave propagating shoreward from outer depth, h_1 , to inner depth, h_2 , undergoes a transformation in wave height that is given by:

$$H_2 = H_1 K_s K_r K_f \quad (4.2)$$

where H_2 and H_1 are wave heights at depths h_2 and h_1 respectively, and K_s , K_r and K_f are the shoaling, refraction and frictional dissipation coefficients respectively. The following initial conditions are required for application of the model: deepwater (i.e. at the base of the model bathymetric profile) wave height, period and angle of incidence; and cross-shore variation in mean-current speed and direction. The detailed description of the numerical model and verification of certain equations used in the model are left for the Appendix.

The similarity of shore-normal profiles that were separated in the longshore dimension by several kilometers was taken as evidence of the longshore uniformity of the shoreface bathymetry (section 3.2.1). Thus, it is possible to reduce the analysis to one dimension (i.e. assume $\partial Q_{wc,y} / \partial y = 0$) without losing any vital information. For computational purposes, it is expedient to represent the observed depths by some continuous analytical expression. Dean (1977) showed that an equation of the form:

$$h = m x^p \quad (4.3)$$

reproduced the offshore profile, where x is the distance offshore, and the coefficients m and p are found by a least squares fit of equation 4.3 to observed depth data. For purposes of convenient description, the model profile was obtained by fitting equation 4.3 to an average of the observed profiles (see Figure 3.2) over the domain $200 \text{ m} < x < 5000 \text{ m}$, which corresponds to $3.64 \text{ m} < h < 23.09 \text{ m}$ (i.e. from near the outer bar

of the surfzone to the base of the shoreface). The (average) shoreline is located at $(x,h) = (0,0)$.

There was no obvious trend to the shore-normal distribution of surficial sediments in the range $3.64 \text{ m} < h < 23.09 \text{ m}$ (see section 3.2.1), therefore a single value (0.13 mm) was chosen to represent the mean grain-size of the shoreface sediments. The corresponding critical Shields parameter is 0.060 (Madsen and Grant, 1976). The dimensions of the wave-generated ripples were taken as: $\eta = 3 \text{ cm}$, $\lambda = 15 \text{ cm}$. A full discussion of the effect of ripple dimensions on the model calculations is provided in the Appendix.

The model bathymetric profile was divided into 100-m intervals and the wave-transformation equations were solved in each successive segment, the transformed wave height at the inner end of one segment acting as the initial condition for the next adjacent segment. Local wave height was therefore estimated every 100 m. Linear wave theory was used to calculate the cross-shore distribution of wave parameters. Given the cross-shore variation in H , h and \hat{U}_c , the corresponding variation in $\hat{\phi}_{wc}$ was calculated using the transport theory detailed in Chapter 2. The dimensionless net transport rate, $\hat{\phi}_{wc}$, was converted to a volume rate, \hat{Q}_{wc} , by multiplying by $\rho_s g w D$. The local gradient in volume flux, $\partial \hat{Q}_{wc,x} / \partial x$, was estimated at the center of each segment and converted to a local rate of sedimentation (equation 4.1) by assuming that the bulk sediment porosity reduced the effective sediment density by 30%.

The central problem in the model simulation is the definition of the cross-shore variation in the mean-current velocity. During event C, the semi-diurnal tidal-current rotation was replaced by a steady mean

flow, which is indicative of a coherent mean-current field of possible broad spatial extent and complex structure. Coastal-boundary-layer flow theory is of no assistance in defining the mean-flow field, firstly because classical models (e.g. Csanady, 1982) fail in the shoreface region, even when friction terms are included (Niedoroda et al, 1985), and secondly because it is unclear what the pertinent driving terms and scales are. Observational data are also of no assistance; the description in the literature of the spatial and temporal variability of subtidal currents has previously been concerned only with high-energy wind-driven episodes. For the purposes of the following analysis, the mean-current field will be assumed to be uniform, i.e. the mean current at every point on the shoreface is set equal to the observed mean current at 22-m depth.

Observed currents were essentially steady and unidirectional over the duration of the event, which can be exploited to further simplify the model simulation: one set of initial conditions will suffice to predict the local sedimentation rate ($\partial z/\partial t$) at every point on the shoreface profile and this rate will be assumed to apply for the duration of the event. The net erosion or deposition at a point (δz) is thus obtained by multiplying the local predicted sedimentation rate (either positive or negative) by the duration of the event.

The initial model conditions chosen to represent event C were as follows: $T = 14.5$ s (observed average peak spectral period) and deepwater wave height and direction = 0.70 m and 235° respectively. Deepwater refers to 23.5-m depth, which is the seaward base of the model profile. These initial conditions were chosen such that predicted wave parameters coincided with observed values at both the experimental site

at 22-m depth and the waverider site at 18.5-m depth. The mean-current velocity at every point on the shoreface was set equal to the observed mean-current velocity at 22-m depth: 14.0 cm/s at 100 cm above the bed directed to 170° , i.e. to the south and onshore.

Shown in Figure 4.2 are the predicted cross-shore distributions of $\hat{\phi}_{wC}$; $\hat{\phi}_{wC,x}$; $U_{*w,wC,m}^1$ and $U_{*c,wC}^1$; ζ ; and δz , where δz is the predicted net erosion (δz negative) or accretion (δz positive) that occurred over the duration of the event, and $\hat{\phi}_{wC}$ was calculated assuming symmetrical wave-orbital velocity.

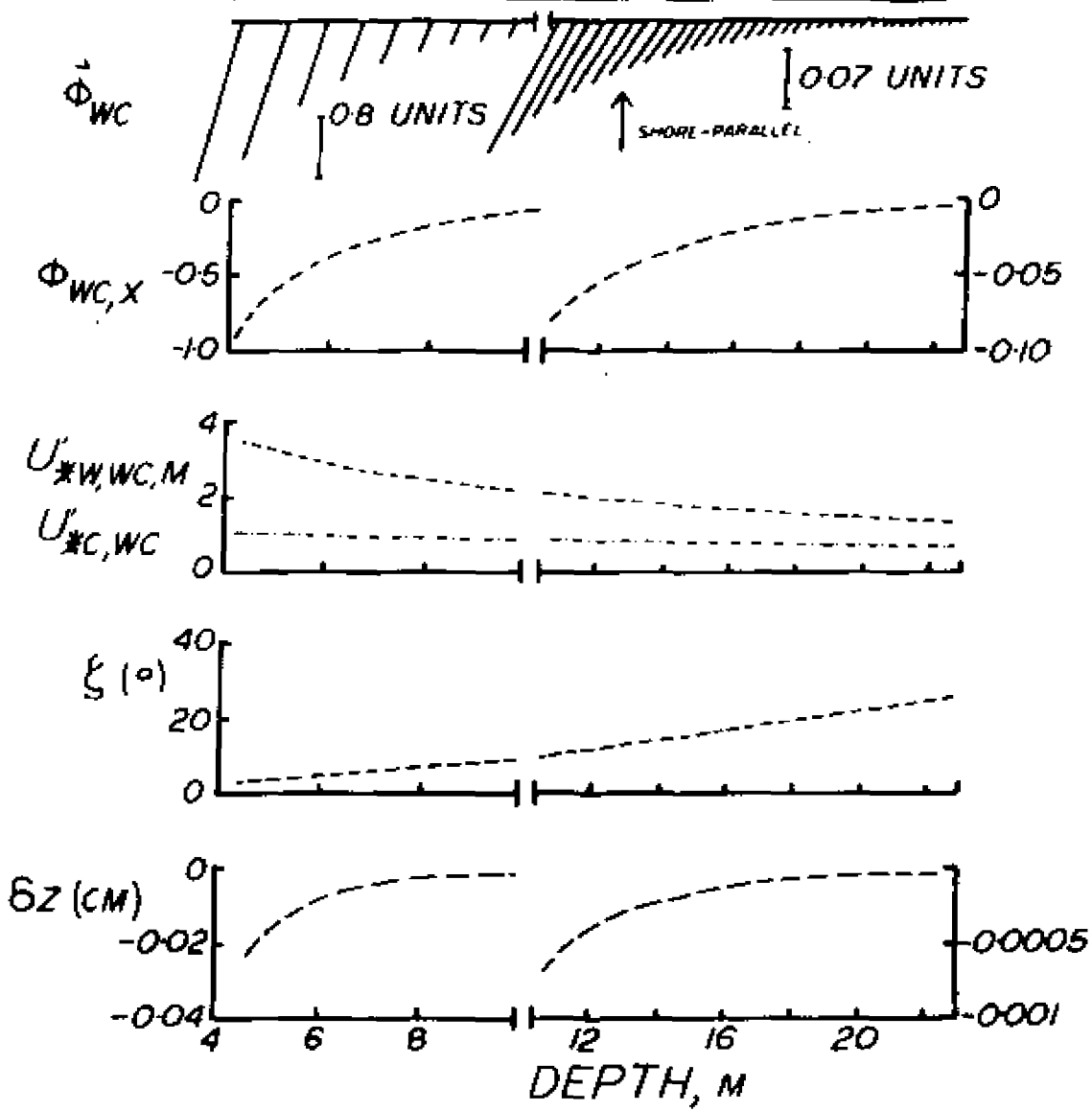
Net bedload flux increased in magnitude with decreasing depth, driven primarily by the cross-shore increase in $U_{*w,wC,m}^1$ and secondarily in $U_{*c,wC}^1$. At every point on the shoreface, net bedload flux was directed south and onshore. As the ratio $\psi_{wC,m}^1/\psi_{cr}$ increased approaching shore, $\hat{\phi}_{wC}$ turned offshore in the direction of \hat{U}_c ; consequently ζ decreased from $+28^\circ$ at 22-m depth to $+3^\circ$ at 4-m depth.

Cross-shore changes in magnitude and direction of $\hat{\phi}_{wC}$ thus drove changes in $\hat{\phi}_{wC,x}$ that were opposite in sense: the increasing magnitude of $\hat{\phi}_{wC}$ caused a shoreward decrease in $\hat{\phi}_{wC,x}$ (i.e. $\hat{\phi}_{wC,x}$ became more negative), while the rotation of $\hat{\phi}_{wC}$ caused the opposite. Positive sediment-flux divergence (erosion) at every point on the shoreface is defined by the former; negative divergence (accretion) by the latter. Bed shear stress was the dominant control: the predicted outcome was shoreward-directed transport and erosion at every point on the profile, with the local rate of deflation increasing towards shore (Figure 4.2).

At some point, the bedload-flux divergence must reverse in order to conserve sediment, i.e. sediment eroded from the shoreface and transported shorewards must be deposited. The reversal may occur at the

Figure 4.2 Onshore transport, symmetrical wave-orbital velocity: event C. Predicted cross-shore distributions of $\hat{\phi}_{wc}$; $\phi_{wc,x}$; $U_{*w,wc,m}^+$ and $U_{*o,wc}^+$; ζ_i and δz .

EVENT C - SYMMETRIC WAVE



shoreface-surfzone boundary (i.e. breakpoint) with the fundamental change in fluid motions that occurs there, or it may occur on the shoreface itself as follows. Consider a total sediment flux, where the bedload component of that flux is directed onshore (negative sign) and the suspended component is directed alongshore, advected by the mean current (Figure 4.3). Approaching shore, the near-bed wave-orbital velocities become more energetic, which, in conjunction with the rippled bed, results in an increasing proportion of the total sediment flux moving as suspended load. There may exist a point on the shoreface such that shoreward of that point the proportion of sediment moving as suspended load increases faster than does the total amount of sediment in motion. Hence, shoreward of that point the bedload component of the total sediment flux increases (i.e. become less negative), which reverses the sign of the spatial derivative of that component relative to the sign seaward of that point. Thus, sediment eroded as bedload from seaward of that point is deposited across the shoreface shoreward of that point, steepening the shoreface profile in the process.

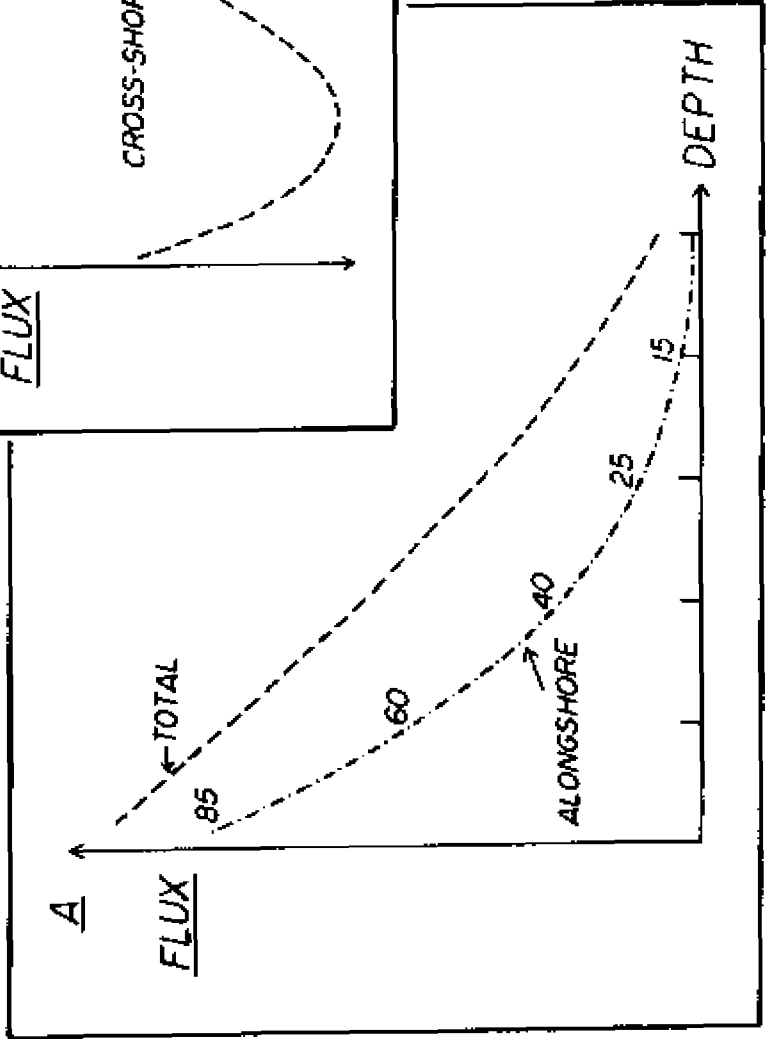
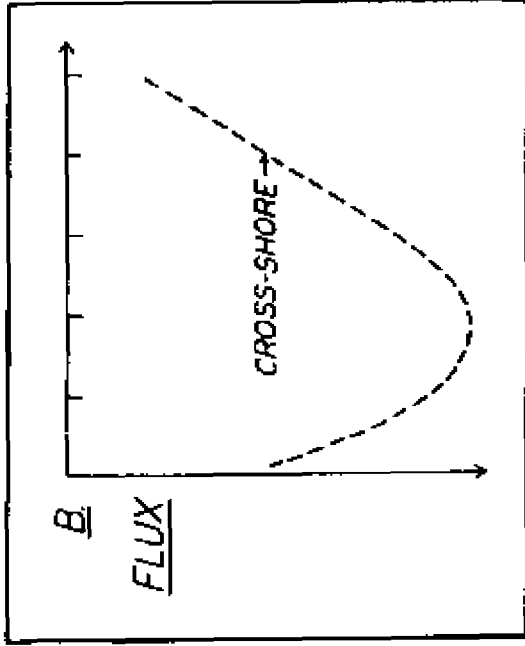
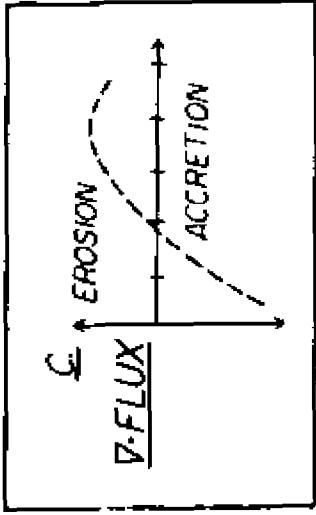
4.2.3 Effect of wave asymmetry

The model calculations thus far have allowed only for transport by a mean current superimposed on symmetrical wave-orbital velocities. The following analysis is intended to elucidate the control exerted by wave asymmetry on the cross-shore gradient of combined-flow bedload flux.

The asymmetric wave-orbital velocity is incorporated into the calculation of net combined-flow transport by integrating the general transport equation (2.39) over the wave period, where the wave-orbital

Figure 4.3 The proportion (numbers in A) of total sediment flux advected alongshore as suspended load increases shoreward. The cross-shore component of total flux, directed onshore as bedload, therefore varies as in B. The profile response (C) is given by the derivative of the curve in B: the profile is steepened by deposition across the top of the shoreface of sediment eroded from deeper water.

ONSHORE TRANSPORT



velocity is given by the second-order equation (2.40). The cross-shore distribution of $\hat{\phi}_{wc}$, where the wave-orbital velocity is now skewed in the direction of wave propagation, was calculated using the initial conditions that have been defined as being representative of event C.

The skewed wave-orbital velocities reinforced the stress-driven shoreward decrease in $\phi_{wc,x}$. The outcome, assuming a reversal in the bedload-flux divergence beginning at some point on the shoreface or upon entering the surfzone, was simply a more rapid steepening of the shoreface profile.

4.3 Offshore Transport

4.3.1 Local transport

The wind was light (<20 km/hr) and blew onshore for the duration of the mid-shoreface (17.5-m depth) deployment. Event A (marked as such on Figures 3.6, 3.7 and 3.9) was approximately 2.5 hours duration and coincided with an ebbing tide. The event was initiated by simultaneous increases in U_{100} and $U_{1/10}$; U_{100} increased to an average (over the event) of -12 cm/s and $U_{1/10}$ to -21 cm/s (Figure 3.6). Peak spectral period inferred from measured near-bed velocities was 8 to 9 s (Figure 3.7), which is in agreement with the peak spectral period of 8.83 s reported from a nearby waverider in 18.5-m water depth on the same shore-normal transect (CERC, 1983). Significant wave height, recorded by the same waverider, was 0.88 m.

During the event, $U_{1/10}/U_{100}$ averaged -2 (Figure 3.9). $U_{*w,wc}'$ was, on average, three times the magnitude of $U_{*c,wc}'$ (Figure 3.9), however

the ratio of total skin friction calculated from the wave and current in combination to skin friction calculated on the assumption that the mean current was zero, averaged 1.10 over the event. Thus, 90% of the total skin friction was due to the wave-orbital velocity.

Net dimensionless combined-flow sediment-transport rate, assuming symmetrical wave-orbital velocity, averaged 0.012 (0.31 g/s^3) over the duration of the event, which was, on average, -30% of the average back-and-forth transport rate, i.e. $|\hat{\phi}_{w0}|/\bar{\phi}_{w0} = 0.30$ (Figure 3.9).

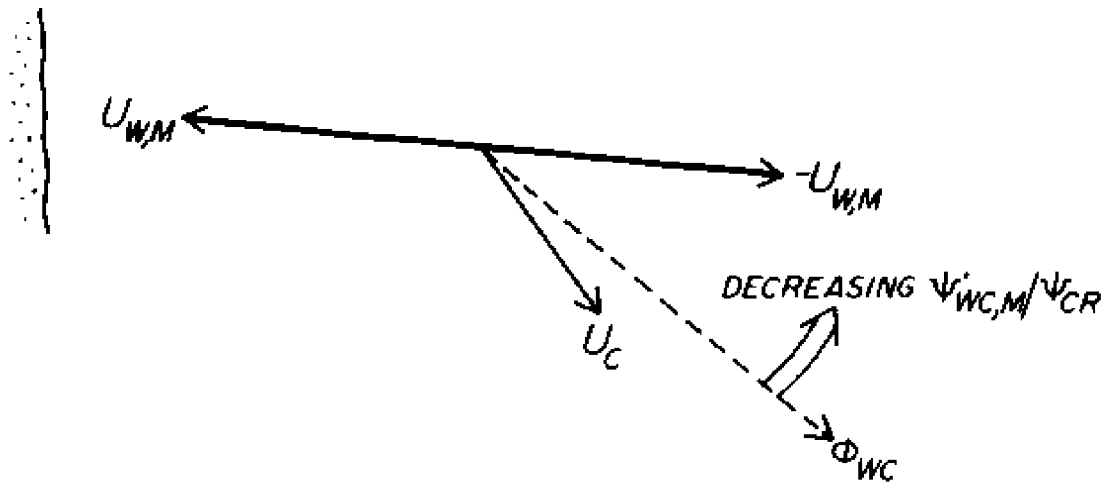
The mean current set to the south and offshore, and the waves propagated normal to shore (Figures 3.6 and 3.7). The threshold effect significantly augmented the offshore component of the net transport; shown in Figure 4.4 is a schematic of the threshold-induced rotation of net transport in relation to the mean current and symmetrical wave-orbital velocity. $\hat{\phi}_{w0}$ was directed to the south and offshore, and was rotated offshore relative to \hat{U}_c (i.e. ζ was negative) due to the threshold-induced asymmetry in the instantaneous transport rate. After 2.5 hours (event duration), the offshore component of $\hat{\phi}_{w0}$ was 170.5% of the offshore component of $\hat{\phi}_c$, which corresponded to $\zeta = -40^\circ$ (Figure 4.4).

4.3.2 Cross-shore gradient in transport

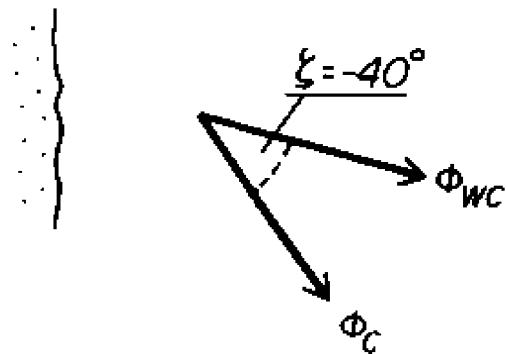
The cross-shore variation in mean-current velocity associated with event A is unknown. The simplest solution to this problem is as follows: assume the mean-current field is uniform, i.e. the mean current at every point on the shoreface is given by the observed mean current at 17.5-m depth. This assumption is not untenable. Given that

Figure 4.4 Offshore transport: event A, mid-shoreface. Schematic of threshold-induced rotation of net transport in relation to mean current and symmetrical wave-orbital velocity. After 2.5 hours (event duration), cumulative net transport was turned offshore 40° by the threshold-induced asymmetry in the instantaneous transport rate.

OFFSHORE TRANSPORT



EVENT A - AFTER 2.5 HOURS



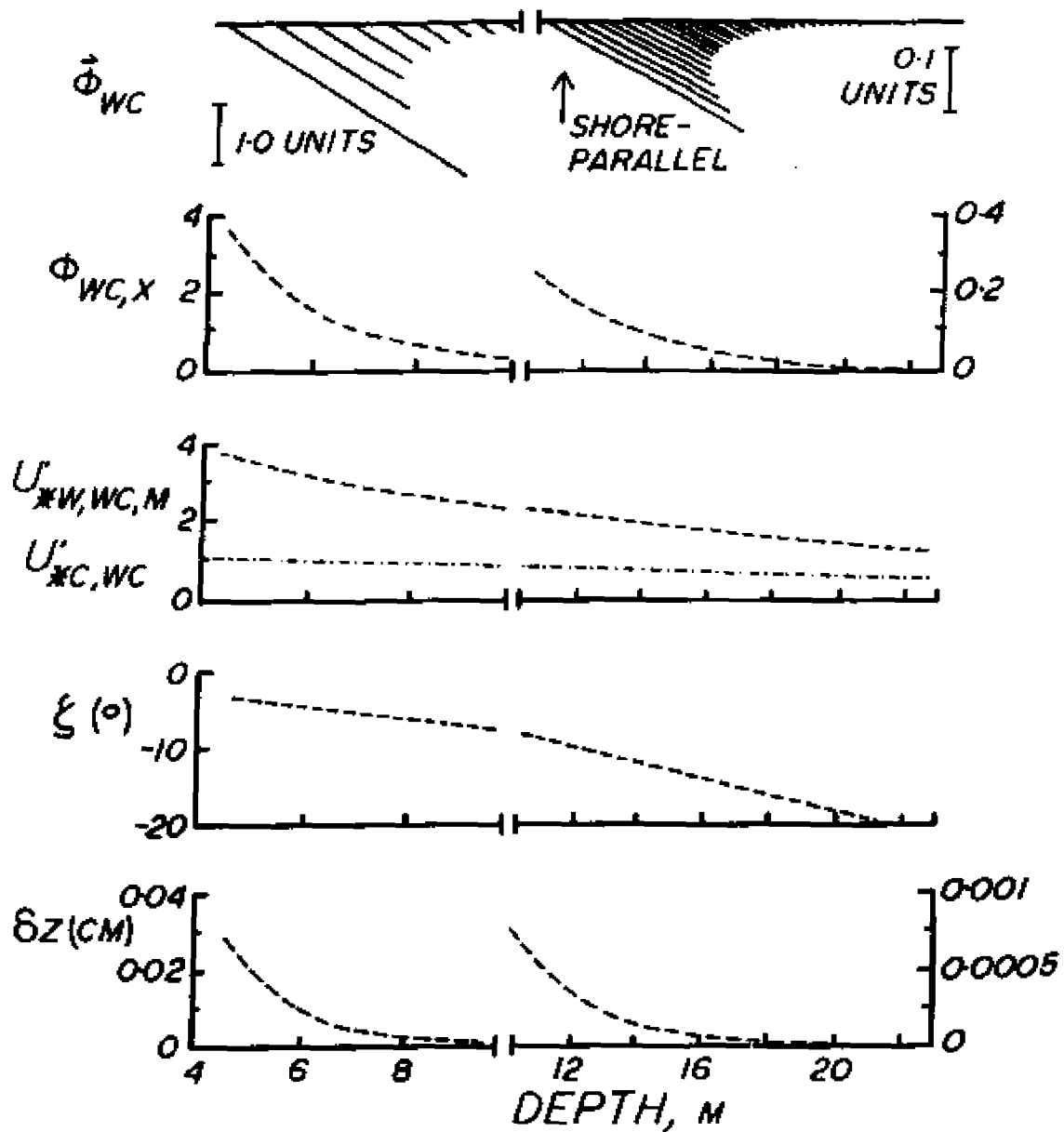
observed $U_{1/10}$ was twice the magnitude of U_{100} at 17.5-m depth (which will be reproduced by the initial model conditions), and that the cross-shore rate of change of $U_{w,m}$ (which is reproduced by the wave transformation model) is likely to exceed that of U_c , then errors in the assumed magnitude of the inshore tidal-current velocity will translate only into relatively smaller errors in $U_{w,m}/U_c$, which ratio is the important control on the bed shear stress and bedload flux. However, the assumption of uniform direction may be violated by a progressive turning of the current vector towards alignment with the shoreline as the depth decreases, this to satisfy the boundary condition imposed by the coastline. This possibility is addressed during the discussion of the model predictions.

The initial model conditions chosen to represent event A were as follows: $T = 8.83$ s (observed average peak spectral period) and deepwater wave height and direction = 0.88 m and 250° (i.e. propagating normal to shore) respectively. These initial conditions were chosen such that the predicted wave parameters at 17.5-m depth coincided with observed values. The mean-current velocity at every point on the shoreface was set equal to the observed mean-current velocity at 17.5-m depth (13.7 cm/s at 100 cm above the bed, directed to 135° , i.e. to the south and offshore). Shown in Figure 4.5 are the predicted cross-shore distributions of: $\hat{\phi}_{wc}$; $\hat{\phi}_{wc,x}$; $U_{*w,wc,m}^2$ and $U_{*c,wc}^2$; ζ ; and δz , where $\hat{\phi}_{wc}$ was calculated assuming symmetrical wave-orbital velocity.

Both the magnitude and direction of the predicted bedload flux changed with depth across the shoreface. The increase in magnitude with decreasing depth was driven by increases in $U_{*w,wc,m}^2$ and, to a lesser extent, $U_{*c,wc}^2$. Net bedload transport was directed south and offshore

Figure 4.5 Offshore transport, symmetrical wave-orbital velocity: event A. Predicted cross-shore distributions of: $\hat{\phi}_{wc}$; $\phi_{wc,x}$; $U_{*w,wc,m}^1$ and $U_{*c,wc}^1$; ζ ; and δz .

EVENT A - SYMMETRIC WAVE



at every point on the profile. As the ratio $\psi'_{w0,m}/\psi_{cr}$ increased approaching shore, $\hat{\phi}_{w0}$ turned onshore in the direction of \hat{U}'_c ; ζ increased from -20° at 22-m depth to -4° at 4-m depth.

As was the case previously, the cross-shore changes in magnitude and direction of $\hat{\phi}_{w0}$ drove changes in $\phi_{w0,x}$ that were opposite in sense. The resulting sediment-flux divergence in this case though is opposite that associated with onshore transport. The increasing magnitude of $\hat{\phi}_{w0}$ caused a shoreward increase in $\phi_{w0,x}$, while the rotation of $\hat{\phi}_{w0}$ caused the opposite. Negative sediment-flux divergence (accretion) at every point on the shoreface is defined by the former; positive divergence (erosion) by the latter. Again, bed shear stress was the dominant control: the predicted outcome was seaward-directed transport and accretion at every point on the profile, with the local rate of accretion increasing approaching shore (Figure 4.5). As was the case previously, the bedload-flux divergence must reverse sign to conserve sediment. Assuming the reversal occurs at some point on the shoreface dependent on the proportion of total load moving in suspension, then sediment eroded from the top of the shoreface is deposited across the bottom of the shoreface in deeper water, flattening the profile in the process (Figure 4.6).

4.3.3 Effect of wave asymmetry

The predicted cross-shore distributions of $\hat{\phi}_{w0}$, $\phi_{w0,x}$, $U'_{*w,w0,m}$, $U'_{*c,w0}$ and δz are shown in Figure 4.7, where the net transport was calculated by incorporating the expression for the asymmetric wave-orbital velocity. The salient feature of the model predictions is the

Figure 4.6 The proportion (numbers in A) of total sediment flux advected alongshore as suspended load increases shoreward. The cross-shore component of total flux, directed offshore as bedload, therefore varies as in B. The profile response (C) is given by the derivative of the curve in B: the profile is flattened as sediment is eroded from the top of the shoreface and deposited in deeper water.

OFFSHORE TRANSPORT

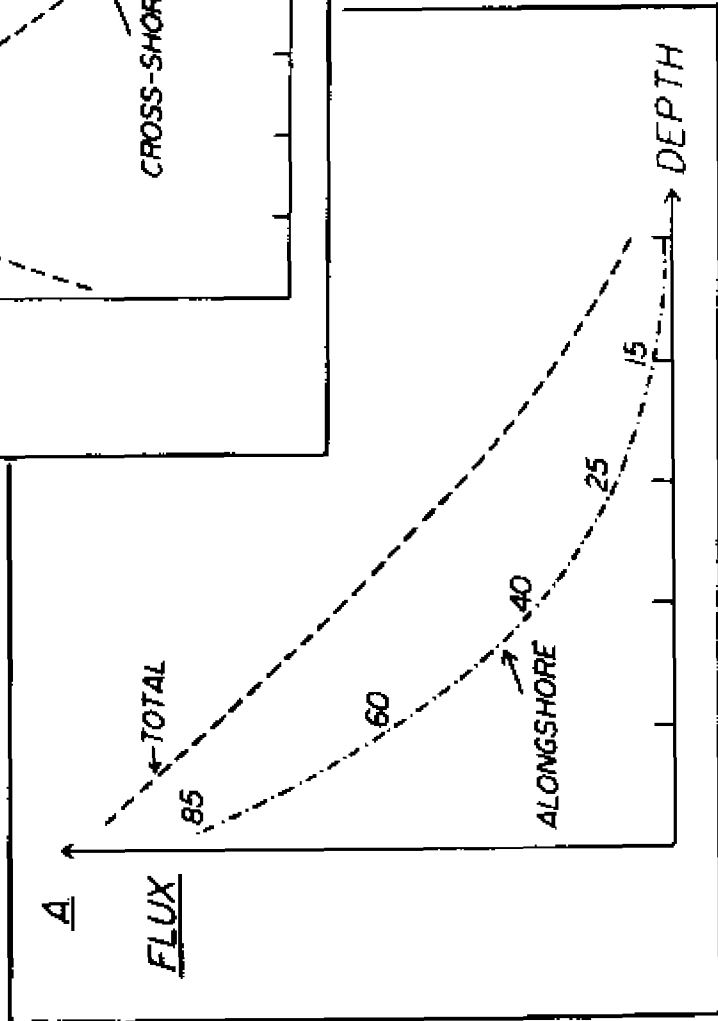
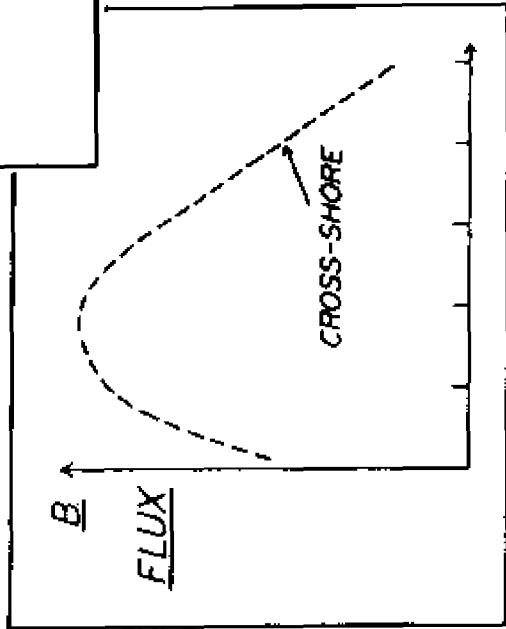
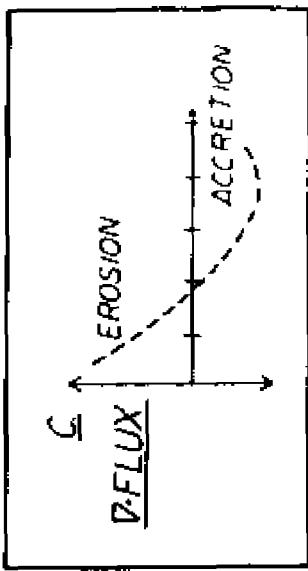
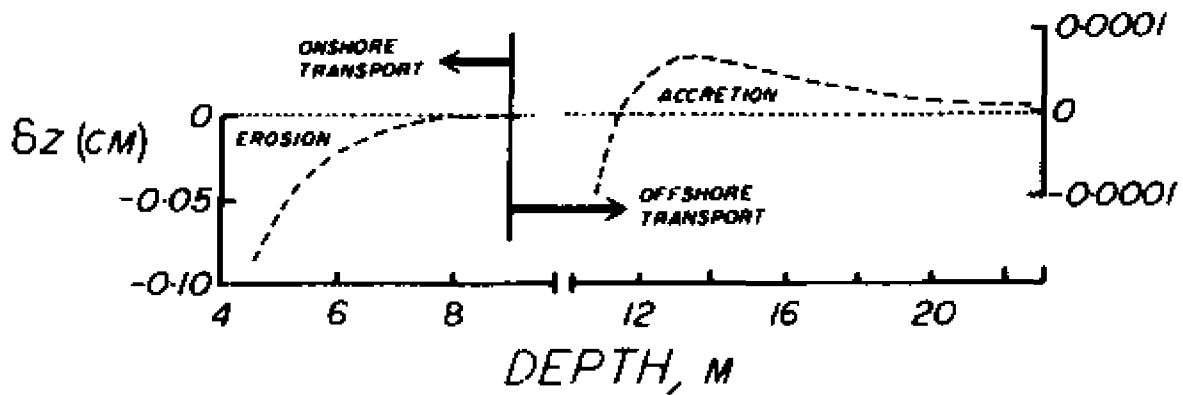
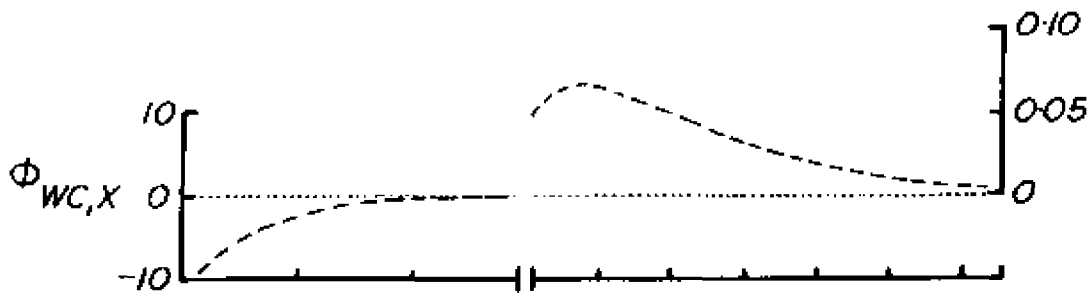
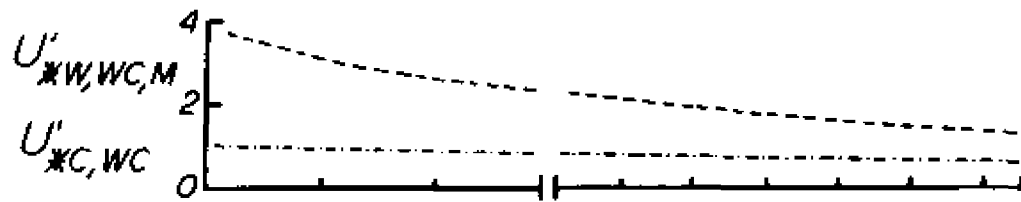
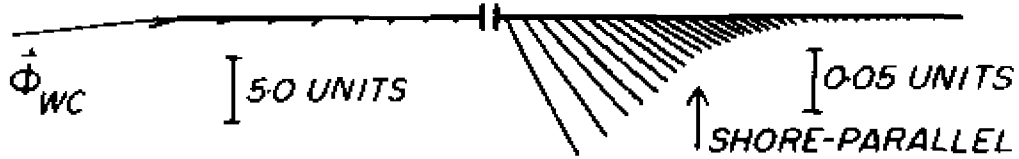


Figure 4.7 Offshore transport, skewed wave-orbital velocity:
 event A. Predicted cross-shore distributions of:
 $\hat{\phi}_{wc}$; $\phi_{wc,x}$; $U_{*w,wc,m}^*$ and $U_{*c,wc}^*$; and δz .

EVENT A - SKEWED WAVE



effect of the skewed wave-orbital velocity on the rotation with depth of the net bedload-flux vector. Under the symmetrical wave, net transport was directed offshore, being constrained by the juxtaposition of the oscillatory and mean flow. The skewed wave-orbital velocities remove that constraint. Net transport rotated progressively onshore as the wave became increasingly skewed with decreasing depth; eventually $\hat{\phi}_{wc}$ turned onshore of \hat{U}_o , and, shorewards of 9.5-m depth, net transport was directed onshore. At 11.5-m depth, bedload-flux divergence changed sign; seaward of 11.5-m depth, divergence was positive (accretion), and shoreward, divergence was negative (erosion). The change in sign that both $\phi_{wc,x}$ and $\partial\phi_{wc,x}/\partial x$ undergo does not (and can not) occur at the same depth. Hence, sediment eroded between 9.5-m depth and 11.5-m depth was deposited seaward of 11.5-m depth. Between 9.5-m depth and the top of the shoreface, predicted shoreward-directed transport increased without limit (Figure 4.7), which is reconciled by assuming, as before, a reversal in the bedload-flux divergence, either at the breakpoint or at some point on the upper shoreface.

Thus, as depth decreased and the wave component of the combined flow became increasingly skewed, the mean current relinquished dominant control over the cross-shore gradient in bedload flux. At the base of the profile, where wave asymmetry was not pronounced, the profile was flattened under the dominant influence of the mean flow; in shallower depths, the profile was steepened under the influence of wave asymmetry.

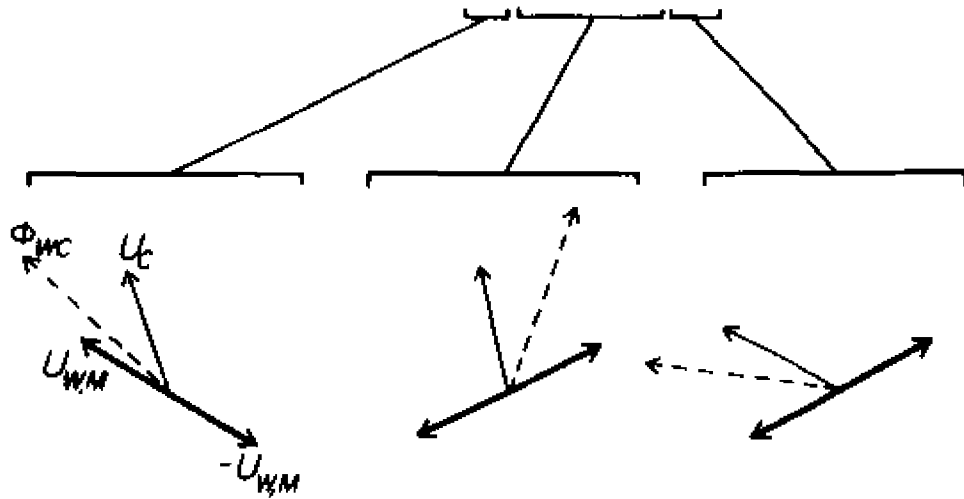
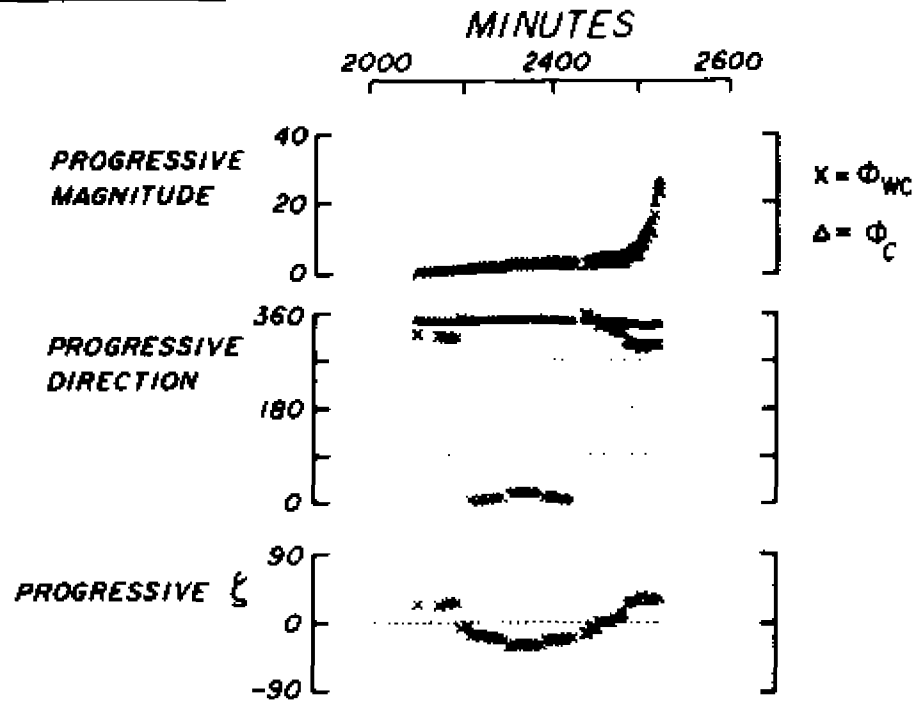
4.4 Variable Wave Direction

Shortly into the ebbing tide that began near 1600 hours on August 17, the semi-diurnal rotation of the mean current that had persisted for the first half of the mid-shoreface (17.5-m depth) experiment ceased (Figure 3.6). Thus was presaged the second event observed during the 17.5-m depth deployment. Event B, which began near 0100 hours 18 August, is marked as such on Figures 3.6, 3.7 and 3.9. Critical stress was exceeded for a total of 9.2 hours through, and presumably some time beyond, the termination of the experiment. Event B was initiated by simultaneous increases in U_{100} and $U_{1/10}$: U_{100} increased to an average (over the event) of -10 cm/s and $U_{1/10}$ to -20 cm/s. Peak spectral period inferred from the measured near-bed velocities was 8 to 9 s, which is in agreement with the peak spectral period reported from the nearby waverider: 8.83 s at 0100 18 August, and 8.01 s at 0700 18 August (CERC, 1983). Significant wave heights at those times, recorded by the same waverider, were 0.54 m and 0.53 m.

The mean current set north and onshore over the duration of the event (Figures 3.6 and 3.7). Three shifts in relative wave and current direction affected the direction of net sediment transport. Refer to Figure 4.8 for schematics of the following description, in which $\hat{\phi}_{wc}$ was calculated assuming symmetrical wave-orbital velocity and where $\hat{\phi}_c$ has the magnitude of $\hat{\phi}_{wc}$ and the direction of \hat{U}_c . Early in the event, waves propagated north of shore-normal and the acute angle between the wave and mean current opened onshore; $\hat{\phi}_{wc}$ thus was rotated shorewards of \hat{U}_c and the onshore component of net transport was enhanced. After ~1.5 hours, wave direction changed, and for the next 4.5 hours, waves

Figure 4.8 Event B, mid-shoreface (17.5-m depth) experiment. Progressive magnitude and direction of $\hat{\phi}_{WC}$ and $\hat{\phi}_C$ over the duration of the event, where $\hat{\phi}_{WC}$ was calculated assuming symmetrical wave-orbital velocity. Also shown is the progressive angle of rotation (ζ) and schematics, applicable to the three relative orientations of the wave and current discussed in the text, of the threshold-induced rotation of net transport in relation to mean current and symmetrical wave orbital velocity.

EVENT B



propagated south of shore-normal. The acute angle now opened seawards, and the offshore component of net transport was enhanced.

Accompanying the increase in magnitude of $\hat{\phi}_{WC}$ that occurred towards the end of the experiment (Figure 3.9) was an onshore rotation of the mean-current vector, which re-established the relative orientation of the oscillatory and mean flow as it was during the first 1.5 hours of the experiment. After 9.2 hours, the onshore component of $\hat{\phi}_{WC}$ was 208% of the onshore component of $\hat{\phi}_0$, which corresponded to $\zeta = +39^\circ$.

The relative orientation of the two components of the total flow, rather than the direction of either single component, therefore controls the direction of net transport in low-energy conditions. The onshore component of the combined-flow transport is enhanced when the acute angle between the wave and mean current opens shoreward, and when the wave-orbital velocity is symmetrical or at least not greatly skewed. The reverse is true (i.e. offshore component is enhanced) when the acute angle opens seaward.

4.5. Discussion

Using a combined-flow boundary-layer dynamics model, long periods were identified when the fairweather flow was competent, i.e. capable of generating skin friction that exceeded that necessary to initiate sediment movement. The oscillatory component of the competent combined flow generated greater than 80% of the total skin friction. However, given the high power-dependence of transport on stress, especially at low transport rates, the minor contribution made by the mean flow to the total skin friction is still important in terms of sediment transport.

Since the observed competent wave heights at 17.5-m and 22-m depth (0.50 to 0.80 m) were less than the annual average wave height at 18.5-m depth (0.88 m; Birkemeier et al., 1985), it is likely that the entire shoreface, extending from the breakpoint to the inner shelf, is active for a significant part of the year.

The four fairweather events that were observed are representative of two different kinds. The first kind (event A) was characterized by a short-lived increase in wave height that coincided with an ebbing tidal current. Unless the increase in wave height that initiated the event was linked causally to the adverse mean flow, which seems unlikely since this was not observed during other times of adverse mean current, then the wave height increase was transient, coincidentally occurring on an ebbing tide. The second type of event, represented by events B, C and D, was characterized by a steady mean flow that suppressed the semi-diurnal tidal-current rotation. The persistence of the steady flow is indicative of a coherent mean-flow field of possible broad spatial extent and complex structure. Subtidal (i.e. of a frequency lower than semi-diurnal) currents in the Mid-Atlantic Bight are usually energetic and driven by storm winds (e.g. Beardsley and Bolcourt, 1981); the fairweather mean flow associated with events B, C and D was neither high-energy (compared to typical storm-current velocities reported in the literature) nor was it correlated with high winds. The observed mean flow may have been driven by a baroclinic pressure gradient; density stratification is a common feature of Mid-Atlantic Bight shelf waters during summer. In any case, fairweather competent currents may be represented by subtidal mean-current fields that span the entire

width of the shoreface and that were previously thought to be characteristic only of storms.

The observed competent fairweather wave-orbital velocities ($U_{1/10} = 20$ to 24 cm/s, associated with wave heights of 50 to 80 cm and wave periods of 7 to 14 s) and mean-current speeds (10 to 14 cm/s) were significantly less energetic than the velocities associated with storm conditions that the shoreface experiences episodically throughout the year. For example, Wright et al. (1986) reported a significant wave height of 2.10 m and maximum wave heights in excess of 3 m in 8-m water depth associated with an early fall "northeaster" storm (mid-latitude cyclone) of 3.5-days duration. The storm wave-orbital velocities at 20 cm above the bed exceeded 150 cm/s, and the mean current speed at the same elevation was 33 cm/s (which would have been substantially higher at $z = 100$ cm, the reference elevation used herein). Thus, fairweather flow is capable of transporting sediment at rates that are orders of magnitude smaller than storm flows are capable of. However, in terms of the relative contribution of low-energy flow to the long-term (years or longer) sediment budget of the shoreface, higher frequency of occurrence of low-energy competent flow may offset lower transport rates. In any case, if the assumption of longshore uniformity of the shoreface and the shoreface flow field holds, then the total sediment flux is irrelevant to an understanding of profile change, for it is the spatial derivative of the cross-shore component of the total flux that controls the profile evolution (i.e. migration or change of shape).

Sediment-flux divergence was examined in terms of the cross-shore variation in magnitude and direction of net transport. The magnitude of $\hat{\phi}_{wc}$ increased approaching shore, driven primarily by the shoreward

increase in the oscillatory component of the total skin friction. Several factors were identified that exerted varying degrees of control on the direction of sediment transport: the juxtaposition of the mean and oscillatory components of the combined flow, the degree of wave asymmetry, the critical bed shear stress, and the intensity of near-bed flow, all of which may vary with depth or distance offshore. The threshold-induced asymmetry in the instantaneous transport rate that caused rotation of the net transport vector is significant only when sediment is not in motion over the whole wave period. Vincent et al. (1983) speculated that this rotation was a high-energy phenomenon and that the rotation enhanced onshore transport. Both of these speculations are contrary to the results of the present analysis: firstly, it was shown that the rotation of $\hat{\phi}_{wc}$ relative to \hat{U}_c approaches zero as the ratio $\psi'_{wc,m}/\psi_{cr}$ increases, and secondly, offshore transport is enhanced if the acute angle between the wave and current opens seaward.

Suspended-sediment transport may play an important role in the profile adjustment to competent flow. If suspended load accounts for an increasing proportion of the total load approaching shore, and the total load has a shore-parallel component of motion, then the spatial derivative of the cross-shore component of bedload-flux is restrained from either increasing or decreasing without limit. In this way, sediment conservation is preserved; sediment transported onshore as bedload is deposited at the top of the shoreface, and sediment that is transported offshore as bedload is deposited at the base of the shoreface, both of which are intuitively reasonable.

In summary, two scenarios characterize fairweather bedload transport of sediment on the shoreface by combined wave and current flow:

- (1) The acute angle between the mean component and the oscillatory component of the total flow opens shoreward. Net bedload transport is directed onshore at all depths and the onshore component of transport is enhanced by the threshold-induced asymmetry in the instantaneous transport rate and by the skewed wave-orbital velocity. Sediment eroded from the base of the shoreface is transported shoreward and deposited at the top of the shoreface, thus steepening the shoreface profile.
- (2) The acute angle between the mean component and the oscillatory component of the total flow opens seaward. At the seaward base of the shoreface, where wave asymmetry is not pronounced, net bedload transport is offshore and the shoreface profile is flattened under the dominant control of the mean flow. At some depth that is dependent on the wave conditions, net transport is turned onshore relative to the mean flow by the asymmetry of the wave-orbital velocity. Shoreward of this depth, sediment is transported onshore under the dominant control of the skewed oscillatory flow to be deposited at the top of the shoreface.

Actual observations of shoreface erosion and accretion under fairweather waves and currents are used in the next chapter to assess and verify the predicted shoreface profile response to onshore and offshore sediment transport.

5. OBSERVED SHOREFACE RESPONSE TO LOW-ENERGY COMPETENT FLOW

5.1 Methodology and Data Analysis

The field experiment conducted over the period 6-16 September, 1985, was designed to measure bed response to fairweather waves and currents over an extended period. Observations were made in a water depth of 8 m at the top of the shoreface (Figure 3.5). On 11 September, 4.5 days from the beginning of the experiment, there occurred a "northeaster" storm which was accompanied by high waves and a strong downwelling. Only the 4.5 days of fairweather observations prior to the storm are described herein; see Wright et al. (1986) for a description of bed response to the storm conditions.

A Sea-Data Model 635-9RS directional wave and current meter was mounted on a weighted tripod and set on the seabed at the 8-m depth site. The Sea-Data instrument incorporated a ParoScientific quartz pressure sensor and a 4.0-cm diameter, 2-axis Marsh-McBirney electromagnetic current meter. A Datasonics Model ASA-920 digital sonar altimeter (DSA), mounted on a nearby separate platform supported by pipes driven into the seabed, was also interfaced to the Sea-Data logger. The DSA is a short-range (0.5 to 5 m), high-resolution sonar device configured to measure relative changes in bed elevation at a single point. The time between transmission of a high-frequency (4.5 MHz) acoustic pulse and receipt of an echo from the seabed is measured

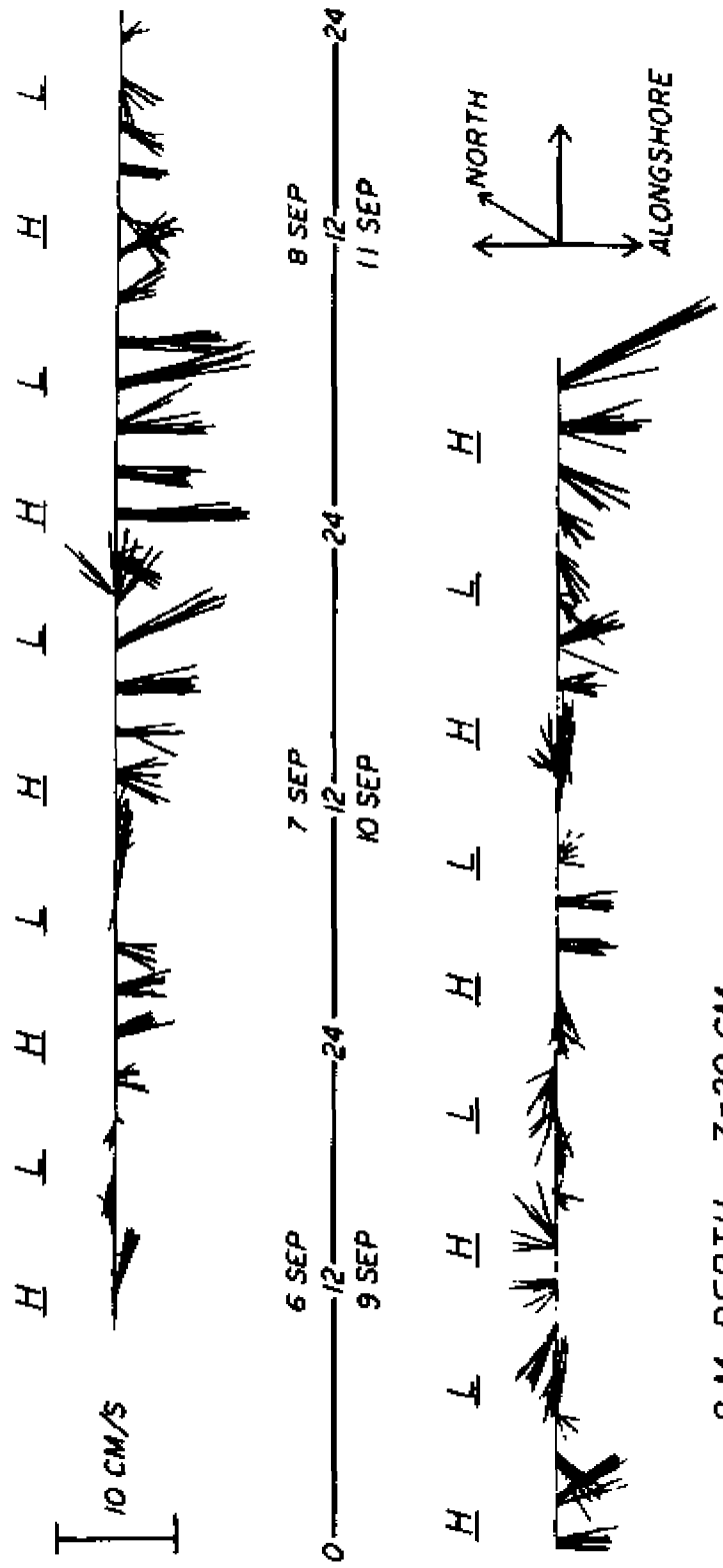
by a solid-state timer and converted to a digital number that is proportional to the distance between the transducer and the seabed. A calibration curve that enabled conversion of the measured time into distance of the transducer above the seabed was derived in the laboratory prior to and at the conclusion of the experiment; see Green and Boon (1987) for a complete description of the calibration procedure and verification of the long-term stability of the instrument.

The Sea-Data unit controlled a burst-sampling sequence; each burst was 2048-s long, and a burst was begun every 2 hours. Pressure and current sensors were sampled every second, and the sonar altimeter every 8 s. The current meter and the DSA, which was located 6 m from the main tripod, were set at nominal elevations of 20 cm and 50 cm above the bed respectively. The current-meter elevation and orientation, and the elevation of the DSA above the bed were verified periodically by divers.

Sediment at the site was very well-sorted fine sand (mean diameter 0.13 mm) with a silt and clay content of less than 2%. Symmetrical wave-generated ripples, 3-cm high by 15-cm long, covered the bed.

The vector-averaged (over blocks of 512 s) current velocity during the fairweather period of the experiment is shown in Figure 5.1, together with predicted times of high and low water at Kitty Hawk. The wind was light to moderate (<21 km/hr) and primarily from the southwest to southeast over the entire pre-storm period, except for a short interval of light northerly breezes on the second day. The waves were low (<60 cm at the 18.5-m depth waverider) and long (10 s) throughout. The total skin friction exerted by the wave and current in nonlinear combination, calculated as described in Chapter 3, exceeded the critical stress for the 0.13-mm diameter sediment (0.080; Madsen and Grant, 1976)

Figure 5.1 Overview of the fairweather portion of the upper-shoreface (8-m depth) experiment. Shown are the vector-averaged (over blocks of 512 s) current velocities ($z = 20$ cm) and times of predicted high ("H") and low ("L") water. The experiment began at 1300 hours, 6 September. 4.5 days later, near midnight on 11 September, the storm reported by Wright et al. (1986) began.



8-M DEPTH, Z=20 CM

for almost the entire duration of the experiment (Figure 5.2). Thus, sediment at 8-m depth on the shoreface was in motion virtually continuously throughout the 4.5-day fairweather period. During this time, the mean-current vector (average magnitude ~6 cm/s) rotated at the semi-diurnal tidal frequency, with the exception of one interval when the mean current set alongshore to the south for approximately 24 consecutive hours (Figure 5.1).

Two statistical measures are used in the following analysis to demonstrate the mean-flow and wind-wave-asymmetry controls on direction of net bedload transport at the 8-m site. The nondimensional skewness, S_k , of the shore-normal component of flow is defined by:

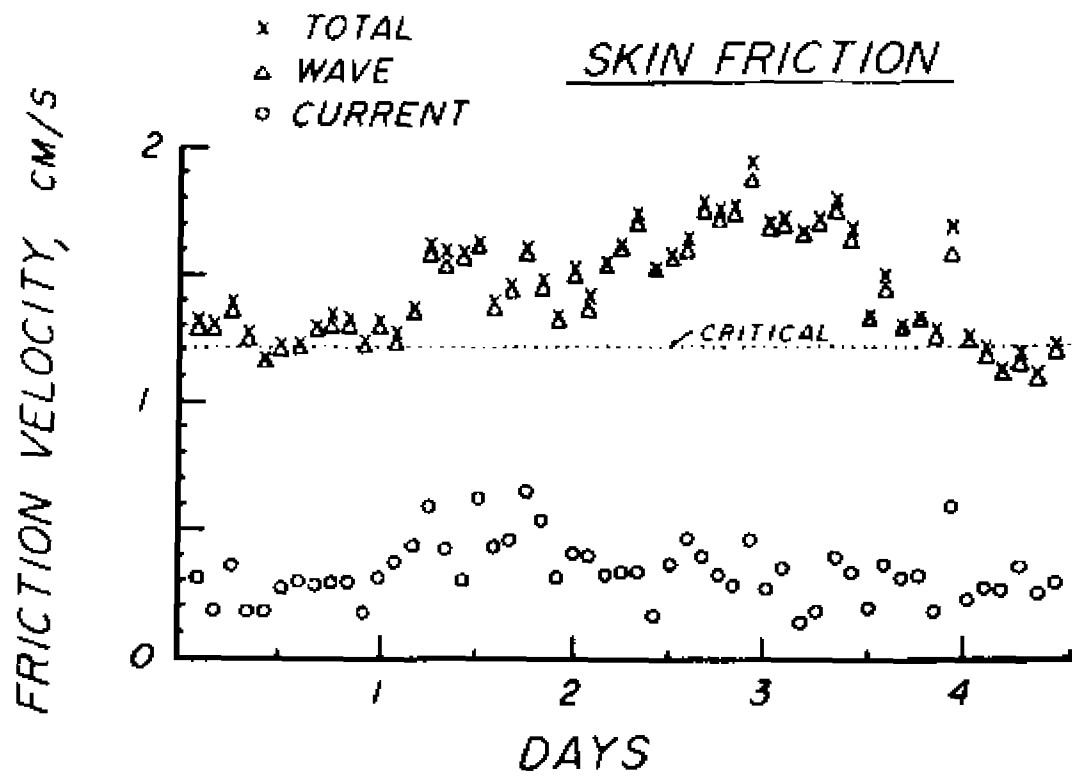
$$S_k = (1/n) \sum_{i=1}^n (u_i - \bar{u})^3 / \left[(1/n) \sum_{i=1}^n (u_i - \bar{u})^2 \right]^{3/2} \quad (5.1)$$

where u_i is the shore-normal component of the i th velocity observation, \bar{u} is the mean shore-normal component of flow, and n is the number of observations. Since the mean flow is removed from each u_i , S_k represents the skewness of the wave-orbital velocities only. The mean cube of the shore-normal component of flow, \bar{u}^3 , also nondimensionalized by the variance (raised to the power 1.5), and defined as:

$$\bar{u}^3 = (1/n) \sum_{i=1}^n (u_i)^3 / \left[(1/n) \sum_{i=1}^n (u_i - \bar{u})^2 \right]^{3/2} \quad (5.2)$$

is an indicator of net transport direction. Positive \bar{u}^3 (i.e. higher than Gaussian frequency of positive velocities) indicates offshore transport, and negative \bar{u}^3 indicates onshore transport. Furthermore,

Figure 5.2 Total skin friction, wave component of the total skin friction, and current component of the total skin friction, all expressed as friction velocities (units of cm/s). Calculated from burst-averaged flow parameters at 8-m depth. The critical skin friction for the 0.13-mm diameter sediment is also shown. The time axis is days from beginning of the experiment (1300 hours, 6 September, 1985).



since the mean flow is not removed from each u_i as it is in the calculation of S_k , both the mean-flow control and wave-skewness control on transport direction are contained in \bar{u}^3 .

S_k was calculated from equation 5.1 and \bar{u}^3 from equation 5.2, where the series length was set equal to the number of observations in a single burst (i.e. $n = 2048$), and u_i was defined as the shore-normal component of the observed velocity at the 8-m site. The calculated values of S_k , \bar{u}^3 and \bar{u} are shown in Figure 5.3.

S_k was consistently negative, which indicates a higher than Gaussian frequency of large negative (onshore) velocities. Since the mean flow was removed from each u_i in the calculation of S_k , the observed negative values of S_k are due to asymmetric wave-orbital velocities, skewed onshore in the direction of wave propagation. Divided opinion exists as to the ability of electromagnetic current meters to measure high-order velocity moments such as skewness. Hamblin et al. (1987) concluded that "the quantitative use of higher-order velocity moments for sediment transport measured from such a system [i.e. electromagnetic current meters] would lead to unacceptably large errors" (p. 11,872), however their analysis was based on a comparison of data from widely separated (kilometers) stations in a shallow lake, which must cast doubt on their conclusions. Doering and Bowen (1987), on the other hand, compared data from co-located current meters and pressure sensors and concluded that "the Marsh-McBirney current meter appears to be a suitable sensor to use for the estimation of normalized velocity moments" (p.13,183). It is noted here that the observed velocity skewness at the 8-m site was consistent with that expected from theory (viz. wave-orbital velocities skewed in the direction of wave

Figure 5.3 Nondimensional skewness of the shore-normal component of flow (S_k), nondimensional mean cube of the shore-normal component of flow (\bar{u}^3), and mean shore-normal component of flow (\bar{u}), 8-m depth, $z = 20$ cm. The time axis is days from the beginning of the experiment (1300 hours, 6 September, 1985).

\bar{U} CM/S

10
5
0
-5

$-\bar{U}^3$
 ΔS_K

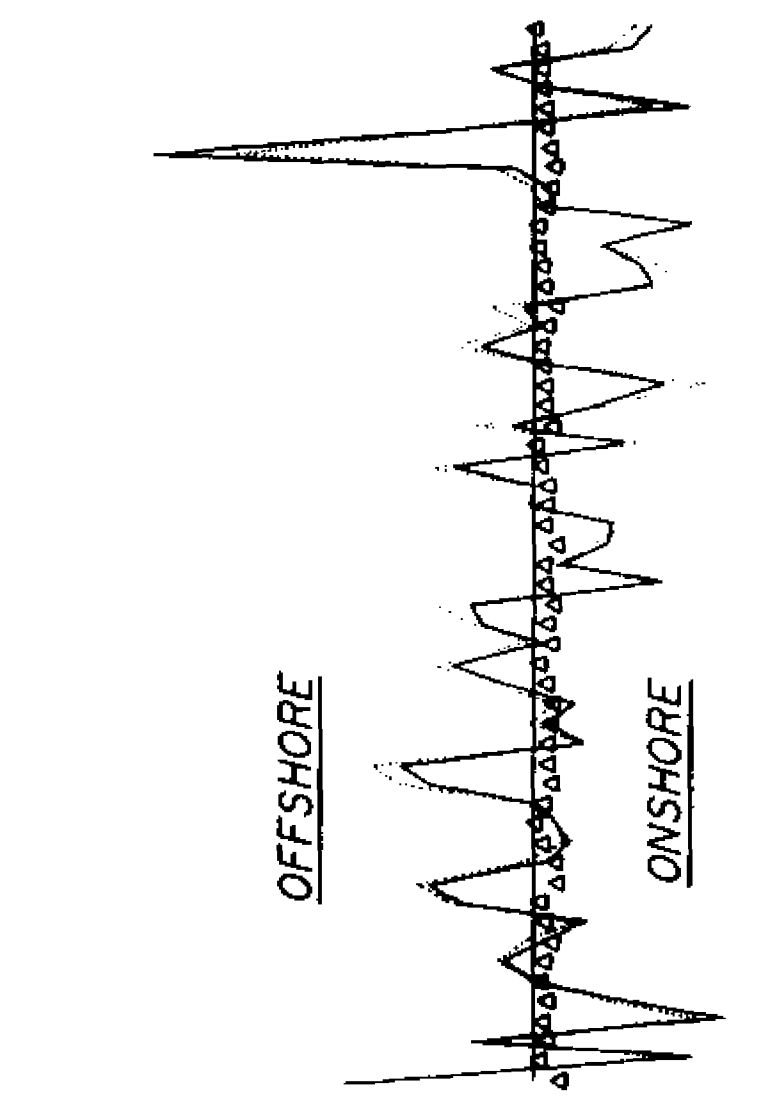
3
2
1
0
-1

OFFSHORE

ONSHORE

1 2 3 4

DAYS



propagation).

The mean cross-shore flow changed sign (i.e reversed) as the tidal flow rotated. The sign of \bar{u}^2 , and therefore the direction of cross-shore transport, followed the sign of \bar{u} almost exactly (Figure 5.3), indicating that it was the mean flow that controlled transport direction at this depth rather than the skewness of the wave-orbital velocities.

The sonar altimeter record, which is a record of the bed elevation relative to the fixed elevation of the transducer, was searched for intermittent spikes prior to analysis. A sample of the record is shown in Figure 5.4. Generally, the signal was characterized by a variation of 1 or 2 digital units (corresponding to a variation in relative bed elevation of ~0.30 cm) around what appears to be a base value (Figure 5.4.A). Two spikes of the kind that were removed from the record before further analysis are shown in Figure 5.4.B. The peak labelled "I" represents a temporary delay of echo detection and is presumably caused by scattering of the acoustic pulse by suspended particulate matter (sediment and organic debris). The peak labelled "II" represents a premature echo. This peak is wider than a single spike and therefore may represent an echo from a substantive feature, e.g. a transient but structured nepheloid layer.

The DSA record was averaged over each burst after all spikes were removed. The burst-averaged relative bed elevation over the fairweather period of the experiment is shown in Figure 5.5; over 4.5 days, relative bed elevation increased by a total of nearly 6 cm. It is likely that this represents accretion underneath the DSA, since the migration of wave ripples (the only bedforms observed at the site; see also the description of side-scan sonar imagery in section 3.2.1) underneath the

Figure 5.4 Two samples of DSA output from the low-energy period of the 8-m depth deployment.

A. The signal was generally characterized by a variation of 1 or 2 digital units (equivalent to a variation of -0.30 cm in relative bed elevation) around a base value.

B. The peak labelled "I" is due to pulse scattering, and the peak labelled "II" is due to a premature echo, possibly from a substantive feature. Both kinds of peak were removed from the record before averaging.

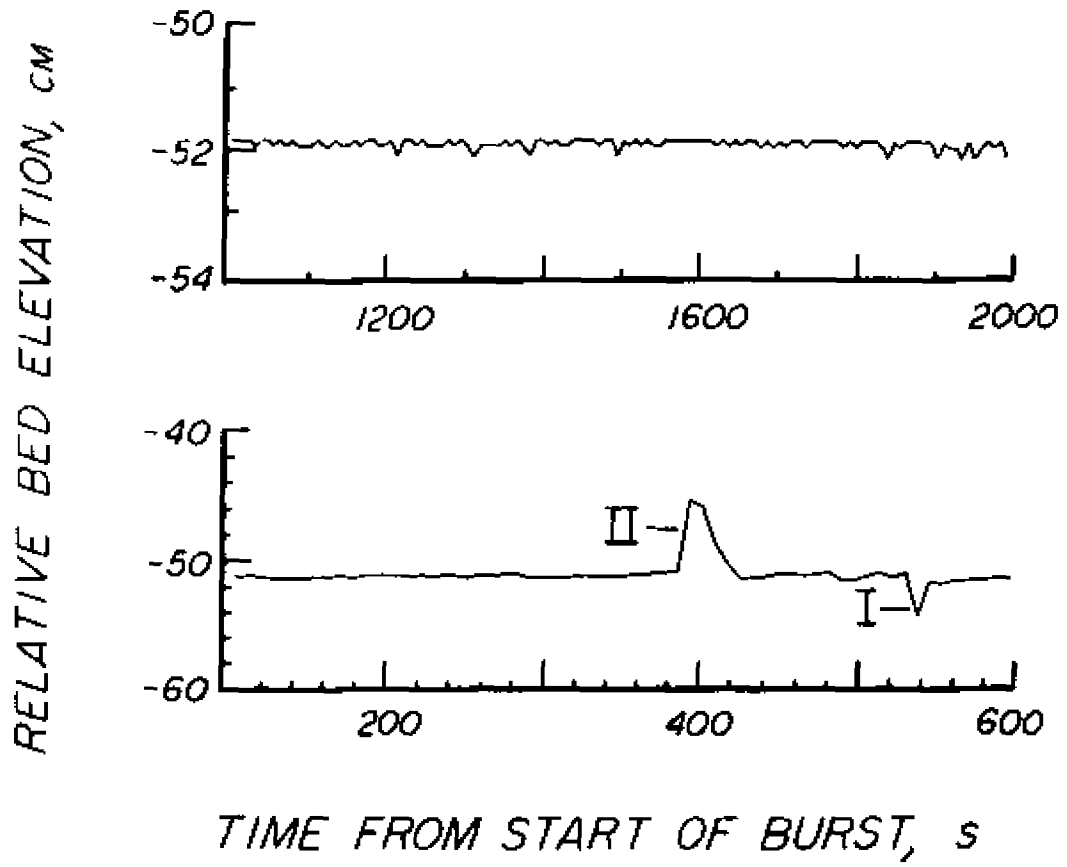
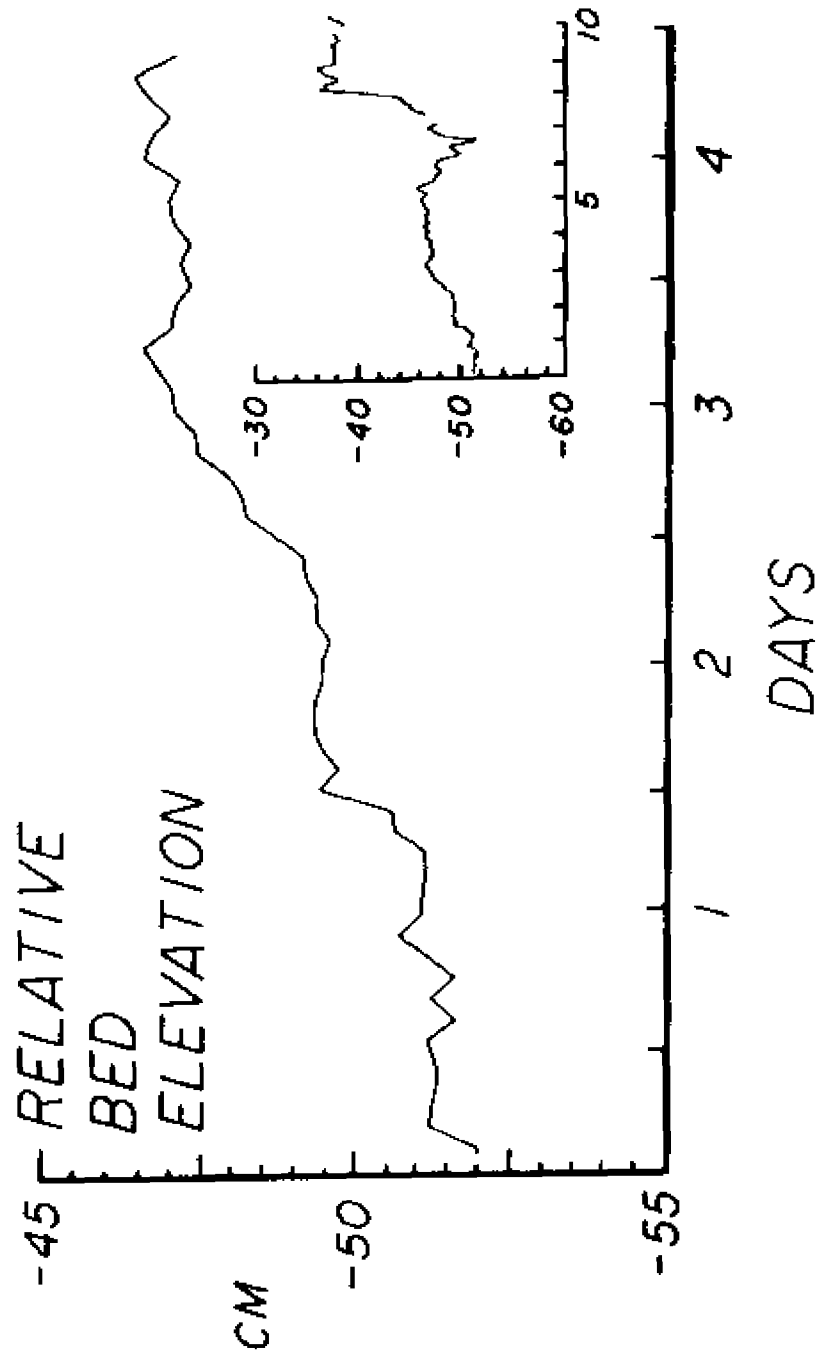


Figure 5.5 Burst-averaged bed elevation relative to the fixed elevation of the transducer; 8-m depth, fairweather. The transducer is at an arbitrary elevation of 0 cm. Also shown, as an inset, is the fairweather portion of the record and the erosional event reported by Wright et al. (1986), which began 4.5 days into the experiment. The time axis in both plots is days from the beginning of the experiment (1300 hours, 6 September, 1985).



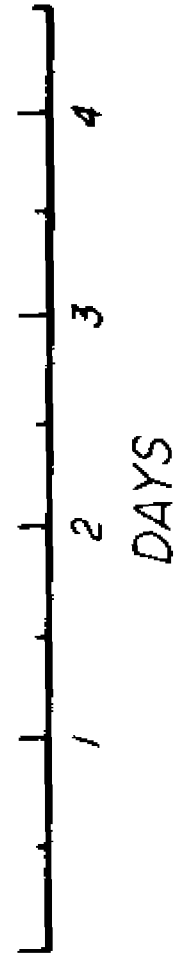
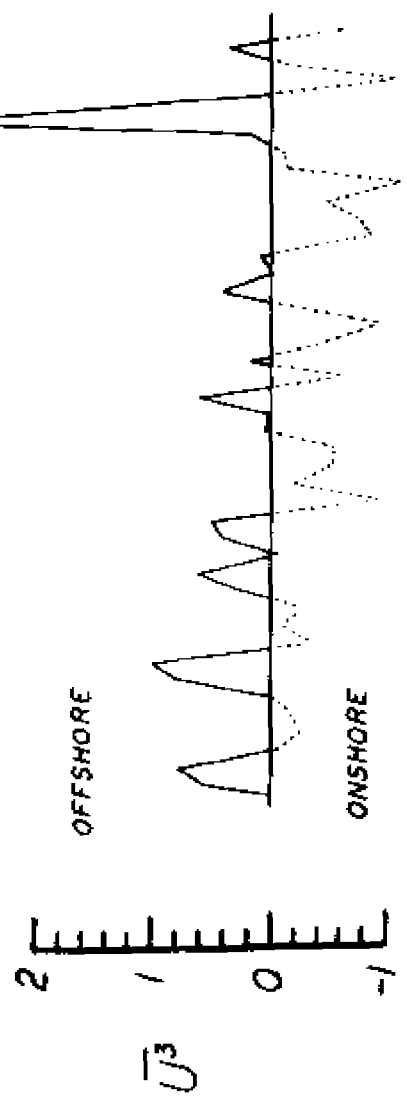
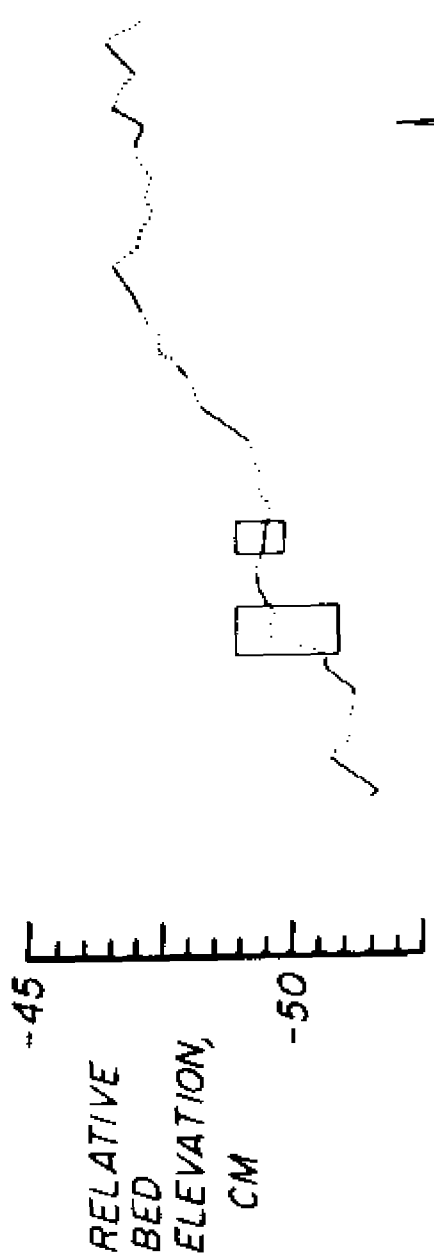
sensor could not have caused the observed monotonic increase in relative bed elevation. Furthermore, divers verified that accretion was not simply local, i.e. caused by the DSA obstructing the near-bed flow.

5.2 Discussion

The change in relative bed elevation and the mean cube of the shore-normal velocity component are shown together in Figure 5.6. Careful inspection of the data in Figure 5.6 reveals that the bed response associated with offshore transport (positive \bar{u}^3) is different to that associated with onshore transport (negative \bar{u}^3). With only one exception (noted in Figure 5.6), relatively rapid accretion occurred during periods of offshore transport. Also with only one exception (noted in Figure 5.6), erosion or relatively slow accretion occurred during periods of onshore transport. Therefore, it appears that the shoreface at 8-m depth responded in fundamentally different ways to offshore and onshore transport. The model simulations of onshore and offshore transport (Chapter 4) predict fundamentally different profile responses; the simulations are used in the following discussion to explain the 8-m depth observations.

Accretion under mean-flow-controlled seaward-directed transport is found to be consistent with the model simulation of offshore transport (section 4.3) if it is assumed that the 8-m site corresponds functionally to the shoreface seaward of 11.5-m depth in the simulation (see Figure 4.7). Both the sediment source supplying the observed accretion, and the predicted point where transport turns onshore under the dominant control of shoreward-skewed wave-orbital velocities, must

Figure 5.6 Burst-averaged bed elevation relative to the fixed elevation of the transducer (where the transducer is at an arbitrary elevation of 0 cm), and nondimensional mean cube of the shore-normal component of flow, where negative indicates onshore transport and positive indicates offshore transport. The two sections of record enclosed in rectangles indicate the two exceptions to the rule described in the text. The time axis is days from the beginning of the experiment (1300 hours, 6 September, 1985).



therefore be onshore of 8-m depth. In effect then, the cross-shore distribution of transport shown in Figure 4.7 is compressed and shifted up the shoreface. Hence, onshore transport of sediment into the beach sediment prism occurred over a far more restricted area than indicated by the model simulation.

Erosion under mean-flow-controlled onshore transport is consistent with the model simulation of onshore transport (see Figure 4.2). It is interesting to note that the slow rate of accretion (relative to that observed during periods of offshore transport) sometimes associated with the observed onshore transport is consistent with the prediction of gradual deposition across the top of the shoreface driven by a progressive increase in proportion of total load moving as bedload (see Figure 4.3).

6. CONCLUSIONS

The observations of currents and model calculations of bedload transport provide a mechanistic basis for the fairweather transit of sediments across the shoreface. Magnitude and direction of sediment transport, cross-shore gradients in bedload flux, and associated shoreface profile response to fairweather waves and currents were examined using combined-flow boundary-layer and bedload-transport models. The objective was to understand the flow parameters governing bedload flux and flux divergence, where those parameters are the first three moments of the combined-flow velocity distribution (mean flow, wind-wave energy and wind-wave asymmetry respectively). Velocity data from two locations on the shoreface were used to identify and characterize fairweather transport events, and those observations were used to guide the model simulations.

Two fundamentally different types of event were observed. The first was of short duration (less than half a tidal period) and was initiated by an increase in wave height that coincided with an ebbing tide. The second, of which several instances were observed, spanned several tidal periods and was characterized by steady and unidirectional (alongshore to the south) mean flow that suppressed the semi-diurnal rotation of the tidal current. This seems indicative of a complex mean-current field of the type that is usually high-energy and wind-driven. However, each event of this type was low-energy (relative to reported

storm currents) and occurred during a period of light sea-breezes. The mean flow may have been driven by a baroclinic pressure gradient, since water-column stratification is a common feature of Mid-Atlantic Bight shelf waters.

Four events of the second type were observed: one of >9 hours duration at 17.5-m depth; one of >10 hours duration followed after a hiatus of ~4 hours by another of >9 hours duration at 22-m depth; and one of ~24 hours duration at 8-m depth. Shoreface flow, even in the deeper waters towards the inner shelf, may therefore be frequently competent. Over 4.5 days at 8-m depth on the upper shoreface, skin friction generated by fairweather waves and currents was in excess of critical stress virtually continuously. Hence, relatively low transporting capacity of competent fairweather flow may be compensated for in the long term by frequent occurrence.

The oscillatory component of the combined flow was generally twice the magnitude of the mean component and generated greater than 80% of the total skin friction. The mean flow should not be construed as insignificant though, firstly because the current acts to enhance the wave component of the total skin friction through nonlinear interactions in the boundary layer, and secondly because the highly nonlinear dependence of transport on stress means that even minor contributions to skin friction are important in terms of transport.

Direction of net bedload transport was controlled by several factors: the relative orientation of the oscillatory and mean components of the combined flow, the wave-orbital velocity asymmetry, and the threshold criterion. The threshold-induced asymmetry in the instantaneous combined-flow transport rate caused rotation of the net

transport vector when sediment was not in motion over the whole wave period (i.e. when the ratio $\psi'_{wc,m}/\psi_{cr}$ was small). This effect was significant on the lower shoreface where the flow was not intense and the wave orbital velocities were not greatly skewed. When the acute angle between the wave-orbital velocity and the mean flow opened seawards, the threshold-induced rotation enhanced the offshore component of transport, and vice versa. Enhancement of both offshore and onshore transport in this way was inferred from analysis of the velocity data.

Assuming the shoreface flow field is uniform in the longshore dimension, shoreface sedimentation is governed by the cross-shore gradient in bedload flux, which in turn is controlled by the cross-shore variation in both magnitude and direction of sediment flux. Approaching shore, the bedload-flux magnitude increases, driven primarily by an increase in the wave component of the total skin friction, and the net transport vector rotates in response to changes in the wave-orbital velocity asymmetry and the near-bed flow intensity.

Two scenarios, which are idealized but useful in a heuristic sense, emerged from the analysis of bedload-flux divergence. The first scenario was characterized by a seaward-opening acute angle between the wave and current. Net bedload transport was directed offshore at the base of the shoreface under the dominant influence of the mean flow, and onshore at the top of the shoreface under the dominant influence of shoreward-skewed wave-orbital velocities. The predicted depth where the transition occurred was approximately 10 m. The second scenario was characterized by a shoreward-opening acute angle between the wave and mean flow, and transport was directed onshore at every point on the profile. The two scenarios share an important common feature: onshore

transport over the upper shoreface (depths less than approximately 10 m) that increased in magnitude as the depth decreased. In both cases then, the bedload-flux divergence was positive over the upper shoreface, indicating a sediment source. The eroded sediment is deposited where the flux divergence changes sign; this could be at the shoreface-surfzone boundary, where a fundamental change in fluid motions occurs, or across the upper shoreface itself, if an increasing proportion of the total load is entrained as suspended load and advected parallel to shore with the mean flow.

The key prediction, common to both scenarios, was that fairweather shoreface sediment transport is characterized by upper-shoreface accretion under the dominant control of shoreward-skewed wave-orbital velocities. Observations of currents and changes in relative bed elevation over a 4.5-day period at 8-m depth were used to verify the simulated shoreface response to fairweather waves and currents. The mean flow controlled transport direction at 8-m depth, and the bed responded in fundamentally different ways to offshore and onshore transport. The observed bed response was consistent with the model simulations, with one important modification: the mean flow controlled the transport direction in depths shallower than predicted by the model simulations. Thus, onshore transport of sediment into the beach sediment prism by skewed wave-orbital velocities was restricted to a very limited range of depths (less than at most 8 m) immediately outside the surfzone when the mean flow set offshore. When the mean flow set onshore, sediment was transported into the surfzone from depths greater than at least 8 m. The mean flow is thus at least as an important

control as wind-wave asymmetry on transport direction, and therefore is a significant factor in sculpting the equilibrium shoreface profile.

The observed change in relative bed elevation at 8-m depth during five days of fairweather (-6 cm of accretion) was the same order as that observed during the subsequent 3.5-day duration storm (-5 cm of erosion followed by -10 cm of rapid accretion; Wright et al., 1986). Wright et al.'s conclusion, that "the amplitude of bed response over the mid shoreface to a typical northeaster [storm] may be appreciable" (p. 159), should thus be extended to apply also to fairweather conditions. The bed response to fairweather flow should vary with depth, being dependent on the near-bed flow intensity, the mean flow and the wave-orbital velocity asymmetry.

The model predictions and observations of upper-shoreface response to fairweather waves and currents are consistent with the concept, postulated by Niedoroda and Swift (1981) and Wright et al. (1984), of fairweather return of sediments from offshore to the beach prism. Sediment is exchanged between the surfzone and deeper waters offshore, and this exchange is bi-directional, with the shoreface acting at times as a conduit to the inner shelf, and at other times as a sediment sink or source. During fairweather, combined wave and current flow on the shoreface drives shoreward transport and sediment deposition at the top of shoreface. Thus, the beach sediment prism is nourished and replenished during the frequent periods of low-energy competent flow. Sediments, though, may not be returned consistently from very far down the shoreface, probably not from as far offshore as storms deposit sediments. Given no external sediment supply, and even in the absence of sea-level rise, a net offshore movement of sediment may therefore

occur causing landward migration of the shoreface and beach profiles. The long-term stability of beaches and the short-term post-storm recovery of beaches may thus be governed at least in part by those processes that control the fairweather sediment pathways between the shoreface and surfzone.

APPENDIX

A gravity wave propagating into shoaling water may experience a transformation in wave height due to the processes of shoaling, refraction and frictional dissipation. A wave also undergoes a wavelength transformation (predicted by linear theory) and a shape transformation (predicted by second and higher order wave theories). Given an initial wave height, period and angle of incidence and the bathymetric profile over which the wave is to propagate, equations that describe the various transformations can be used to predict the wave height and direction of propagation at every point on the profile.

Wave shoaling and refraction are expediently expressed (albeit with strictly limiting assumptions) using linear wave theory (e.g. Ippen, 1966). Change in wave height due to shoaling between outer depth h_1 and inner depth h_2 is given by:

$$K_s = H_2/H_1 = [C_{g(1)} / C_{g(2)}]^{0.5} \quad (\text{A.1})$$

where the subscripts 1 and 2 refer to the depths h_1 and h_2 respectively, and K_s is the shoaling coefficient. C_g is the wave group velocity:

$$C_g = C_p / 2 [1 + [(4\pi h/L) / \sinh(4\pi h/L)]] \quad (\text{A.2})$$

and C_p is the wave phase speed:

$$C_p = L / T \quad (A.3)$$

where L is the wavelength:

$$L = (gT^2/2\pi) \tanh(2\pi h/L) \quad (A.4)$$

Snell's law describes the bending of the wave crest due to the change in phase speed with water depth:

$$C_p / \sin(\alpha) = \text{constant} \quad (A.5)$$

where α is the acute angle subtended by a line normal to the wave crest (i.e the wave ray or orthogonal) and the tangent to the local depth contour. The change in wave direction between depths h_1 and h_2 is thus given by:

$$\sin(\alpha_2) = [C_{p(2)} / C_{p(1)}] \sin(\alpha_1) \quad (A.6)$$

The increase (at a convergence of wave rays) or decrease (divergence of wave rays) in wave height due to refraction is given by:

$$K_r = H_2/H_1 = [\cos(\alpha_1) / \cos(\alpha_2)]^{0.5} \quad (A.7)$$

where K_r is the refraction coefficient.

Evaluation of the dissipation of wave energy by bottom friction requires the use of empirical friction factors that have been the subject of extensive study. Assuming a plane bed of constant slope,

then the instantaneous rate of wave energy dissipation per unit area of bed due to friction forces under a pure wave (i.e. with no superimposed current), $E_w(t)$, is:

$$E_w(t) = \tau_w(t) U_w(t) \quad (\text{A.8})$$

(Jonsson, 1966) where $\tau_w(t)$ is the instantaneous wave-induced bed shear stress and $U_w(t)$ is the instantaneous near-bed wave-orbital velocity. The time-averaged, over a wave period, wave energy dissipation per unit area of bed, \bar{E}_w , is:

$$\bar{E}_w = 1/T \int_0^T \tau_w(t) U_w(t) dt \quad (\text{A.9})$$

(Kajiura, 1964). The average wave energy dissipation per unit area of bed is integrated over the horizontal wave path and the resultant change in wave height is computed from the decrease in wave energy flux. The change in wave height due to frictional dissipation of a wave propagating from depth h_1 to h_2 , which is a horizontal distance of Δx , is given by:

$$K_f = H_2/H_1 = [(P_1 - \int_{h_1}^{h_2} \bar{E}_w \Delta x) / P_1]^{0.5} \quad (\text{A.10})$$

where K_f is the frictional dissipation coefficient, applicable to the segment bounded by depths h_1 and h_2 , and P is the wave energy flux, defined as:

$$P = (\rho_f g H^2 / 2) C_g \quad (\text{A.11})$$

For practical prediction purposes, equation A.9 needs to be evaluated.

Let:

$$\tau_{w,m} = 1/2 \rho_f f_w U_{w,m}^2 \quad (\text{A.12})$$

after Jonsson (1966) where f_w is the wave friction factor (which should not be confused with the skin-friction wave friction factor, f'_w , in equation 2.9). Using the linear-theory expressions for $U_{w,m}$ (equation 2.10) and $U_w(t)$ (equation 2.12), then $\tau_w(t)$, following equation 2.11, is given by:

$$\tau_w(t) = \tau_{w,m} |\cos(\omega t + \sigma)| \cos(\omega t + \sigma) \quad (\text{A.13})$$

where σ is the phase lag between peak stress and near-bed wave-orbital velocity. Substituting equations 2.12 and A.13 into equation A.9 and integrating gives the result:

$$\bar{E}_w = -2/3\pi \rho_f f_e U_{w,m}^3 \quad (\text{A.14})$$

(Jonsson, 1966) where f_e is the wave dissipation factor:

$$f_e = f_w \cos(\sigma) \quad (\text{A.15})$$

(Grant and Madsen, 1982). If bed shear stress and wave-orbital velocity are in phase, f_e is equal to f_w . For laminar boundary-layer flow, $\sigma =$

45° (Dyer, 1986) and hence $f_e = 0.71 f_w$. For rough turbulent boundary-layer flow, which is expected in nature, experimental data indicate that bed shear stress leads wave-orbital velocity as in laminar flow, but by less than 45°, e.g. Horikawa and Watanabe (1968); Jonsson and Carlsen (1976); Lofquist (1980). The fundamental distinction between f_e and f_w should be maintained, but, weighed against certain assumptions used in deriving the expression for wave energy dissipation, f_e and f_w are generally taken to be equal (e.g. Nielsen et al., 1982). These assumptions include: the initial formulation of the rate of wave energy dissipation (equation A.8) which Jonsson (1966) points out is only a "good guess"; the expression for $\tau_w(t)$ (equation A.13) which, as shown by Lofquist (1980), is probably an unrealistic simplification; the implicit assumption of a constant wave friction factor over the wave cycle; and the first-order expression for $U_w(t)$ (equation 2.12).

The wave friction factor in equations A.15 and A.12 is fundamentally different from f_w' in equation 2.9 since f_w reflects both the skin friction and form drag experienced by the wave, both of which contribute to wave energy dissipation.

The fixed-bed (flat and rippled) roughness models (equations 2.43 and 2.44 respectively) do not always account for the observed roughness of a loose-sand bed under waves (Nielsen et al., 1982; Grant and Madsen, 1982). Grant and Madsen (1982) hypothesized that the inadequacy of fixed-bed roughness models is evidence of "a larger dissipation in the flow than that due to form drag" (p. 475) and that sediment in motion near the bed is the source of the extra dissipation. Grant and Madsen (1982) proposed a model relating the "roughness due to the near-bed

entrained sediment," k_M , (or simply "movable bed roughness") to the skin friction in excess of critical:

$$k_M = 504 (\sqrt{\psi_w^*} - 0.7/\psi_{cr})^2 D \quad (\text{A.16})$$

which is applicable to quartz sand ($\rho_s = 2.65 \text{ g/cm}^3$).

A pure wave thus dissipates energy at a rate proportional to the sum of the skin friction, form drag and drag due to near-bed entrained sediment. The wave friction factor, f_w , is thus a function of the relative roughness, k/A , where k , the total boundary roughness, is the sum of the three sources:

$$k = k_G + k_R + k_M \quad (\text{A.17})$$

Christofferson and Jonsson (1985) demonstrated that gravity-wave dissipation by bed friction in a combined wave and current flow is increased by the nonlinear coupling between the wave and current. The time-averaged (over a wave period) wave energy dissipation rate per unit area of bed by bed friction in a combined wave and current flow, \bar{E}_{wc} , is given by:

$$\bar{E}_{wc} = 1/T \int_0^T \tau_{w,wc}(t) U_w(t) dt \quad (\text{A.18})$$

(Christofferson and Jonsson, 1985). Given:

$$\tau_{w,wc}(t) = 1/2 \rho_f f_{w,wc} U_{w,m}^2 |\cos(\omega t + \sigma)| \cos(\omega t + \sigma) \quad (\text{A.19})$$

and substituting equations A.19 and 2.12 into A.18 and performing the integration gives:

$$\hat{E}_{wc} = -2/3\pi \rho_f f_{e,wc} U_{w,m}^3 \quad (\text{A.20})$$

where $f_{e,wc}$ is the combined-flow wave-energy dissipation factor:

$$f_{e,wc} = f_{w,wc} \cos(\sigma) \quad (\text{A.21})$$

The ratio of wave energy dissipation in a pure wave to wave energy dissipation in the same wave but with a superimposed steady current is therefore given by the ratio $f_w/f_{w,wc}$, where $f_{w,wc}$ is a function of the relative roughness, k/λ , with k defined as the sum of the three individual roughness sources (equation A.17).

The model parameters, which must be specified, include the bathymetric profile and the mean-current velocity field. The initial conditions include the deepwater (i.e. at the seaward base of the profile) wave height, period and angle of incidence. The model equations are best solved, for reasons to be discussed, by stepping across the profile in small segments. The wave height transformation in each segment is solved for as follows.

The change in wave height due to shoaling and refraction between depths h_1 and h_2 is given by equations A.1 and A.7 respectively. An iterative solution for the decrease in wave height due to frictional dissipation is required however, since the rate of wave energy dissipation depends on the wave height, which depends itself on the rate of wave energy dissipation.

To obtain an initial estimate of \bar{E}_{wc} , $U_{w,m}$ is first calculated at the arithmetic mean depth of the segment (i.e. $[h_1+h_2]/2$) using equation 2.10 and assuming the wave height at this point is simply the mean of the initial and transformed (by shoaling and refraction) wave heights. The time-averaged wave energy dissipation rate is calculated from equation A.20 where $f_{e,wc}$ is given by equation A.21 and $f_{w,wc}$ by:

$$f_{w,wc} = \tau_{w,wc} / 1/2 \rho_f U_{w,m}^2 \quad (A.22)$$

$\tau_{w,wc}$ is found by solving the wave-current boundary-layer equations (Chapter 2) with the boundary roughness as defined by A.17. K_f is found from equation A.10 with \bar{E}_{wc} substituted for \bar{E}_w ; note that the length of the wave path (Δx) will not correspond to the segment length if the wave enters the segment at an oblique angle. The new estimate of H_2 is then given by:

$$H_2 = H_1 K_B K_r K_f \quad (A.23)$$

A new value of $U_{w,m}$ at the arithmetic mean depth of the segment is then calculated by assuming the wave height at that point is simply the mean of H_1 and the new H_2 . The whole process is repeated until successive estimates of $f_{e,wc}$ (or H_2) converge.

A set of simultaneous observations of wave height and period at an offshore and an inshore location on the Duck shoreface was used to verify and calibrate the wave-transformation model. The calibration consisted of adjusting certain model parameters until the best agreement between predicted inshore wave heights (using the observed offshore wave

height and period as the initial model conditions) and observed inshore wave heights was obtained. The objective was to maximize the "forecasting efficiency", defined as:

$$1/n \sum_{i=1}^n [(H_{i,\text{predicted}} / H_{i,\text{observed}}) * 100]$$

where n is the number of observations and $H_{i,\text{predicted}}$ and $H_{i,\text{observed}}$ are the ith predicted and observed inshore wave heights respectively.

The observations of wave height and period were made by the personnel at the Field Research Facility and reported in monthly data summaries (CERC, 1980 to present). Waves were measured simultaneously by two Datawell waverider buoys located in water depths of 18 m and 8.5 m approximately 2 km apart on a line extending seawards from the FRF. The reported wave height was the significant wave height (4 times the standard deviation of the sea surface elevation) and the reported wave period was the peak spectral period. The data set used in the verification consists of all the waverider observations made at 1300 hours (chosen arbitrarily) during May, 1984 (27 observations) plus measurements of mean-current speed and direction 100 cm above the bed in 6.5-m water depth 500 m to the south of the inner waverider. The mean offshore wave height for the data set was 0.66 m, ranging from 0.31 m to 1.45 m. The wave periods ranged from 3.95 s to 12.34 s. The weakest reported current was 5 cm/s and the strongest 38 cm/s.

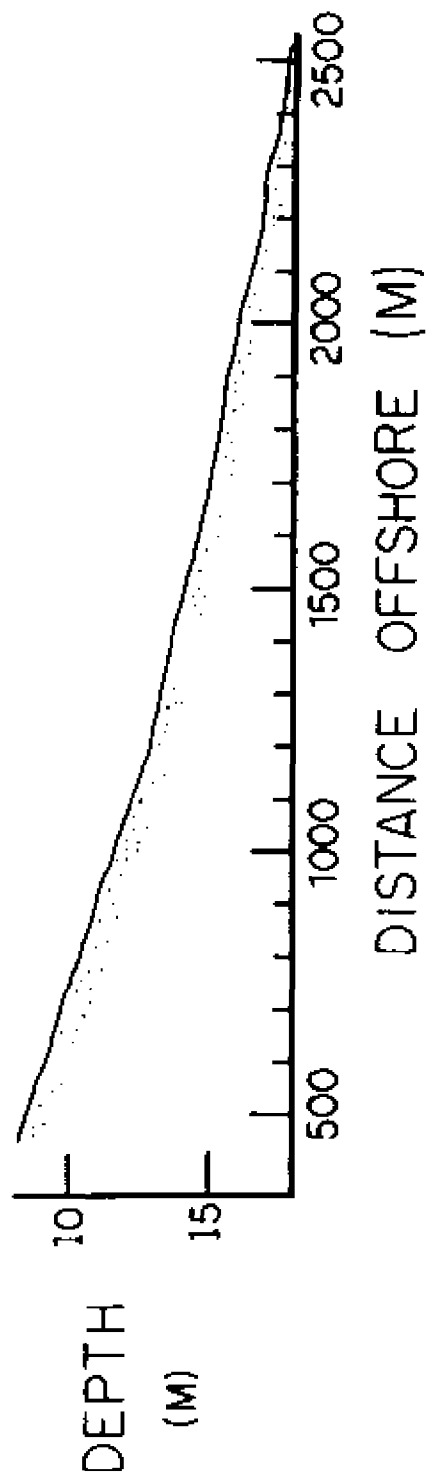
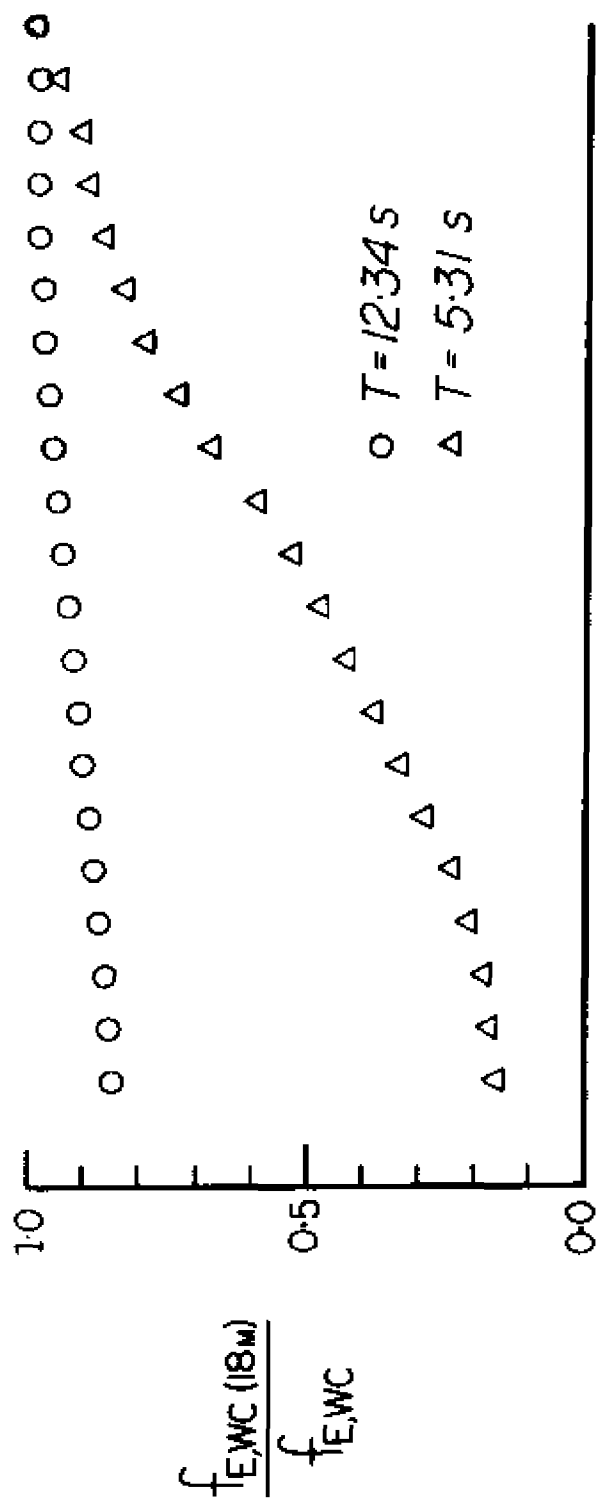
To expedite the computations, it is convenient to represent the two-dimensional bathymetric profile by a continuous analytical expression of the form:

$$h = m x^p \quad (\text{A.24})$$

after Dean (1977), where x is the distance offshore, and the coefficients m and p were found by a least squares fit of A.24 to observed depth data over the domain $200 \text{ m} < x < 5000 \text{ m}$, which corresponds to $3.64 \text{ m} < h < 23.09 \text{ m}$ (i.e. from near the outer bar of the surfzone to the base of the shoreface). The (average) shoreline is located at $(x,h) = (0,0)$. A single value (0.13 mm) was chosen to represent the mean grain-size of the shoreface sediments over the range $3.64 \text{ m} < h < 23.09 \text{ m}$.

Since \bar{E}_{wc} is proportional to $U_{w,m}^3$, the calculated rate of wave energy dissipation at the mean depth of the segment bounded by h_1 and h_2 will be a poor estimate of dissipation across the entire segment if $U_{w,m}$ varies greatly between h_1 and h_2 . \bar{E}_{wc} could be estimated at the geometric mean depth (i.e. $\sqrt{h_1 h_2}$) of the segment, which favors the shallower depth, although a better solution is to shorten the segment length. This solution addresses another potential difficulty: the co-variation of $f_{e,wc}$ and relative roughness (k/A) with depth. The cross-shore variation in $f_{e,wc}$ is potentially complex and is illustrated using two cases drawn from the set of wave observations: a short-period wave ($T = 5.31 \text{ s}$, offshore wave height = 1.26 m); and a long-period wave ($T = 12.34 \text{ s}$, offshore wave height = 1.31 m). For both cases, the model bathymetric profile between 18-m and 8.5-m depth was divided into 100-m segments and the change in $f_{e,wc}$ was computed from segment to segment (Figure A.1). For the purposes of this analysis, the wave-ripple dimensions were $n = 0.03 \text{ m}$ and $\lambda = 0.15 \text{ m}$, and the ripple roughness was given by equation 2.44 with $C_3 = 27.7$.

Figure A.1 The calculated cross-shore variation $f_{e,wc}$ (expressed as the ratio of $f_{e,wc}$ at 18-m depth to local $f_{e,wc}$) and $U_{w,m}/U_c$ for the short-period (5.31 s) and long-period (12.34 s) waves.



The cross-shore variation in $f_{e,wc}$ was large under the short-period wave relative to that under the long-period wave, due primarily to a larger variation in the wave-orbital semi-exursion with depth. A significant improvement in the forecasting efficiency was ultimately realized by allowing $f_{e,wc}$ to vary across the model profile.

The mean current, like the wave-generated ripples, bed sediment and near-bed entrained sediment, influences the rate at which the wave energy is dissipated. The relative contribution made by each to the wave energy dissipation is elucidated by introducing a new roughness length, the "roughness due to the wave-current interaction," k_{wc} . The magnitude of k_{wc} is calculated by finding, using the combined-flow boundary-layer theory with the mean current set to zero (which is equivalent to pure-wave theory), the roughness required to obtain $f_{w,wc}$; subtraction from that roughness of k_G , k_R and k_M leaves k_{wc} . The purpose of introducing this new roughness is to provide a convenient means of comparing the forms (sediments, ripples) and processes (near-bed transport, wave-current interaction) that control $f_{w,wc}$. This in turn will guide the emphasis to be placed on the specification of each relevant parameter.

The analysis was performed using two cases. The first case was that of a swift current: $T = 9.75$ s, offshore wave height = 0.79 m, $U_c = 38$ cm/s. The wave was transformed in two ways: firstly by including the superimposed current in the calculations of wave-dissipation rate and secondly by neglecting it. The bathymetric profile was divided into 100-m segments, and wave-ripple dimensions were taken as: $\eta = 0.03$ m and $\lambda = 0.15$ m. For the purposes of this analysis, equation 2.44 was used for the ripple roughness with $C_3 = 27.7$. The

mean-current speed and direction at every point on the model profile was set equal to the observed mean-current speed and direction at 6.5-m depth. Figure A.2 shows the calculated segment-by-segment variation in $U_{w,m}/U_c$ and \bar{E}_{wc}/\bar{E}_w where \bar{E}_w is the wave energy dissipation rate assuming zero current (equation A.14). As $U_{w,m}/U_c$ increased, \bar{E}_{wc}/\bar{E}_w decreased, primarily because the current became relatively less energetic. The extra wave energy dissipated by the current ranged from nearly 15% at 18-m depth to -5% at 8.5-m depth.

The second case was that of a weak superimposed current: $T = 8.06$ s, offshore wave height = 0.40 m, $U_c = 5$ cm/s. The extra wave energy dissipated by the current in this case was only -1% across the entire profile (Figure A.2).

The segment-by-segment variation in the four roughness types was calculated for the cases of strong and weak superimposed mean current, and these results are plotted in Figure A.3. Ripple roughness was the dominant source of roughness for the case of weak superimposed mean current. k_{wc} varied from -0.4 cm offshore to -0.2 cm inshore, which was only -2% of the magnitude of k_R . k_M varied in the opposite sense: from -0.1 cm at 13-m depth where threshold was initially exceeded, to -0.5 cm at 8.5-m depth. At its maximum, k_M was no more than 3% of the magnitude of k_R . Grain roughness was negligible.

For the case of strong superimposed mean current, in which the current added on the order of 10% to the wave energy dissipation rate across the profile, wave ripples were again the dominant source of roughness. k_{wc} varied from -4.4 cm in 18-m water depth to -1.7 cm in 8.5-m depth, which represented 27%, at 18-m depth, and 10%, at 8.5-m

Figure A.2 The calculated cross-shore variation in wave energy dissipation with the current added (\bar{E}_{wc}), and wave energy dissipation neglecting the current (\bar{E}_w) for the cases of strong and weak superimposed mean current.

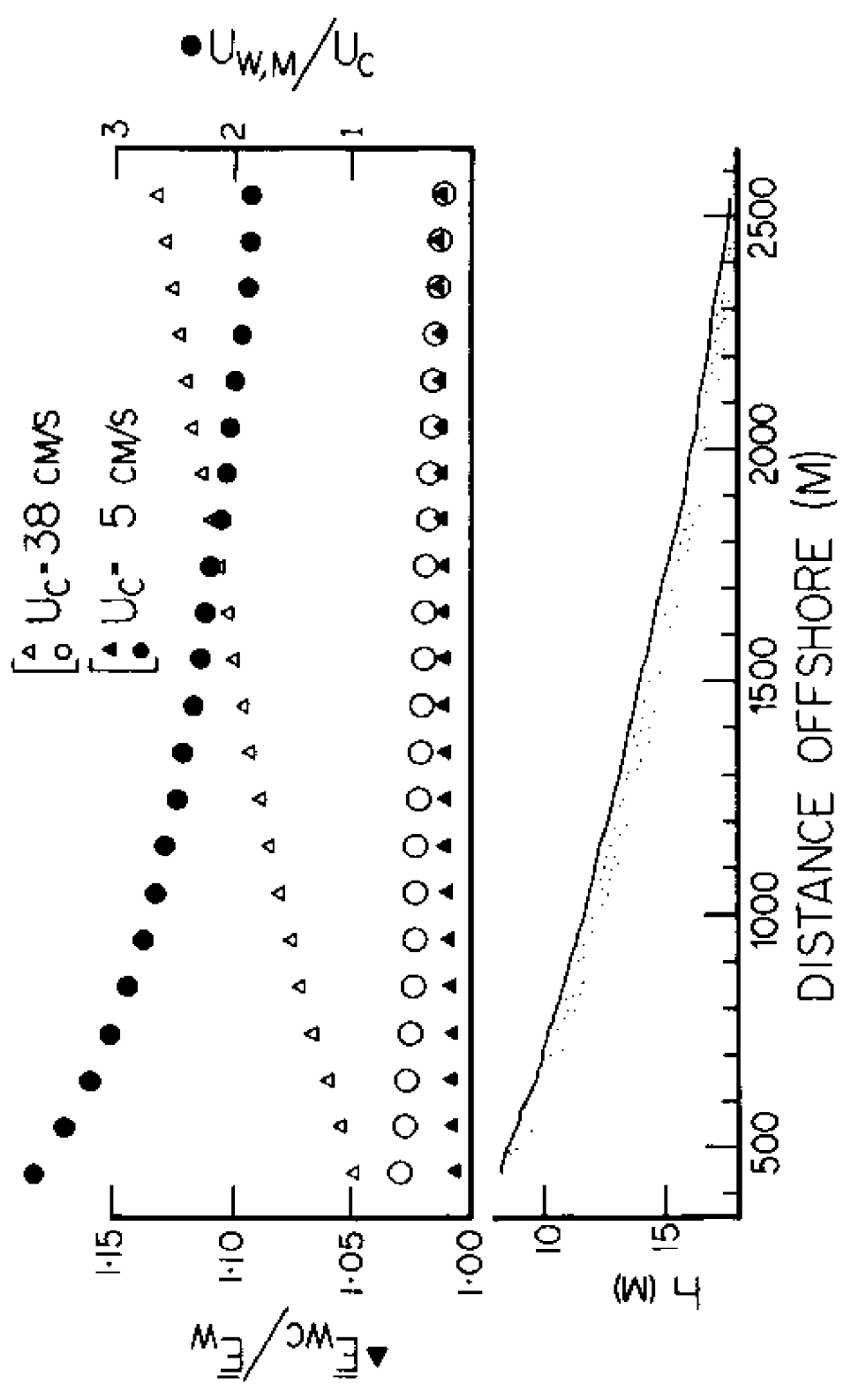
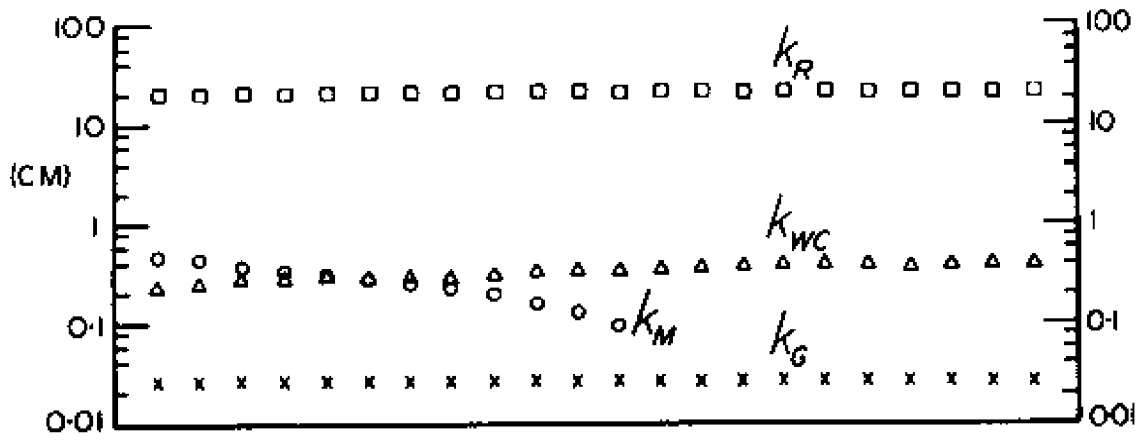


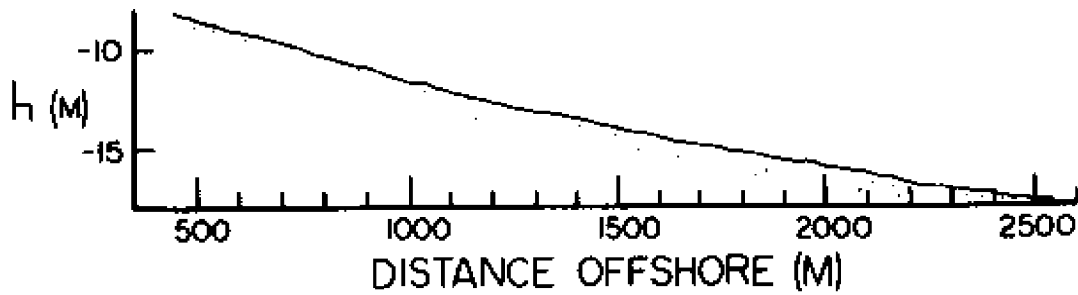
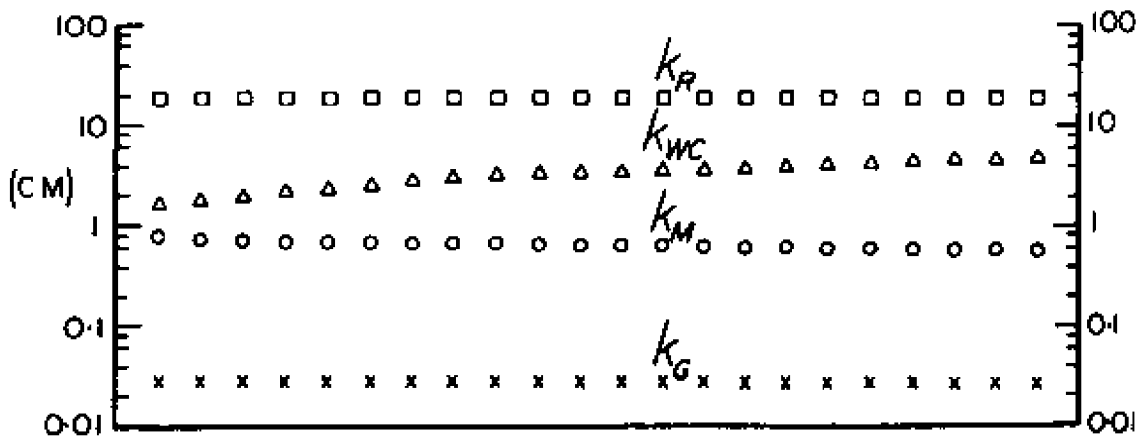
Figure A.3 Calculated variation across the model profile in k_G , k_R , k_M and k_{wc} .

- A. Weak superimposed mean current (5 cm/s).
- B. Strong superimposed mean current (38 cm/s).

A WEAK CURRENT



B STRONG CURRENT

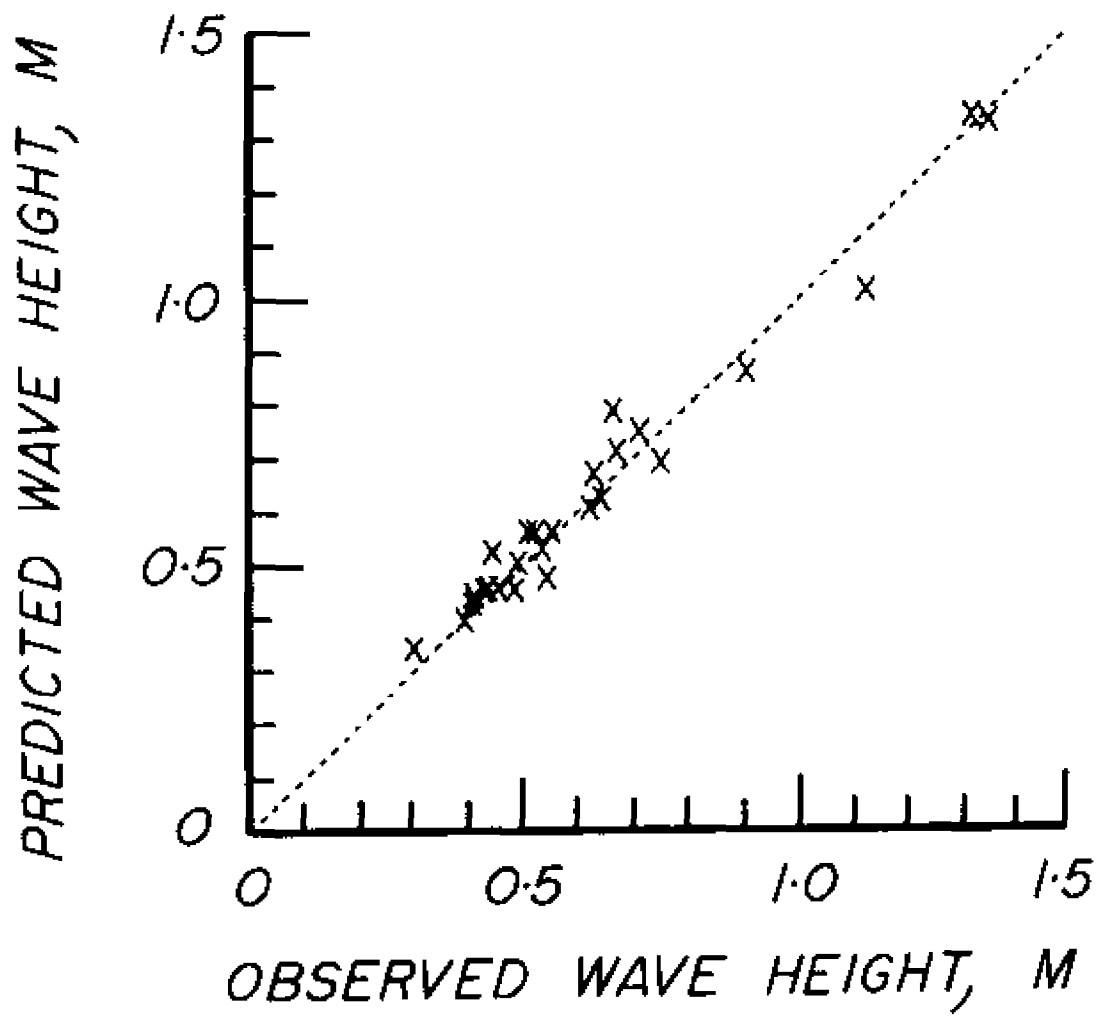


depth, of the magnitude of k_R . k_M increased from -0.6 to -0.8 cm, which was only -4% of the magnitude of k_R .

Thus, even when a strong mean current is superimposed, wave ripples are the dominant source of roughness; k_{wc} , at its maximum, was only 27% of the magnitude of k_R , which is considerably less than the uncertainty associated with the estimate of k_R (compare Grant and Madsen's (1982) value of C_3 in equation 2.44 with Nielsen's (1983) value).

The forecasting efficiency index was calculated using various combinations of observed ripple dimensions (including using an empirical predictive model to predict the change in ripple dimensions across the profile as a function of the changing depth and wave conditions), roughness models and mean-current distributions. The best results were obtained by allowing for the current-enhancement of the wave dissipation; by using the Grant and Madsen (1982) combined roughness model (i.e. $C_3 = 27.7$ in equation 2.44 together with equation A.16 for the movable-bed roughness); and by assuming fixed wave-ripple dimensions across the profile ($\eta = 0.03$ m, $\lambda = 0.15$ m). The best forecasting efficiency finally obtained was 101.65% (Figure A.4), which was associated with the lowest mean absolute deviation of predicted from observed wave heights.

Figure A.4 Predicted versus observed inshore (8.5-m depth) wave heights. Forecasting efficiency was 101.65%, and mean absolute deviation of predicted from observed wave heights was 0.038 m.



LITERATURE CITED

- Abou-Seida, M.M., 1965. Bed load function due to wave action. Rept. HEL-2-11, Hydraulic Eng. Lab., Univ. of California, Berkeley, 78 pp.
- Abramowitz, M. and Stegun, I.A., 1964. Handbook of Mathematical Functions with Formulas, Graphs and Mathematical Tables. Dover, New York, 1046 pp.
- Ackers, P. and White, W.R., 1973. Sediment transport: new approach and analysis. Proc. A.S.C.E., J. Hydr. Div., 99: 2041-2060.
- Aubrey, D.G. and Trowbridge, J.H., 1985. Kinematic and dynamic estimates from electromagnetic current meter data. J. Geophys. Res., 90: 9137-9146.
- Bagnold, R.A., 1963. Mechanics of marine sedimentation. In: M.N. Hill (Editor), The Sea, Vol. 3. Wiley-Interscience, New York, pp. 507-528.
- Bailard, J.A., 1981. An energetics total load sediment transport model for a plane sloping beach. J. Geophys. Res., 86: 10,938-10,954.
- Bailard, J.A. and Inman, D.L., 1981. An energetics bedload transport model for a plane, sloping beach: local transport. J. Geophys. Res., 86: 2035-2043.
- Bakker, W.T. and van Dorn, T., 1978. Near-bottom velocities in waves with a current. Proc. 16th Int. Coastal Eng. Conf., Hamburg, A.S.C.E., pp. 1394-1413.
- Battisti, D.S. and Clarke, A.J., 1982. A simple method for estimating barotropic tidal currents on continental margins with specific application to the M_2 tide off the Atlantic and Pacific coasts of the United States. J. Phys. Oceanogr., 12: 8-16.
- Beardsley, R.C. and Boicourt, W.C., 1981. On estuarine and continental circulation in the Middle-Atlantic Bight. In: B.A. Warren and C. Wunsch (Editors), Evolution of Physical Oceanography. MIT Press, Cambridge, Massachusetts, pp. 198-233.
- Beardsley, R.C., Boicourt, W.C. and Hansen, D.V., 1976. Physical oceanography of the Middle Atlantic Bight. In: M.G. Gross (Editor), Middle Atlantic Continental Shelf and the New York Bight. Special Symposium 2, American Soc. Limnol. Oceanogr., pp. 20-34.

- Beardsley, R.C. and Butman, B., 1974. Circulation on the New England continental shelf: response to strong winter storms. *Geophys. Res. Lett.*, 1: 181-184.
- Bijker, E.W., 1966. The increase of bed shear in a current due to wave motion. Proc. 10th Int. Coastal Eng. Conf., Tokyo, A.S.C.E., pp. 746-765.
- Bijker, E.W., 1967. Some considerations about scales for coastal models with movable beds. Rept. No. 50, Delft Hydr. Lab., Netherlands, 142 pp.
- Bijker, E.W., 1971. Longshore transport computations. Proc. A.S.C.E., J. Waterways, Harbors and Coastal Eng. Div., 97: 687-701.
- Birkemeler, W.A., Miller, H.C., Wilhelm, S.D., DeWall, A.E. and Gorbics, C.S., 1985. A user's guide to the Coastal Engineering Research Center's (CERC's) Field Research Facility. Instruction Rept. CERC-85-1, U.S. Army Corps of Engineers, Waterways Expt. Station, Vicksburg, Miss., 121 pp.
- Boicourt, W.C. and Hacker, P.W., 1976. Circulation on the Atlantic continental shelf of the United States, Cape May to Cape Hatteras. Mem. Soc. Royale des Sciences de Liege, 6th Series, 10: 187-200.
- Bowen, A.J., 1980. Simple models of nearshore sedimentation; beach profiles and longshore bars. In: S.B. McCann (Editor), *The Coastline of Canada*. Paper 80-10, Geol. Surv. of Canada, p. 1-11.
- Bowen, A.J. and Doering, J.C., 1984. Nearshore sediment transport: estimates from detailed measurements of the nearshore velocity field. Proc. 19th Int. Coastal Eng. Conf., Houston, A.S.C.E., pp. 1703-1714.
- Brown, C.B., 1950. Sediment transportation. In: H. Rouse (Editor), *Engineering Hydraulics*. Wiley, New York, p. 797.
- Bruun, P., 1962. Sea-level rise as a cause of shore erosion. Proc. A.S.C.E., J. Waterways and Harbors Div., 88: 117-130.
- Bumpus, D.F., 1965. Residual drift along the bottom on the continental shelf in the Middle Atlantic Bight area. *Limnology and Oceanography*, Suppl. 10: R50-R53.
- Cacchione, D.A. and Drake, D.E., 1982. Measurements of storm-generated bottom stresses on the continental shelf. *J. Geophys. Res.*, 87: 1952-1960.
- Chriss, T.M. and Caldwell, D.R., 1982. Evidence for the influence of form drag on bottom boundary layer flow. *J. Geophys. Res.*, 87: 4148-4154.

- Christofferson, J.B. and Jonsson, I.G., 1985. Bed friction and dissipation in a combined current and wave motion. *Ocean Engineering*, 12: 387-423.
- Coastal Engineering Research Center, 1980 to present. Preliminary data summary. Field Research Facility, U.S. Army Corps of Engineers, Waterways Expt. Station, Kitty Hawk, North Carolina.
- Cowell, P.J., 1986. Australian "mega rip" study. *Trans. Am. Geophys. Union*, 67: 449.
- Csanady, G.T., 1982. *Circulation in the Coastal Ocean*. Reidel, Dordrecht, Holland, 279 pp.
- Curray, J.R., 1969. Shore zone sand bodies: barriers, cheniers and beach ridges. In: D.J. Stanley (Editor), *The New Concepts of Continental Margin Sedimentation*. American Geological Institute, Washington, D.C., pp. JC-2-1 - JC-2-19.
- Davies, A.G., 1980. Field observations of the threshold of sand motion in a transitional wave boundary layer. *Coastal Eng.*, 4: 23-46.
- Davies, A.G., 1984. Field observations of wave-induced motion above the seabed and of the resulting sediment movement. I.O.S. Rept. No. 179, Inst. Oceanogr. Sciences, Taunton, U.K., 171 pp.
- Davies, A.G., 1985. Field observations of the threshold of sediment motion by wave action. *Sedimentology*, 32: 685-704.
- Dean, R.G., 1977. Equilibrium beach profiles: U.S. Atlantic and Gulf Coasts. *Ocean Eng. Tech. Rept. 12*, Dept. Civil Eng., Univ. of Delaware, Newark, Delaware, 46 pp.
- Doering, J.C. and Bowen, A.J., 1987. Skewness in the nearshore zone: a comparison of estimates from Marsh-McBirney current meters and colocated pressure sensors. *J. Geophys. Res.*, 92: 13,173-13,183.
- Dyer, K.R., 1980. Velocity profiles over a rippled bed and the threshold of movement of sand. *Estuarine and Coastal Mar. Sci.*, 10: 181-199.
- Dyer, K.R., 1986. *Coastal and Estuarine Sediment Dynamics*. Wiley-Interscience, Chichester, Great Britain, 342 pp.
- Einstein, H.A., 1950. Bed-load function for sediment transportation in open channel flows. *Tech. Bull. No. 1026*, U.S. Dept. Agriculture, Soil Cons. Serv., 71 pp.
- Engelund, F. and Hansen, E., 1967. A monograph on sediment transport in alluvial streams. *Teknisk Forlag, Copenhagen*, 62 pp.
- Engelund, F. and Hansen, E., 1972. A monograph on sediment transport. *Teknisk Forlag, Copenhagen*.

- Everts, C.H., 1978. Geometry of profiles across inner continental shelves of the Atlantic and Gulf coasts of the United States. Tech. Paper 78-4, U.S. Army Corps of Engineers, Coastal Engineering Research Center, Fort Belvoir, Virginia, 29 pp.
- Field, M.E., Meisburger, E.P., Stanley, E.A. and Williams, S.J., 1979. Upper Quaternary peat deposits on the Atlantic inner shelf of the United States. Geol. Soc. Am. Bull., 90: 618-628.
- Fischer, A.G., 1961. Stratigraphic record of transgressing seas in light of sedimentation on Atlantic coast of New Jersey. Bull. Amer. Assoc. Pet. Geol., 45: 1656-1666.
- Folk, R.L., 1980. Petrology of Sedimentary Rocks. Hemphill, Austin, Texas, 182 pp.
- Frijlink, H.C., 1952. Discussion des formules de debit solide de Kalinske, Einstein et Meyer-Peter et Muller compte tenue des mesures recentes de transport dans les rivieres Neerlandaises. Soc. Hydrol. Fr., Grenoble, J. Hydraulique, 2: 98-103.
- Gadd, P.E., Lavelle, J.W. and Swift, D.J.P., 1978. Estimates of sand transport on the New York shelf using near-bottom current meter observations. J. Sed. Petrol., 48: 239-252.
- Grant, W.D. and Madsen, O.S., 1979. Combined wave and current interaction with a rough bottom. J. Geophys. Res., 84: 1779-1808
- Grant, W.D. and Madsen, O.S., 1982. Movable bed roughness in unsteady oscillatory flow. J. Geophys. Res., 87: 469-481.
- Grant, W.D., Williams, A.J. and Glenn, S.M., 1984. Bottom stress estimates and their prediction on the northern California continental shelf during CODE-1: the importance of wave-current interaction. J. Phys. Oceanogr., 14: 506-527.
- Grant, W.D., Williams, A.J., Glenn, S.M., Cacchione, D.A. and Drake, D.E., 1983. High frequency bottom stress variability and its prediction in the CODE region. W.H.O.I. Tech Rept. 83-19, Woods Hole Oceanogr. Inst., Woods Hole, Massachusetts, 72 pp.
- Green, M.O., 1986. Side-scan sonar mosaic of a sand ridge field: southern mid-Atlantic Bight. Geo-Marine Letters, 6: 35-40.
- Green, M.O. and Boon, J.D., 1987. Response characteristics of a short-range, high-resolution, digital sonar altimeter. Mar. Geol., in press.
- Guza, R.T. and Thornton, E.B., 1985. Velocity moments in nearshore. Proc. A.S.C.E., J. Waterway, Port, Coastal and Ocean Eng., 111: 235-256.
- Hallermeier, R.J., 1982. Oscillatory bedload transport: data review and simple formulation. Cont. Shelf Res., 1: 159-190.

- Hamblin, P.F., Marmoush, Y.M.R. and Boyce, F.M., 1987. Field evaluation of an electromagnetic current meter based vertical profiler. *J. Geophys. Res.*, 92: 11,867-11,872.
- Hardisty, J., 1983. An assessment and calibration of formulations for Bagnold's bedload equation. *J. Sed. Petrol.*, 53: 1007-1010.
- Heathershaw, A.D., 1981. Comparisons of measured and predicted sediment transport rates in tidal currents. *Mar. Geol.*, 42: 75-104.
- Heathershaw, A.D. and Carr, A.P., 1977. Measurements of sediment transport rates using radioactive tracers. *A.S.C.E., Proc. Coastal Sediments '77*, Charleston, South Carolina, pp. 399-416.
- Heathershaw, A.D., Carr, A.P. and Blackley, M.W.L., 1981. Final report: Coastal erosion and nearshore sedimentation processes. Topic Rept. B, Swansea Bay Project, Ser. Rept. No. 118, Inst. Oceanogr. Sciences, Taunton, U.K., 67 pp.
- Horikawa, K. and Watanabe, A., 1968. Laboratory study on oscillatory boundary layer flow. *Coastal Eng. Japan*, 11: 13-28.
- Horikawa, K., Watanabe, A. and Katori, S., 1982. Sediment transport under sheet flow conditions. *Proc. 18th Int. Coastal Eng. Conf.*, Capetown, A.S.C.E., pp. 1335-1352.
- Hsiao, S.V. and Shemdin, O.H., 1979. Bottom dissipation in finite-depth water waves. *Proc. 16th Int. Coastal Eng. Conf.*, Hamburg, A.S.C.E., pp. 434-448.
- Huntley, D.A. and Bowen, A.J., 1975. Comparison of the hydrodynamics of steep and shallow beaches. In: J. Hails and A. Carr (Editors), *Nearshore Sediment Dynamics and Sedimentation*. Wiley-Interscience, London, pp. 69-110.
- Huyer, A.B.M., Hickey, J.D., Smith, R.L. and Pillsbury, R.D., 1975. Alongshore coherence at low frequencies in currents observed over the continental shelf off Oregon and Washington. *J. Geophys. Res.*, 80: 3495-3505.
- Inman, D.L., and Bagnold, R.A., 1963. Littoral processes. In: M.N. Hill (Editor), *The Sea*, Vol. 3. Wiley-Interscience, New York, pp. 529-533.
- Ippen, A.T., 1966. *Estuary and Coastline Hydrodynamics*. McGraw-Hill, New York, 744 pp.
- Jonsson, I.G., 1966. Wave boundary layers and friction factors. *Proc. 10th Int. Coastal Eng. Conf.*, Tokyo, A.S.C.E., pp. 127-148.
- Jonsson, I.G. and Carlsen, N.A., 1976. Experimental and theoretical investigations in an oscillatory (rough) turbulent boundary layer. *J. Hydraulic Res.*, 14: 45-60.

- Kachel, N.B. and Sternberg, R.W., 1971. Transport of bedload as ripples during an ebb current. *Mar. Geol.*, 10: 229-244.
- Kajiura, K., 1964. On the bottom friction in an oscillatory current. *Bull. Earthquake Res. Inst. Tokyo Univ.*, 42: 147-174.
- Kalkanis, G., 1964. Transportation of bed material due to wave action. *Tech. Memo. No. 2, U.S. Army Corps of Engineers, Coastal Eng. Res. Center*, 38 pp.
- Kamphuis, J.W., 1975. Friction factor under oscillatory waves. *Proc. A.S.C.E., J. Waterways, Harbors and Coastal Eng. Div.*, 101: 135-144.
- Karl, H.A., Drake, D.E. and Cacchione, D.A., 1981. Response of the suspended sediment transport system to continental shelf dynamics. *Geo-Marine Letters*, 1: 243-248.
- Kemp, P.H. and Simons, R.R., 1983. The interaction of waves and a turbulent current: waves propagating against the current. *J. Fluid Mechanics*, 130: 73-90.
- Kim, C.S. and Wright, L.D., 1987. Longshore bars and mass transport induced by long waves. *Proc. A.S.C.E., Conference on Coastal Hydrodynamics, Univ. of Delaware, Newark*, pp. 564-578.
- Kobayashi, N., 1982. Sediment transport on a gentle slope due to waves. *Proc. A.S.C.E., J. Waterway, Port, Coastal and Ocean Div.*, 108: 254-271.
- Komar, P.D., 1971. The mechanics of sand transport on beaches. *J. Geophys. Res.*, 76: 713-721.
- Komar, P.D., 1976. Boundary layer flow under steady unidirectional currents. In: D.J. Stanley and D.J.P. Swift (Editors), *Marine Sediment Transport and Environment Management*. Wiley-Interscience, New York, pp. 91-106.
- Komar, P.D., 1977. Beach sand transport: distribution and total drift. *Proc. A.S.C.E., J. Waterway, Port, Coastal and Ocean Div.*, 103: 225-239.
- Langhorne, D.N., 1982. A study of the dynamics of a marine sandwave. *Sedimentology*, 29: 571-594.
- Larsen, L.H., Sternberg, R.W., Shi, N.C., Marsden, M.A.H. and Thomas, L., 1981. Field investigations of the threshold of grain motion by ocean waves and currents. *Mar. Geol.*, 42: 105-132.
- Lavelle, J.W., Swift, D.J.P., Gadd, P.E., Stubblefield, W.L., Case, F.N., Brashear, H.R. and Haff, K.W., 1978. Fair weather and storm sand transport on the Long Island, New York, inner shelf. *Sedimentology*, 25: 823-842.

- Leatherman, S.P., 1979. Migration of Assateague Island, Maryland, by inlet and overwash processes. *Geology*, 7: 104-107.
- Lees, B.J., 1979. A new technique for injecting fluorescent sand tracer in sediment transport experiments in a shallow wave environment. *Mar. Geol.*, 33: M95-M98.
- Lees, B.J., 1981. Sediment transport measurements in the Sizewell-Dunwich Banks area, East Anglia, U.K. In: S.-D. Nio, R.T.E. Shuttenehm and T.J.C.E. van Weering (Editors), *Holocene Marine Sedimentation in the North Sea Basin*, Special Publication 5, Int. Assoc. Sedimentologists, Blackwell Scientific, Oxford, pp. 269-281.
- Lees, B.J., 1983. The relationship of sediment transport rates and paths to sandbanks in a tidally dominated area off the coast of East Anglia, U.K. *Sedimentology*, 30: 461-483.
- LeMehaute, B., 1976. *An Introduction to Hydrodynamics and Water Waves*. Springer-Verlag, New York, 315 pp.
- Lesht, B.M., 1980. Benthic boundary-layer velocity profiles: dependence on averaging period. *J. Phys. Oceanogr.*, 10: 985-991.
- Lesht, B.M., Clarke, T.L., Young, R.A., Swift, D.J.P. and Freeland, G.L., 1980. An empirical relationship between the concentration of resuspended sediment and near bottom wave-orbital velocity. *Geophys. Res. Lett.*, 7: 1049-1052.
- Lofquist, K.E.B., 1980. Measurements of oscillatory drag on sand ripples. *Proc. 17th Int. Coastal Eng. Conf.*, Sydney, A.S.C.E., pp. 3087-3108.
- Ludwick, J.C., 1978. Coastal currents and an associated sand stream off Virginia Beach, Virginia. *J. Geophys. Res.*, 83: 2365-2372.
- Lundgren, H. and Jonsson, I.G., 1961. Bed shear stresses induced by waves and a current. *Basic Research Prog. Rept. 1*, Coastal Eng. Lab., Tech. Univ. Denmark.
- Madson, O.S. and Grant, W.D., 1976. Sediment transport in the coastal environment. *Rept. No. 209*, Ralph M. Parsons Lab., Dept. Civil Eng., Mass. Inst. Technol., Massachusetts, 105 pp.
- Manohar, M., 1955. Mechanics of bottom sediment movement due to wave action. *Tech. Memo. No. 75*, U.S. Army Corps of Engineers, Beach Erosion Board, 121 pp.
- Miller, M.C. and Komar, P.D., 1979. Measurements of sand spreading rates under near-bottom wave orbital motions. *J. Geol.*, 87: 593-608.
- Moody, D.W., 1964. Coastal morphology and processes in relation to the development of submarine sand ridges off Bethany Beach, Delaware. *Thesis*, Johns Hopkins Univ., Baltimore, Maryland, 167 pp.

- Murray, S.P., 1967. Control of grain dispersion by particle size and wave state. *J. Geol.*, 75: 612-634.
- Niedoroda, A.W., 1980. Shoreface surf-zone sediment exchange processes and shoreface dynamics. Tech. Memo. OMPA-1, N.O.A.A., Boulder, Colorado, 89 pp.
- Niedoroda, A.W., Ma, C.M., Mangarella, P.A., Cross, R.H., Huntsman, S.R. and Treadwell, D.D., 1982. Measured and computed coastal ocean bedload transport. Proc. 18th Int. Coastal Eng. Conf., Capetown, A.S.C.E., pp. 1353-1368.
- Niedoroda, A.W. and Swift, D.J.P., 1981. Maintenance of the shoreface by wave orbital currents and mean flow: observations from the Long Island coast. *Geophys. Res. Lett.*, 8: 337-340.
- Niedoroda, A.W., Swift, D.J.P. and Hopkins, T.S., 1985. The shoreface. In: R.A. Davis (Editor), *Coastal Sedimentary Environments*, 2nd Rev. Ed. Springer-Verlag, New York, pp. 533-624.
- Nielsen, P., 1979. Some basic concepts of wave sediment transport. Series Paper 20, Institute of Hydrodynamics and Hydraulic Engineering, Tech. Univ. of Denmark, Lyngby, Denmark, 160 pp.
- Nielsen, P., 1983. Analytical determination of nearshore wave height variation due to refraction, shoaling and friction. *Coastal Eng.*, 7: 233-251.
- Nielsen, P., Green, M.O. and Coffey, F.C., 1982. Suspended sediment under waves. Coastal Studies Unit Tech. Rept. No. 82/6, University of Sydney, Sydney, 157 pp.
- Nowell, A.G.M., 1983. The benthic boundary layer and sediment transport. *Rev. Geophys. Space Phys.*, 21: 1181-1192.
- Pattiaratchi, C.B. and Collins, M.B., 1984. Sediment transport under waves and tidal currents: a case study from the northern Bristol Channel, U.K. *Mar. Geol.*, 56: 27-40.
- Pattiaratchi, C.B. and Collins, M.B., 1985. Sand transport under the combined influence of waves and tidal currents: an assessment of available formulae. *Mar. Geol.*, 67: 83-100.
- Pierce, J.W. and Colquhoun, D.J., 1970. Holocene evolution of a portion of the North Carolina coast. *Geol. Soc. Am. Bull.*, 81: 3697-3714.
- Pond, S.P. and Pickard, G.L., 1978. *Introductory Dynamic Oceanography*. Pergamon Press, New York, 241 pp.
- Redfield, A.C., 1958. The influence of the continental shelf on the tides of the Atlantic coast of the United States. *J. Mar. Research*, 17: 432-448.

- Reimnitz, E., Toimil, L.J., Shepard, F.P. and Gutierrez-Estrada, M., 1976. Possible rip current origin for bottom ripple zones to 30-m depth. *Geology*, 4: 395-400.
- Scott, J.T. and Canady, G.T., 1976. Nearshore currents off Long Island. *J. Geophys. Res.*, B1: 5401-5409.
- Seymour, R.J., 1985. Threshold effects on sediment transport by waves. *Proc. A.S.C.E., J. Waterway, Port, Coastal and Ocean Eng.*, 111: 371-387.
- Seymour, R.J., 1986. Nearshore auto-suspending turbidity currents. *Ocean Engineering*, 13: 435-447.
- Shi, N.C. and Larsen, L.H., 1984. Reverse sediment transport induced by amplitude modulated waves. *Mar Geol.*, 54: 181-200.
- Shi, N.C., Larsen, L.H. and Downing, J.P., 1985. Predicting suspended sediment concentration on continental shelves. *Mar. Geol.*, 62: 255-276.
- Shibayama, T. and Horikawa, K., 1980. Laboratory study on sediment transport mechanics due to wave action. *Proc. Japan Soc. Civil Eng.*, 296: 131-141.
- Sleath, J.F.A., 1978. Measurements of bed load in oscillatory flow. *Proc. A.S.C.E., J. Waterway, Port, Coastal and Ocean Div.*, 104: 291-307.
- Sleath, J.F.A., 1984. *Sea Bed Mechanics*. Wiley-Interscience, New York, 335 pp.
- Smith, J.D., 1977. Modeling of sediment transport on continental shelves. In: E.D. Goldberg, I.N. McCave, J.J. O'Brien and J.H. Steele (Editors), *The Sea*, Vol. 6. Wiley-Interscience, New York, pp. 539-577.
- Sternberg, R.W., 1972. Predicting initial motion and bedload transport of sediment particles in the shallow-marine environment. In: D.J.P. Swift, D.B. Duane and O.H. Pilkey (Editors), *Shelf Sediment Transport: Process and Pattern*. Dowden, Hutchinson and Ross, Stroudsburg, Pennsylvania, pp. 6-82.
- Stubblefield, W.L. and Swift, D.J.P., 1981. Grain-size variation across sand ridges, New Jersey continental shelf. *Geo-Marine Letters*, 1: 45-48.
- Swart, D.H., 1974. Offshore sediment transport and equilibrium beach profiles. Publ. No. 131, Delft Hydr. Lab., Netherlands.
- Swart, D.H., 1976. Coastal sediment transport: computation of longshore transport. Rept. No. R968, Delft Hydr. Lab., Netherlands, 61 pp.

- Swift, D.J.P. and Field, M.E., 1981. Storm-built sand ridges on the Maryland inner shelf: a preliminary report. *Geo-Marine Letters*, 1: 33-37.
- Swift, D.J.P., Niedoroda, A.W., Vincent, C.E. and Hopkins, T.S., 1985. Barrier island evolution, Middle Atlantic Bight, U.S.A., Part 1: Shoreface dynamics. *Mar. Geol.*, 63: 331-361.
- Swift, D.J.P., Parker, G., Lanfredi, N.W., Perillo, G. and Figge, K., 1978. Shoreface-connected sand ridges on American and European shelves: A comparison. *Estuarine and Coastal Mar. Sci.*, 7: 257-273.
- Swift, D.J.P., Sanford, R.B., Dill, C.E. and Avignone, M.F., 1971. Textural differentiation on the shore face during erosional retreat of an unconsolidated coast, Cape Henry to Cape Hatteras, western North Atlantic shelf. *Sedimentology*, 16: 221-250.
- Tanaka, H. and Shuto, N., 1981. Friction coefficient for a wave-current coexisting system. *Coastal Eng. Japan*, 24: 105-128.
- Thorne, P.D., Salkied, A.P. and Marks, A.J., 1983. Application of acoustic techniques in sediment transport research. *Proc. Conf. Acoustics and the Sea Bed*, Inst. of Acoustics, pp. 395-402.
- Thornton, E.B., 1973. Distribution of sediment transport across the surfzone. *Proc. 13th Int. Coastal Eng. Conf.*, Vancouver, A.S.C.E., pp. 1049-1068.
- Van der Graaf, J. and van Overeem, J., 1979. Evaluation of sediment transport formulae in coastal engineering practice. *Coastal Eng.*, 3: 1-32.
- Vincent, C.E., Young, R.A. and Swift, D.J.P., 1981. Bedload transport under waves and currents. *Mar. Geol.*, 39: M71-M80.
- Vincent, C.E., Young, R.A. and Swift, D.J.P., 1982. On the relationship between bedload and suspended sand transport on the inner shelf, Long Island, New York. *J. Geophys. Res.*, 87: 4163-4170.
- Vincent, C.E., Young, R.A. and Swift, D.J.P., 1983. Sediment transport on the Long Island shoreface, North American Atlantic shelf: Role of waves and currents in shoreface maintenance. *Cont. Shelf Res.*, 2: 163-182.
- Wells, D.R., 1967. Beach equilibrium and second-order wave theory. *J. Geophys. Res.*, 72: 497-504.
- Wiberg, P. and Smith, J.D., 1983. A comparison of field data and theoretical models for wave-current interactions at the bed on the continental shelf. *Cont. Shelf Res.*, 2: 147-162.
- Wilkinson, R.H., 1986. Variation of roughness length of a mobile sand bed in a tidal flow. *Geo-Marine Letters*, 5: 231-239.

- Williams, S.J., 1983. Results of a sidescan sonar, seismic reflection and sediment sampling survey off Duck, North Carolina as part of the ARSLOE study. Open-File Report, Coastal Engineering Research Center, Fort Belvoir, VA, 19 pp.
- Winant, C.D., 1979. Coastal current observations. Rev. Geophys. Space Phys., 17: 89-98.
- Wright, L.D., 1981. Nearshore tidal currents and sand transport in a macrotidal environment. Geo-Marine Letters, 1: 173-179.
- Wright, L.D., Boon, J.D., III, Green, M.O. and List, J.H., 1986. Response of the mid shoreface of the southern mid-Atlantic Bight to a "northeaster". Geo-Marine Letters, 6: 153-160.
- Wright, L.D., May, S.K., Short, A.D. and Green, M.O., 1984. Beach and surfzone equilibria and response times. Proc. 19th Int. Coastal Eng. Conf., Houston, A.S.C.E., pp. 2150-2164.
- Wright, L.D., Nielsen, P., Short, A.D., Coffey, F.C. and Green, M.O., 1982. Nearshore and surfzone morphodynamics of a storm wave environment: eastern Bass Strait, Australia. Coastal Studies Unit Tech. Rept. 82/3, University of Sydney, Sydney, 154 pp.
- Yalin, M.S., 1963. An expression for bedload transportation. Proc. A.S.C.E., J. Hyd. Div., 89: 221-250.

VITA

MALCOLM OMAND GREEN

Born in Sydney, Australia on 30 May, 1956. An avid surfer, entered the marine science program at the University of Sydney and graduated in 1979 with a Bachelor of Science with First Class Honours. Was employed for the next three years as a research assistant with the Coastal Studies Unit under L.D. Wright on a project funded by the U.S. Office of Naval Research to investigate beach morphodynamics at various locations around Australia. Decided to see the world, and in August, 1982, began graduate school at the Virginia Institute of Marine Science.